NANOPARTICLE SENSITISATION OF SOLID-STATE NANOCRYSTALLINE SOLAR CELL

THÈSE N^O 3017 (2004)

PRÉSENTÉE À LA FACULTÉ SCIENCES DE BASE

Institut des sciences et ingénierie chimiques

SECTION DE CHIMIE ET GÉNIE CHIMIQUE

ÉCOLE POLYTECHNIQUE FÉDÉRALE DE LAUSANNE

POUR L'OBTENTION DU GRADE DE DOCTEUR ÈS SCIENCES

PAR

Robert PLASS

ingénieur chimiste diplômé EPF
de nationalité suisse et originaire de Versoix (GE)

acceptée sur proposition du jury:

Prof. M. Grätzel, directeur de thèse
Dr A. Goossens, rapporteur
Prof. G. Hodes, rapporteur
Prof. L. Zuppiroli, rapporteur

Lausanne, EPFL
2004

Meinen Eltern

Acknowledgements

Abstract

Over the past fifteen years dye-sensitised nanocrystalline solar cells have been the subject of intense research and development efforts. These systems provide a technically and economically credible alternative to classical p-n junction solar cells, reaching over 10 % certified efficiency under standard solar illumination conditions (AM 1.5, 1000 W/m^2).

Recently, the liquid electrolyte, commonly used in these dye-sensitised solar cells, could successfully be replaced by a novel solid hole-conducting material (spiro-OMeTAD). The absence of volatile solvents and corrosive components like iodine presents a clear advantage of these solid-state devices over their photoelectrochemical counterparts. Yet, their maximum overall efficiency of about 3 % clearly lacks behind the performance features of classical dye-sensitized solar cells.

The objective of this work is the replacement of the usually used sensitiser (transition metal complexes and organic dyes) by quantum-dots. It was motivated by the possibility to achieve panchromatic light absorption due to the size-dependent properties of the quantum-dots. Some studies have been published using quantum-dots of inorganic low-bandgap semiconductors as sensitisers for mesoporous wide bandgap semiconductor electrodes in conjunction with liquid electrolytes. These systems often suffer from corrosion and photo-corrosion mainly due to the aggressive nature of the electrolyte employed. Solid-state organic-inorganic heterojunctions might provide the desired environment for quantum-dot sensitisation, as the environment is much less aggressive.

A large variety of inorganic quantum-dot materials like PbS, CdS, PbSe and CdSe were scrutinized for their use as sensitisers. All particles were synthesised in situ on the TiO_2 surface using two different techniques: dip-coating and chemical bath deposition. Lead sulphide was the most investigated due to its superior photovoltaic characteristics. High Resolution Transmission Electron Microscopy (HRTEM) of PbS sensitised TiO_2 electrodes fabricated via dip-coating clearly showed the distinct particles on the surface of the semiconductor.

The electron transfer dynamics following optical excitation of quantum-dot sensitized TiO_2/spiro-OMeTAD heterojunctions were thoroughly studied. Fluorescence spectroscopy was used to prove the possible electron injection from the PbS into the

TiO$_2$. Nanosecond laser spectroscopy was applied to monitor the interfacial recombination of the injected electron and the oxidised hole-conductor. Femtosecond laser spectroscopy allowed measuring the ultra-fast kinetics in the system, including electron trapping, exciton recombination and PbS regeneration. An overall efficiency of 0.5 % at 0.1 sun (AM 1.5) has been reached with such systems.

Chemical bath deposition (CBD) of PbS leads to the formation of a layer rather than distinct particles on the TiO$_2$. Solar cells fabricated via CBD exhibited open-circuit voltages which were generally 100 mV higher then those of comparable devices made via dip-coating. The PbS layer acts as blocking layer, hindering the contact between TiO$_2$ and the hole-conductor. This technique allowed achieving devices highly linear with respect to the illumination power.

Different strategies were pursued to impede interfacial recombination, among which the introduction of self-assembled monolayers at the interface between the organic and inorganic phases was proven to be the most efficient. Nanosecond laser spectroscopy showed a strong decrease of the interfacial recombination kinetic rates in the presence of hexadecylmalonic acid or decylphosphonic acid monolayers. Short-circuit currents could be raised by a factor two to four using such type of molecules. The overall efficiency of the device could be strongly increased, reaching 1 % at 0.1 Sun (AM 1.5).

CBD was also used to deposit PbSe and CdSe layers at the surface of TiO$_2$. Fluorescence spectroscopy was used to probe electron injection from CdSe quantum dots to TiO$_2$. Generally it was observed that metal sulfides were more efficient in sensitizing TiO2/OMeTAD heterojunctions then the respective selenides.

Résumé

Dans les quinze dernières années, la recherche ainsi que le développement des cellules nanocristallines à colorant ont été très intenses. Ce type de systèmes est une alternative crédible aux dispositifs classiques à jonction p-n, tant sur le point de vue économique que technique. Des rendements de conversion sous des conditions standard d'illumination (AM 1.5, 1000 W/m^2) de plus de 10 % ont été mesurés et certifiés. Récemment, l'électrolyte liquide utilisé usuellement dans les cellules nanocristallines à colorant a été remplacé avec succès par un nouveau matériau solide conducteur de trous (Spiro-OMeTAD). L'absence de solvants volatiles et de composés corrosifs tels que l'iode est un clair avantage des systèmes solides par rapport au systèmes conventionnels. Néanmoins, leur rendement maximum de 3 % se trouve loin des performances des cellules classiques sensibilisées par colorants.

L'objectif de ce travail est le remplacement des colorants couramment utilisés (complexes de métaux de transitions et colorants organiques) par des nanoparticules. La principale motivation étant la possibilité d'avoir une absorption panchromatique grâce aux propriétés des nanoparticules dépendantes de leur taille. Certaines études ont été publiées, rapportant l'utilisation de nanoparticules (quantum-dots) comme sensibilisateur. Ces systèmes souffrent souvent de la corrosion et de la photo-corrosion, dû à la nature agressive de electrolyte. Les systèmes solides basés sur une junction organique/inorganique présentes un environnement nettement moins agressif, adéquat à la sensibilisation par nanoparticules.

Différents types de nanoparticules inorganiques ont été testés, comme PbS, PbSe, et CdSe. Toutes ces particules ont été synthétisé in-situ sur la surface du TiO$_2$, en utilisant deux techniques ; le trempage successive, et la déposition par bain chimique (CBD). PbS fût étudié très en détails dû à ces meilleures performances photovoltaïques. La microscopie électronique à transmission (HRTEM) a permis de mettre en évidence l'existence des particules distinctes de PbS à la surface du TiO$_2$.

La dynamique du transfert d'électrons succédant à l'excitation lumineuse à la junction hétérogène TiO$_2$/spiro-OMeTAD sensibilisée par des nanoparticules a été étudiée avec une grande attention. La spectroscopie de fluorescence prouva que l'injection d'un électron du PbS dans le TiO$_2$ est possible. La recombinaison interfaciale entre l'électron injecté et le conducteur de trous oxydé fut quantifiée par des mesures de

spectroscopie laser nanoseconde. Les réactions ultra-rapides comme le trappage d'électron, la recombinaison de l'exciton, et la régénération du PbS furent observées grâce à la spectroscopie laser femtoseconde. Un rendement de 0.5 % sous une intensité lumineuse 10 % de soleil (AM 1.5) fut atteint avec de tels systèmes.

La déposition par bain chimique (CBD) de PbS permet la formation d'une couche à la surface du TiO_2, plutôt que la formation de particules distinctes. Le potentiel à circuit ouvert pu être augmenté de 100 mV par rapport aux cellules préparées avec la technique des trempages successifs. Il apparaît que la couche de PbS agit comme couche bloquante, évitant le contact entre le TiO_2 et le conducteur de trous. Cette technique permet d'obtenir des échantillons dont le rendement est très linéaire en fonction de la puissance d'illumination

Différentes stratégies furent employées afin de minimiser la recombinaison interfaciale. Parmi celles-ci l'introduction d'une mono-couche à l'interface entre les phases organique et inorganique fût la plus probante. Des mesures de spectroscopie laser nanoseconde ont montré que la vitesse des cinétiques de recombinaison interfaciale a pu être fortement réduite grâce à la présence de l'acide hexadecylmalonique ou de l'acide decylphosphonique. Les courants de court-circuit furent augmentés d'un facteur deux à quatre grâce à ces molecules. Le rendement de conversion a ainsi pu être augmenté de manière significative pour atteindre 1 % à 0.1 soleil (AM 1.5).

CBD fut également utilisée pour déposer des couches de CdSe et de PbSe à la surface du TiO_2. La spectroscopie de fluorescence prouva que l'injection d'électron est possible depuis les particules de CdSe dans le TiO_2. Il fut généralement observé que les sulfides de métaux furent plus efficaces pour la sensibilisation de jonctions hétérogènes que les selenides équivalents.

Zusammenfassung

In den fünfzehn letzten Jahren, wurden farbstoffsensibilisierte nanokrystalline Solarzellen intensiv erforscht und entwickelt. Diese Systeme sind eine technisch und wirtschaftlich glaubwürdige Alternative zu klassischen, auf p-n Junktion basierten, photovoltaischen Systemen. Sie erreichen einen zertifizierten Wirkungsgrad von über 10 % unter standardisierter Beleuchtung (AM 1.5, 1000 W/m^2). Kürzlich wurde der in der farbstoffsensibilisierten Zelle benutzte flüssige Elektrolyt erfolgreich durch einen neuen Festkörper-Lochleiter (spiro-OMeTAD) ersetzt. Die Abwesenheit von volatilen Lösungsmitteln und korrosiven Komponenten wie Jod ist ein klarer Vorteil dieser soliden Systeme gegenüber den konventionellen Systemen. Die erreichten Wirkungsgrade von etwa 3 % sind jedoch deutlich niedriger als die Leistung der klassischen farbstoffsensibilisierten Zelle.

Das Ziel der vorliegenden Arbeit ist die Ersetzung des gewöhnlich verwendeten Farbstoffs (Uebergansmetallkomplexe und organische Farbstoffe) durch Nanoteilchen. Es wurde von der Möglichkeit panchromatischer Lichtabsorption durch die grössenabhängigen Eigenschaften der Nanoteilchen Gebrauch gemacht. In einigen Veröffentlichungen wurde die Benutzung von Nanoteilchen (quantum-dots) als Sensibilisator bereits untersucht, jedoch litten diese Systeme meistens unter Korrosion und Photokorrosion wegen der aggresiven Natur der gebrauchten Lösungsmittel. Solide Heterojunktion-Systeme könnten, wegen des weniger aggressiven Umfeldes, ideal für die Sensibilisierung durch Nanoteilchen sein.

Verschiedene Typen von Nanoteilchen, wie zum Beispiel PbS, CdS, PbSe oder CdSe, wurden getestet. Diese Teilchen wurden in situ auf das TiO$_2$ synthetisiert, wozu zwei verschiedene Methoden verwendet wurden: „dip-coating" und „chemical bath deposition" (CBD).

PbS-sensibilisierte Systeme wurden wegen ihrer hervorragenden photovoltaischen Charakteristiken am meisten erforscht. Untersuchungen am hochauflösenden Transmissions-Elektronenmikroskop (HRTEM) von mittels dip-coating mit PbS sensibilisierten TiO$_2$ Elektroden zeigten eindeutig einzelne Teilchen auf der Oberfläche des Halbleiters.

Die Elektronentransfer-Dynamik nach optischer Anregung der mit quantum-dots sensibilisierten TiO$_2$/spiro-OMeTAD Heterojunktion wurde gründlich untersucht.

Durch Fluoreszenz-Spektroskopie konnte die Elektroninjektion vom PbS in das TiO_2 nachgewiesen werden. Nanosekunden-Laser-Spektroskopie zeigte die Grenzflächen-Rekombination zwischen dem injizierten Elektron und dem oxydierten Lochleiter. Femtosekunden-Laser-Spektroskopie erlaubte es, die Systemkinetik ultra-schneller Vorgänge zu beobachten, wie zum Beispiel die Rekombination des Excitons oder die Regeneration des PbS. Umwandlungswirkungsgrade von 0.5 % bei einer Intensität von 0.1 Sonne (AM 1.5) wurden mit solchen Systemen erreicht.

Die Abscheidung von PbS nach der „CBD"-Methode erlaubt die Bildung einer Schicht anstatt einzelnen Teilchen an der TiO_2 Oberfläche. Die Leerlaufspannung des Systems konnte durch diese Methode um 100 mV erhöht werden im Vergleich mit dip-coating Elektroden. Die PbS Schicht fungiert als blockierende Lage, da sie den Kontakt zwischen TiO_2 und Lochleiter verhindert. Diese Methode erlaubte es, Zellen mit sehr linearem Verhalten als Funktion der Beleuchtungsintensität zu erzeugen.

Verschiedene Strategien wurden verfolgt um die Grenzflächenrekombination zu vermindern. Von diesen war die Einführung einer mono-molekularen Schicht an der Grenzfläche am wirksamsten. Nanosekunden-Laser-Spektroskopie zeigte eine starke Reduzierung der Geschwindigkeit der Grenzflächenrekombination in der Anwesenheit von Hexamalonsäure und Decylphosphonsäure. Kurzschlussströme konnten um einen Faktor zwei bis vier, je nach Molekül, erhöht werden. Ein Wirkungsgrad von 1 % unter einer Intensität von 0.1 Sonne (AM 1.5) konnte mit solchen Systemen erreicht werden.

CBD wurde auch für die Abscheidung von PbSe und CdSe Schichten verwendet. Fluoreszenz-Spektroskopie zeigte die Elektroneninjektion vom CdSe in das TiO_2. Generell konnte beobachtet werden, dass die Metallsulfide das TiO_2/spiro-OMeTAD System besser sensibilisieren als die Metallselenide.

Table of Contents

x

Chapter I

Introduction

For many thousand of years till about three hundred years ago, mankind used exclusively renewable energy sources (with a minor exploitation of coal). Wood was used for heating, animals were used for transportation, and wind and water supplied mechanical energy. During the 19th century, the industrial revolution brought new machines and new energetic needs; coal was found to satisfy the increasing demand of energy. The early 20th century saw the first exploitation of petroleum, natural gas and later, nuclear energy as energy sources to cover the continuously growing demand. Nowadays, fossil energies cover 95 % of the total energy demand worldwide, which exceeds 10^5 TWh per year.

Global energy consumption draws from six primary sources: 44 % petroleum, 26 % natural gas, 25 % coal, 2.5 % hydroelectric power, 2.4 % nuclear power, and 0.2 % non-hydro renewable energy[1]. Between 1980 and 2001, worldwide consumption of petroleum, coal, and natural gas increased by 22, 27, and 71 % respectively. Following the projected energy needs, this will increase by nearly 50 % in the 25 next years. About 30 % of the primary energy is converted to electricity either in the course of initial harvesting (as for hydroelectric, wind, solar and geothermal) or by combustion (as for fossil, and biomass); about 75 % of the primary energy arrives, in one form or the other, at the consumer.

As estimates of non-commercial energy use are incomplete and unreliable, the above estimates do not include nonmarket wood used as fuel and farm residues that are prevalent in many countries. The international energy agency (IEA) suggests that

biomass still provides on average one-third of the energy needs in Africa, Asia, and Latin America, and as much as 80 to 90 % in the poorest countries of these regions. While the average yearly energy consumption per capita in developing countries is about 10 MWh (with about 1 MWh in the poorest!), the yearly consumption in Europe amounts to about 50 MWh and in the USA to 90 MWh per capita. The energy consumption can be classified by sectors, as shown in Figure 1.1; the most important ones are residential, transportation, and industry. The importance of these sectors differs between developing and developed countries. For example, transportation in the developed countries accounts for 35% of the total energy consumption, whilst in the developing ones roughly 18%.
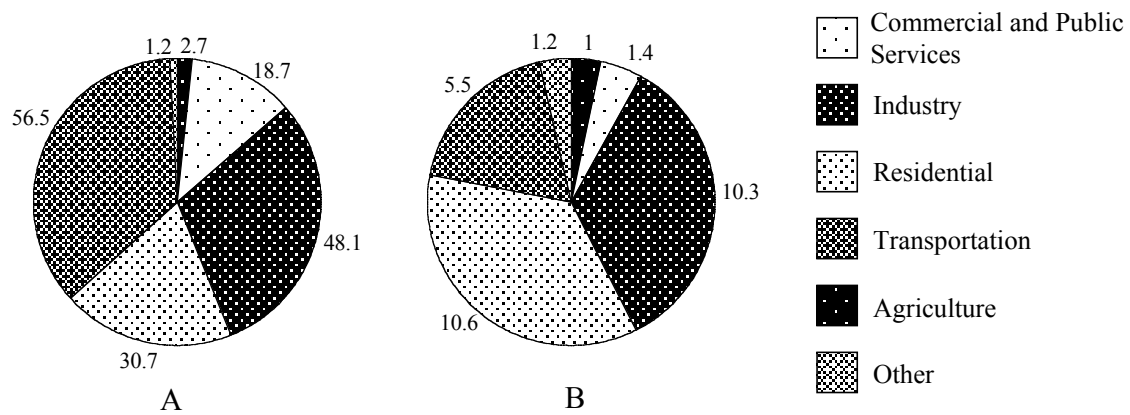
Figure 1.1: Per-capita energy consumption by sectoral end use in (A) the developed world and (B) the developing world (in gigajoules)[1].

Although estimates vary, economically recoverable fossil fuel reserves include almost one trillion tons of coal, more than one trillion barrels of petroleum, and over 150 trillion cubic meter of natural gas. Roughly 3 million tons of uranium reserves are known. Annually, the world consumption of coal is about 0.5% of the reserves, of natural gas around 1.6% of reserves, whereas oil almost 3% of reserves, and nuclear electricity generation consumed the equivalent of 2% of uranium reserves.

Large fossil fuel reserves are concentrated in a small number of countries, with a large number of developing countries having no reserves at all. Many energy-lacking countries have become highly developed through sufficient access to international energy markets. Conversely, some countries possess substantial reserves but remain rather poor. This shows that the possession of reserves is not a sufficient condition to

a country's development unless there is an adequate economic system able to transform these energy resources into general social wealth.

Major changes in the global climate must be expected as a consequence of the carbon dioxide emissions from burning fossil fuels, which at present are of the order of 6.6 billion tons[1] carbon equivalent and still rising. These emissions lead to an enhancement of the atmospheric CO_2 concentration, passing from 280 ppm in 1850 to nearly 370 ppm in 2000[2] and to an increase in global mean temperature of nearly 1°. Fossil fuel consumption also results, to a lesser extent, in the emission of other greenhouse gases (GHG's), such as carbon monoxide, methane, and volatile organic compounds, and the rising ocean temperature increases evaporation and hence the water vapour content in the atmosphere. The Intergovernmental Panel on Climate Change (IPCC) predicts, based on climate models, that continued emissions of anthropogenic GHG's will result in not only increasing mean temperatures but also in more frequent extreme climate events which will have significant consequences for ecosystems but also for human activities, including the flooding of low-lying land due to the thermal expansion of the ocean.

The United Nations, recognizing these threats, have organized the conclusion, at the Conference in Rio in 1992, of the Framework Convention on Climate Change, which has been ratified by all participating countries. After 10 years of negotiations, targets numbers for the reduction of CO_2 emissions for countries or groups of countries have been defined at the 2002 Conference at Kyoto, which however, have not yet been ratified by the main CO_2 emitter, the USA and, several other countries.

Technically, reductions in the emissions of CO_2 can be achieved by the enhanced introduction into our energy system of nuclear energy or of renewable energy sources as discussed in Section 1.1.

Nuclear energy, i.e. the binding energy of the nucleus, can be set free either by fission of the very heavy nuclei (Th, U) or by fusion of light nuclei (^{1}H, ^{2}H, ^{3}H) to Helium. While nuclear fusion is still a subject under development and will, in the opinion of experts, take the order of 50 years to reach a state of useful energy production, nuclear fission is being exploited in approx. 430 reactor units worldwide with a total capacity of about 350 GW (electr.). The construction of new reactors continues to meet at present strong opposition by part of the population because of the fear of nuclear run-

---

[1] 1 ton carbon equivalent = 3.66 tons of CO_2

away. However the run-away risk after several thousands years of integrated (over all existing reactors) run-time is, very small compared to the risks taken by the individual in every-day life (e.g. in road traffic). The development of inherently safe nuclear reactors (which by their very construction cannot undergo thermal excursion), stopped in Germany some 10 years ago, has in recent years been taken up in several countries. The duration of the resources of uranium could be considerably extended by reprocessing of the used fuel elements.

The radioactive wastes occurring from this energy production give rise to a storage problem, as the decomposition of those takes several billion of years. Nevertheless the amount of wastes are small (15 m^3 per year for a 1 GW installation) and the estimate cost for long-time and safe storage is roughly 10 % of the total supply cost of the fission material.

I.1   Renewable energies

Planet Earth receives from the sun an almost constant flux of radiation, which with clear sky and dry air amounts to about $1kW/m^2$. All sources of renewable energies depend either directly or indirectly from the sun's radiation. Although of lesser importance, geothermal energy sources (which derive their energy from the nuclear decay in the earth) and tidal energy (due to the gravitational forces between earth and moon) should also be practically inexhaustable.

Sunlight, or solar energy, can be used directly for heating, lighting, generating electricity and many other applications. Indirectly, sun's heat also creates winds, whose energy is used to generate electricity by wind turbines. Sunlight causes plants to grow. The organic matter composing those plants is known as biomass. Biomass can be used to produce electricity, transportation fuels for example. On the other hand, geothermal energy traps the Earth's internal heat and can be used for a large variety of applications such as building heating and electricity production. Ocean energy can under favourable conditions be used for the production of electricity.

I.1.1   Solar energy

A large variety of techniques are available or under development to benefit from the solar energy, including photovoltaic systems, concentrating solar power, passive solar systems, solar hot water, and solar process heat.

Photovoltaic solar cells are used to directly convert light energy into electricity, and have been available for many years; major applications like solar panels on satellites made them famous, and smaller uses like calculator or watch energy supply, known by everyone. They are based on the photovoltaic effect, which allows the conversion of light (photons) to electricity (electrons). Active research is going on in this domain and will be described in more detail in section 1.2.

Concentrating solar power can be achieved by several types of systems, which share a feature that the incident solar radiation is concentrated onto a small surface. A fluid (often oil) flows through this small surface to be heated; this heat is then used to produce steam, which drives turbines, generators then create electricity. The different types of plants are shown on Figure 1.2. Parabolic trough reflector systems totalling about 350 MW are already in use in the United States and development of all three types are under way in Europe.

Parabolic dish reflector   Parabolic trough reflector   Heliostat reflectors

Receiver   Receiver   Receiver
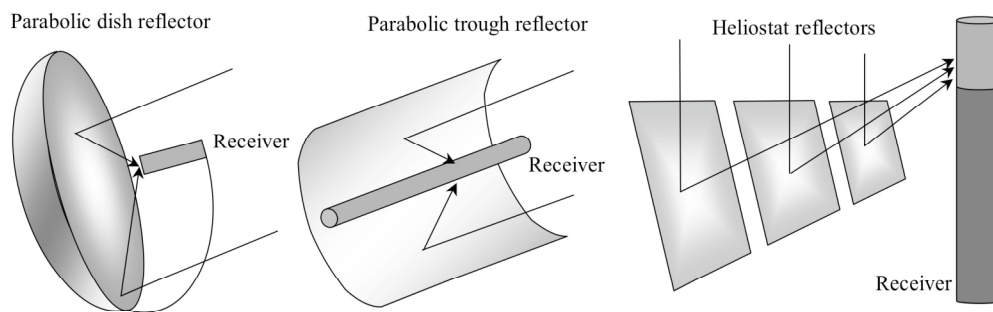
Figure 1.2: Three main types of solar concentrating collector plants

Solar chimney technology is created when the sun's radiation is used to heat a large body of air, which is then forced to move as a hot wind through turbines to generate electricity. A huge project is in development in northern Australia; a 7 km diameter transparent roof with at its center a tower (170 m in diameter and 1000 m in height) should reach a maximal power of 200 MW.

Passive heating of buildings can be achieved by installing large windows on the south side as they receive most sunlight. More efficiently, a sunspace (similar to a greenhouse) is built on the south side of a building with ventilation allowing the heat to circulate into the building.

Hot water can rather easily be produced from solar energy and stored in well-insulated tanks. Most common is the flat-plate, consisting of a set of tubes under a transparent cover, easily mounted on roofs.

I.1.2   Hydroelectric power

Water wheels have been driving mills and heavy tools for many centuries. Currently, hydroelectric power is the world's largest renewable source of electricity, accounting for about 15% of the world's electricity. Even if hydroelectric energy does not release any standard atmospheric pollutants, the impact of this technology on the environment is not negligible. The most obvious one is the flooding of large areas of land, much of it previously forested or used for agriculture. Damming a river alters the amount and quality of water in the river downstream of the dam, as well as preventing fish from migrating upstream to spawn; on the other hand, it protects land downstream against flooding.

I.1.3   Wind energy

Again, wind energy has been used for many centuries for the pumping of water and grinding grain, using windmills. Some 200,000 windmills could be counted in Europe in the 18th century. Their modern equivalent, called wind turbines, use wind energy to generate electricity. Different types of turbines exist, the most common ones are the horizontal axis turbines which are mounted on towers, reaching 80 meters height, designed to take advantage of faster and more stable winds. The biggest units can produce up to 5 MW. Vertical axis turbines also exist but are not in wide use. Wind turbines range from single turbines for homeowners to large wind farms with hundreds of turbines providing electricity to the power grid. According to the American Wind Energy Association (AWEA)[2] at the end of 2002 the total production capacity reached over 31000 MW worldwide; on a percentage basis wind is the fastest growing energy source with an annual increase of over 30% per year in the five last years. 75 % of the total production takes place in Europe: Germany, Denmark, Spain, and the U.K. are the principal producers (89 %). In Denmark, wind energy meets 20 % of the country's electricity needs, in Germany 4.5 % of electricity is generated using wind.

---

[2] www.ewea.org

I.1.4   Biomass energy

Mankind has been using biomass energy for thousand of years, since people started burning wood to cook food or to keep warm. Biomass refers to any plant-derived matter available on a renewable basis, including dedicated energy crops and trees, agricultural food and feed crops, agricultural crop wastes and residues, wood wastes and residues, aquatic plants, animal wastes, municipal wastes, and other waste materials. Bioenergy is used to produce a large array of products like electricity, solid, liquid and gaseous fuels, heat, and chemicals. Of course by burning organic materials CO_2 is released in the atmosphere, but the same amount of CO_2 is actually removed when new plants are growing. The net emission of CO_2 will be zero as long as plants continue to be replenished for biomass energy purposes. Biomass can be directly converted into liquid fuels, mainly ethanol and biodiesel to be used for transportation needs. Biopower is the use of biomass to generate electricity. Most of the biopower plants use direct burning of the biomass for steam production, to drive a generator to produce electricity. Biobased products include green chemicals, renewable plastics, natural fibers and natural structural materials. Many of these products can replace products and materials traditionally derived from petrochemicals, but new and improved processing technologies will be required.

Bioenergy accounts for 3 % of the primary energy production in the United-States, being in second rank after hydropower in renewable primary energy production. In Europe, wood accounts for more than half of the renewable primary energy production, excluding hydropower. Great efforts are made to increase the production of biogas and biofuels, an annual growth of 30 % is expected until 2010[3].

I.1.5   Geothermal energy

Geothermal energy uses the heat of earth for the production of electricity, for the direct use of the hot water for heating, and for geothermal heat pumps, which are used to heat and cool buildings. Geothermal energy is not easily accessible all over the world; however some countries take great advantage of this energy. In Iceland geothermal energy provides half of the total energy consumption, the other half being provided by hydropower; it is principally used for space heating (85 % of the households).

I.1.6   Ocean energy

Ocean energy draws on energy of the ocean waves, currents and of tides. One estimates that the power of the waves breaking on the world's coastlines is around $2*10^6$ MW, but it is very expensive to collect. A dam is typically used to convert tidal energy into electricity by forcing the water through turbines, activating a generator. The largest plant worldwide is located in France on the river La Rance. Its power production is 240 MW and has been operating since 1966. Recently, tests have begun to extract some electricity from strong ocean currents by turbine/generator sets submerged at a certain depth.

A great amount of thermal energy is stored in the world's oceans, which daily receive heat from the sun equal to the thermal energy contained in 250 billion barrels of oil. The useful temperature difference is however too small for converting some of this enormous amount of energy into electricity.

I.2   Photovoltaic systems

The photovoltaic effect is the basic physical process through which a solar cell converts sunlight into electricity. In 1839, Edmund Becquerel discovered the photovoltaic effect while experimenting with an electrolytic cell made up of two metal electrodes. He found that certain materials would produce small amounts of electric current when exposed to light[4].

Nowadays the solar cell market is fast growing, with a growth of over 30% per year. In 2002 a world record for solar photovoltaic installations of 440 MW was reached. In spite of the complicated manufacture and high cost, crystalline silicon still dominates the market today. The market share of silicon-based solar cells is nearly 99%, comprising single crystal, polycrystal, and amorphous silicon. Nevertheless active research is going on to replace silicon, as the production of such devices consumes enormous amounts of energy mainly for the purification of the raw material. Indeed, the semiconductors employed must be highly pure and defect-free to avoid premature recombination of electrons and holes.

A very challenging technology is based on ternary compound semiconductors $CuInSe_2$, $CuGaSe_2$, $CuInS_2$. The first work[5] on $CuInSe_2$ (CIS) was extremely promising but the complexity of the material looked complicated as a thin-film technology. Later it became evident that CIS process technology is very flexible with

respect to process conditions[6]. Vapour deposition is used for the fabrication of such devices. Nowadays laboratory cells reach nearly 19 % overall efficiency and bigger modules achieve up to nearly 17 % efficiency.

Thin-film solar cells based on CdTe are the cells with the longest history, but they took a long time to achieve a breakthrough in terms of their conversion efficiency. In 1993, researchers from the National Renewable Laboratory (NREL) achieved an efficiency in the range of 16 %[7]. The pn-junctions was composed on one side of p-CdTe and on the other side of n-CdS. This type of cells accounts for a 0.5 % of the market share of the photovoltaic materials.

Nanocrytalline dye sensitised solar cells are a new type of device where in contrast to Si and CIS cells the functional element, which is responsible for light absorption, is separated from the charge carrier transport itself. These devices are discussed in detail in the next section.

I.3   The dye-sensitised solar cell

The first work on semiconductor sensitisation was reported by Vogel[8]. From 1873 he investigated the sensitisation of silver halide emulsions with dyes, finding the photoresponse significantly extended into the red and even infrared. He applied his findings to photography. In 1887, Moser[9] carried this concept to the photoelectric effect by using the dye erythrosine on silver halide electrodes. Until the 1960's, the theoretical understanding of the process was under dispute. It was not clear whether the mechanism was an electron transfer or an energy-coupling process. The electron injection process was proved by Tributsch and Gerischer with their work on ZnO in 1968[10]. In the following years, the chemisorption of the dye on the surface of the semiconductor was developed to enhance the function of the dye[11,12]. The concept emerged to use dispersed particles to provide an enhanced surface interface[13], then photoelectrodes with high surface roughness were employed, and TiO_2 became the semiconductor of choice[14,15]. The material has many advantages; it is inexpensive, non-toxic, abundant, and is already widely used in many health care products. Thanks to system optimisation, a conversion efficiency of 7.1 % was announced in 1991[16]. This evolution has continued since then and certified efficiencies over 10 % have now been reached.

Figure 1.2 shows the principle of operation of the dye-sensitised solar cell (DSSC).

The TiO$_2$ is the center of the device; it is composed of nanoparticles, which have been sintered together to establish electric contact. An electron is injected into the conduction band of the semiconductor after photoexcitation of the dye attached to the nanocrystalline surface. The reduced dye is regenerated by electron donation from the electrolyte, usually an organic solvent containing the iodide/triiodide couple. The electrolyte itself is regenerated at the counter electrode by reduction of the triiodide, the circuit being completed through the external load.
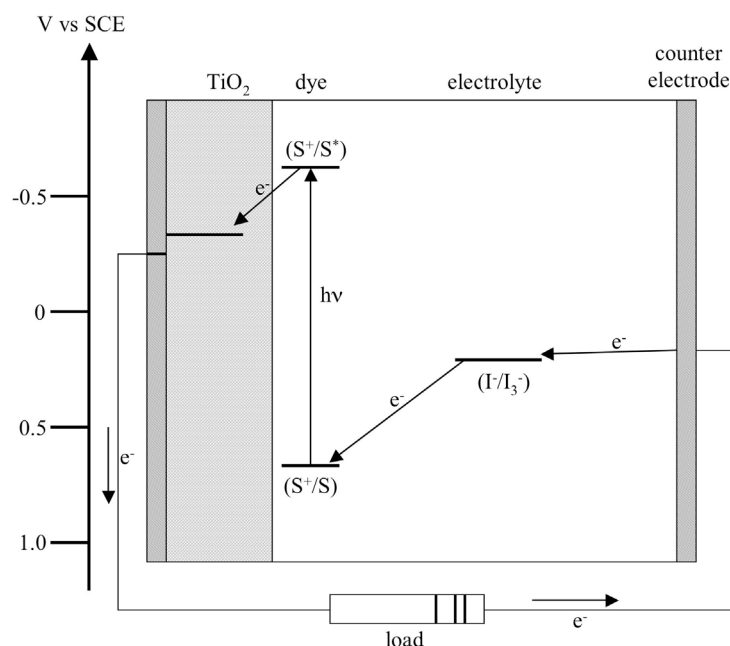
Figure 1.2: Principle of operation and energy level scheme of the dye-sensitised nanocrystalline solar cell.

In a conventional pn-junction photovoltaic cell based for example on silicon, the semiconductor assumes simultaneously two functions. First, it has to absorb the incident sunlight to create an electron-hole pair, and then it has to transport the produced charge carriers. This is the most fundamental difference between the two systems, Figure 1.3 shows a simplified energy band scheme for silicon pn-junction solar cells.
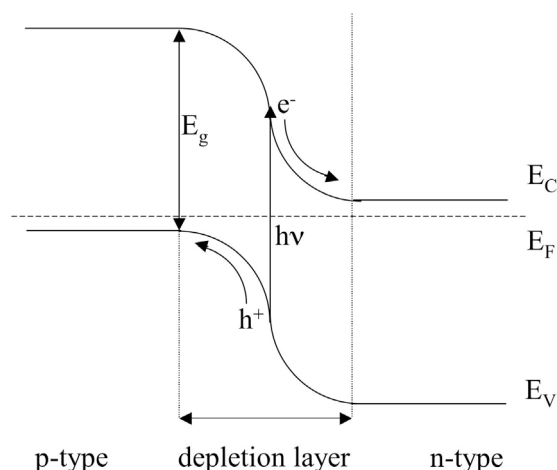
Figure 1.3: Energy band sheme of a pn-junction solar cell, where E_C, E_F, E_V are the energy levels of the conduction band, of the Fermi level and of the valence band respectively. E_g being the semiconductor bandgap.

Good efficiency is reached by producing the charge carriers inside the depletion layer where under the effect of an electric field the charges are separated. To avoid recombination between the created electron and hole, no defects in the solid should be present. As only highly pure materials are defect-poor, this renders solid-state materials of the conventional types expensive. In other words, the pn-junction is characterised by the presence of minority and majority charge carriers in the same volume whereas in the DSSC the electrons are transported by the TiO_2, and the holes in the electrolyte. Only majority charge carriers are present in the same volume, thus the recombination process is hindered and can only occur at the interface.

Even though, unexpected problems arose from the corrosive and the volatile nature of the liquid electrolyte. The sealing of such devices turned out to be much more complicated than for conventional systems due to the characteristics of the solvent. A lot of work is being invested into finding alternative, less volatile electrolytes. Different types of compounds have been used such as; molten salts[17], p-type semiconductors such as CuI[18,19] ,or CuSCN[20,21].

I.4   The solid-state dye-sensitised solar cell (SSD)

The replacement of the liquid electrolyte by an organic charge transport material forms a solid-state dye-sensitised organic/inorganic heterojunction. These types of heterojunctions have already been known for several years. First attempts tried to use hole conducting materials such as TPD, a molecule which is known since the mid-

80's[22], resulting in photocurrents in the nanoampere range. The charge transport mechanisms inside the cell are very similar to the DSSC, except for the electrolyte. In the SSD, contrary to the DSSC, no ions are migrating inside the electrolyte. The electrons are hopping from one hole-conductor molecule to the other, as shown on Figure 1.4.
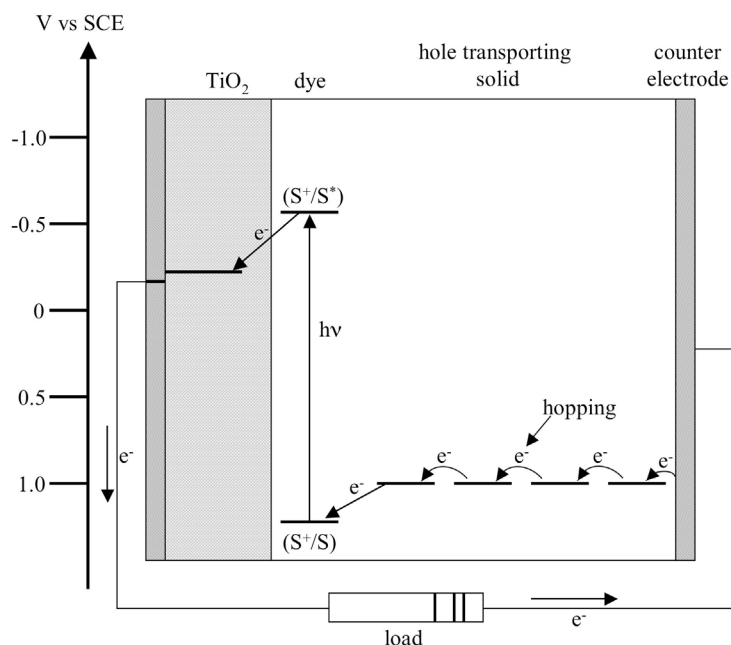
Figure 1.4: Principle of operation and energy level scheme of the solid-state dye sensitised solar cell

A significant breakthrough was achieved by using a new molecule, 2,2'7,7'-tretakis(N,N-di-p-methoxyphenyl-amine)-9,9'-spirofluorene (spiro-OMeTAD). Maximum light conversion efficiency was measured to be 0.74 % at full sun illumination (AM 1.5, 100 mW/m^2)[23]. It was rapidly established that the interfacial recombination was the principal loss mechanism. To further improve the performance of this type of device, this mechanism had to be better understood and recombination reduced to the minimum. The hole transport in the hole conducting material is much slower than for liquid electrolytes, due to the low electron mobility in these compounds. This leads to a hole concentration gradient between the interface and the bulk of the material. As the charges are removed from the surface, the whole interface will get charged, increasing the probability of interfacial recombination. Furthermore, the spiro-OMeTAD cannot achieve a perfect pore filling due to its large size, contrary to the electrolyte cell where the interpenetration is complete. This phenomenon will also enhance the interface charging effect. It was shown that the use of additives in

the hole-conductor matrix could significantly reduce the interfacial recombination. Although the use of a doping agent and lithium salts was already known, the addition of 4-tertbutylpyridine (tBP) lead to a strong increase of the photovoltaic performance of the device. An overall certified conversion efficiency of 2.56 % (AM 1.5, 100 mW/m^2) was achieved by using tBP in the hole conductor matrix[24]. The introduction of tBP resulted in a strong increase in open circuit potential of the device. This effect was assigned to the blending of the hole conductor matrix by the tBP and the lithium salt. Due to the change of the dielectric constant of the solvant, more lithium salt could be dissolved in the hole conductor solution, increasing furthermore its effect. Finally, the presence of silver ions in the dye solution was shown to increase the dye uptake by nearly 40 %, offering an easy method to increase light harvesting[25]. The overall efficiency of the SSD was enhanced to 3.2 % at 100 % sun illumination (100 mW/cm^2), resulting from the simultaneous increase in short circuit current and open circuit potential. On one hand, increased dye uptake allows higher short circuit current. The silver ions were expected to assist the dye assembling on the TiO$_2$ surface as bridging elements between two thiocyanate ligands. On the other hand, the decrease of the interfacial charge recombination, due to the better coverage of the TiO$_2$ surface by the dye molecules (blocking electron back transfer) allows to increase both the open circuit voltage and the short circuit current.

I.5   Aims of the present work

The main objective of the present work is to replace the conventional organo-metallic dye by semiconductor nanoparticles, also called quantum-dots, in the SSD. The properties of such particles are size-dependant, and ruled by the quantum size effect, which will be explained in the following chapter. A panchromatic light absorption may be achieved by using such types of particles, as the absorption properties can be tuned easily by varying the size of particles. Previous studies of quantum-dot (QD) sensitisation have been reported but on liquid electrolyte systems[26,27].The nanoparticles will be synthesised in situ on the TiO$_2$ particles, as preliminary studies have shown that synthesised particles stabilised with an organic molecule, have a poor uptake on TiO$_2$.

This begins by giving a detailed explanation of the device structure and its preparation as well as a description of the experimental techniques. The results and discussion are

divided in three main parts; the metal sulfide sensitisation, the metal selenide sensitisation, and interface optimisation.

I.6   Bibliography

(1)   Chow, J.; Kopp, R. J.; Portney, P. R. *science* **2003**, *302*, 1528.

(2)   Global atmospheric concentration of CO_2, 1999.

(3)   Energy, E. C. F.
         http://europa.eu.int/comm/energy/res/sectors/bioenergy_en.htm.

(4)   Becquerel, A. E. *Comt. Rend. Acad. Sci* **1839**, *9*, 561.

(5)   Wagner, S.; Shay, J. L.; Migliora.P; Kasper, H. M. *Applied Physics Letters* **1974**, *25*, 434.

(6)   Kazmerski, L. L.; White, F. R.; Morgan, G. K. *Applied Physics Letters* **1976**, *29*, 268.

(7)   Britt, J.; Ferekides, C. *Applied Physics Letters* **1993**, *62*, 2851.

(8)   West, W. *Photogr. Sci. Eng.* **1974**, *18*, 35.

(9)   Moser, J. *Monatsh. Chem.* **1887**, *8*, 373.

(10)   Gerischer, H.; Tributsch, H. *Ber. Bunsenges. Phys. Chem.* **1968**, *72*, 437.

(11)   Dare-Edwards, M. P.; Goodenough, J. B.; Hamnet, A.; Seddon, K. R.; Wright, R. D. *Faraday Discuss. Chem. Soc.* **1980**, *70*, 285.

(12)   Tsubomura, H.; Matsumura, M.; Noyamaura, Y.; Amamyiya, T. *Nature* **1976**, *261*, 402.

(13)   Duonghong, D.; Serpone, N.; Gratzel, M. *Helvetica Chimica Acta* **1984**, *67*, 1012.

(14)   Desilvestro, J.; Gratzel, M.; Kavan, L.; Moser, J.; Augustynski, J. *Journal of the American Chemical Society* **1985**, *107*, 2988.

(15)   Vlachopoulos, N.; Liska, P.; Augustynski, J.; Gratzel, M. *Journal of the American Chemical Society* **1988**, *110*, 1216.

(16)   O'Regan, B.; Grätzel, M. *Nature* **1991**, *353*, 737.

(17)   Papageorgiou, N.; Athanassov, Y.; Armand, M.; Bonhote, P.; Pettersson, H.; Azam, A.; Gratzel, M. *Journal of the Electrochemical Society* **1996**, *143*, 3099.

(18)   Tennakone, K.; Kumara, G.; Kottegoda, I. R. M.; Wijayantha, K. G. U.; Perera, V. P. S. *Journal of Physics D-Applied Physics* **1998**, *31*, 1492.

(19) Tennakone, K.; Kumara, G. R. R. A.; Wijayantha, K. G. U.; Kottegoda, I. R. M.; Perera, V. P. S.; Aponsu, G. M. L. P. *Semiconductor Science and Technology* **1998**, *13*, 134.

(20) O'Regan, B.; Schwartz, D. T. *Journal of Applied Physics* **1996**, *80*, 4749.

(21) O'Regan, B.; Schwartz, D. T. *Chemistry of Materials* **1998**, *10*, 1501.

(22) Stolka, M.; Yanus, J. F.; Pai, D. M. *J. Phys. Chem.* **1984**, *88*, 4707.

(23) Bach, U.; Lupo, D.; Comte, P.; Moser, J. E.; Weissörtel, F.; Salbeck, J.; Spreitzer, H.; Grätzel, M. *Nature* **1998**, *395*, 583.

(24) Krueger, J.; Bach, U.; Plass, R.; Cevey, L.; Piccirelli, M.; Grätzel, M. *Appl. Phys. Lett.* **2001**, *79*, 2085.

(25) Krueger, J. Interface engineering in solid-state dye-sensitized solar cells, EPFL, 2003.

(26) Gorer, S.; Hodes, G. *Studies in Surface Science and catalysis* **1996**, *103*, 297.

(27) Vogel, R.; Hoyer, P.; Weller, H. *J. Phys. Chem.* **1994**, *98*, 3183.

Chapter II

The Quantum Size Effect

II.1 What is a quantum dot?

Since beginning of the 1980's, research on nanocrystalline materials has developed into a large field in material science. The most striking feature of these materials is that their chemical and physical properties differ from those of the bulk solids. The reasons for this behaviour can be reduced to two fundamental phenomena. The first is the high dispersity of nanocrystalline systems; i.e. the number of atoms at the surface is comparable to the number of those which are located in the crystalline lattice. For example, a cluster with 55 atoms will have 76 % of the atoms at the surface, if it is constituted of 561 atoms only 45 % of those will be at the surface. The physical and the chemical properties, which are usually determined by the molecular structure of the bulk lattice, become dominated by the defect structure of the surface. In a wide variety of materials ranging from metals to semiconductors to insulators, a decrease in melting temperature was observed with decreasing particle size[1]. The melting point of CdS was shown to decrease from 1200 K for particles with a 4 nm radius to 600 K for particles with a 1.5 nm radius.

The second phenomenon arises from quantum mechanics where it is well known that electronic particles, confined by potential barriers to a space comparable or smaller than the De Broglie wavelength of the particles, have discrete allowed energy states rather than a continuum. For semiconductors, the critical dimensions below which quantization effects appear depend on the effective mass (m*) of the electronic charge

carriers. It can be shown that electrons and holes inside a semiconductor crystal respond to an electric field almost as if they were free particles in a vacuum, but with a different mass. This mass is called the effective mass and is usually stated in units of the ordinary mass of an electron m_e.

Since quantisation depends on spatial confinement, three different shapes can be defined where the confinement exists in one, two or three dimensions as shown in Figure 2.1. Confinement in one-dimension leads to quantum films, in two dimensions produces quantum wires and finally in three dimensions produces quantum particles often called quantum dots.
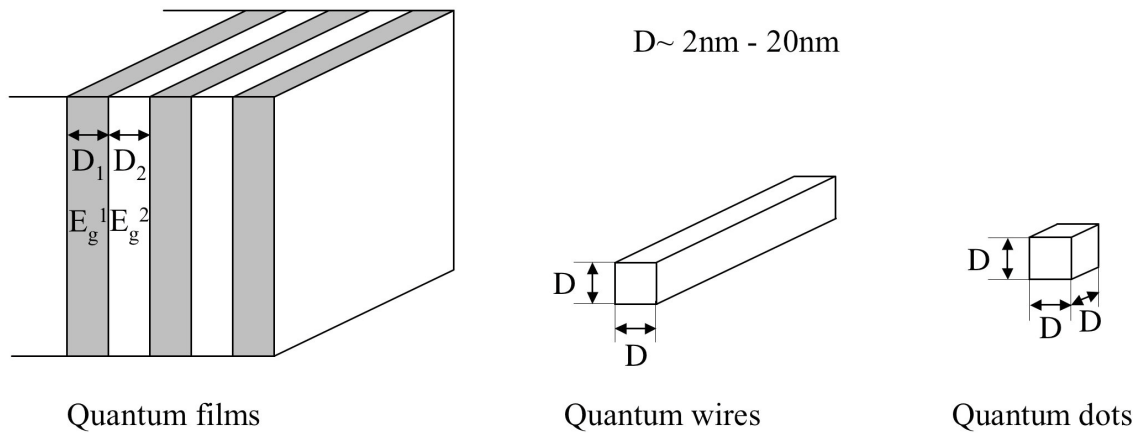
Figure 2.1: Three quantisation configuration types in semiconductor depending on whether the confinement exists in one, two or three dimensions (illustration taken from ref[2]).

The density of states (DOS) is quite different depending on the number of confined dimensions. For bulk materials the DOS is a continuous function, but when confinement appears quantisation arises, and thus for quantum films the DOS is a step function, for quantum dots the DOS is a series of discrete values, like a molecule or an atom. Finally, quantum wires have a DOS that is an intermediate between quantum films and quantum dots. The DOS of the three types of confinement regimes are shown in Figure 2.2 (Taken from ref[2]).
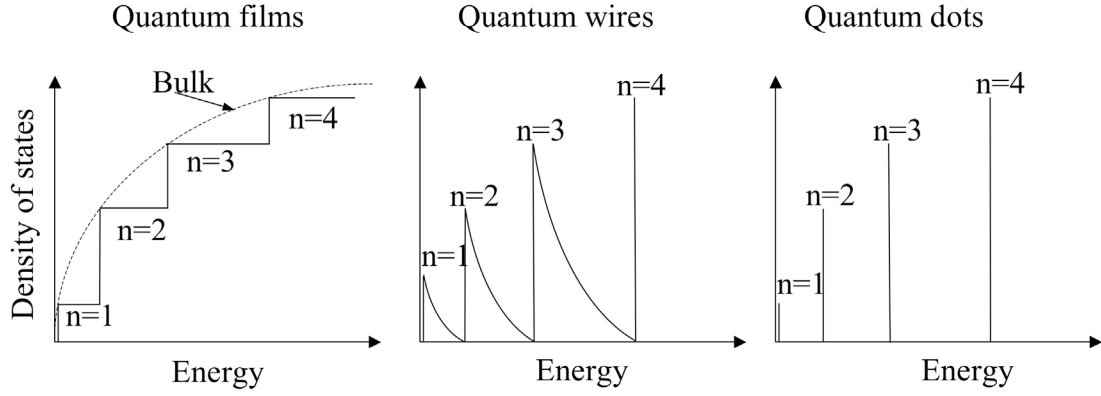
Figure 2.2: Density of states functions for quantum films, quantum wires, and quantum dots.

The existence of the quantum size effect in such small semiconductor nanoparticles was first reported in the early 1980's by Ekimov[3], Efros[4], and Papavassiliou[5]. Different theories were elaborated to calculate the band gap of a semiconductor at a given particle size.

II.2   The molecular orbital approach

A qualitative explanation to the fact that in small semiconductor particles the bands are discrete can be given by the linear combination of atomic orbitals-molecular orbitals approach (LCAO-MO), also called tight binding model[6]. One has to consider an N-atom infinite chain (e.g., an idealized polyacetylene) as the one-dimensional analog of the bulk solid. Recognizing the fact that an infinite chain is isomorphous with a cyclic group of infinite order[6], its energy levels can easily be obtained using the Hückel level as

$$E_j = \alpha + \beta \cos(2j\pi/N), \qquad j = 0, \pm 1, \pm 2, \ldots\ldots, \pm N/2, \qquad (2.1)$$

where E_j is the jth energy level, α the Coulomb integral, and β the resonance integral. This expression can be modified by introducing a new index k such that

$$E(k) = \alpha + \beta \cos ka, \qquad k = 0 \text{ to } \pm\pi/a. \qquad (2.2)$$

Here a is the unit cell length and $k = 2j\pi/Na$, called the wave vector. Figure 2.3 shows the plot of $E(k)$:
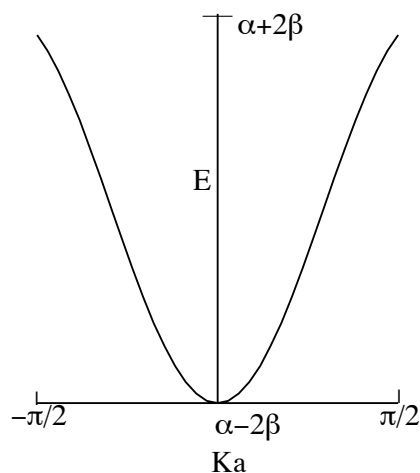
Figure 2.3: Plot of *E(k)* in function of *k*.

From this, the band structure of the idealized one-dimensional solid is obtained. The dispersion of the bands looks continuous, as N is infinite for this infinite chain. The quantized nature of the band can easily be seen when reducing N, as shown in Figure 2.4 for N=15 (15-annulene) and N=5 (cyclopentadiene):

$$E_j = \alpha + 2\beta \cos(2j\pi/15)$$

$$E_j = \alpha + 2\beta \cos(2j\pi/5)$$

15-annulene

cyclopentadiene
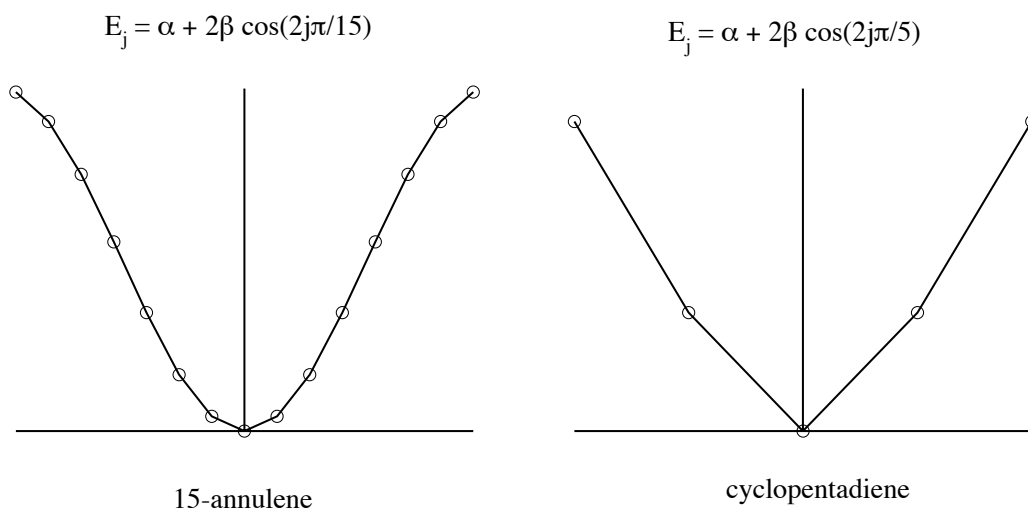
Figure 2.4: Plot of E_j as a function of j for small values of N.

The increasing space between the energy levels can easily be seen on this Figure and the discrete nature of the band becomes more and more prominent as *N* becomes smaller. This transition from the idealized polyacetylene through the annulene to cyclopentadiene provides a one –dimensional analog of the transition from solids to clusters and finally to molecules.

This model allows an easy understanding of the quantum size effect in semiconductors, but it lacks a quantitative theoretical treatment. In the following a

model will be given which calculates theoretical values for the band gap in small semiconductor particles.

II.3   Effective mass approximation

The theoretical background on quantized particles was first published by Brus et al[7-9]. They laid out the framework for understanding these effects from the point of view of molecular quantum chemistry. In II-VI and III-V semiconductors, the exciton can be described by a hydrogen-like model. This model incorporates the effective mass and the screening, described by the dielectric constant. Brus reasoned that unlike the situation in bulk materials, the photogenerated electron-hole pairs in small clusters could become physically confined. Confinement raises the electronic energy exactly as would be expected from the simple particle in a box model of quantum mechanics. The Schrödinger equation is often used to solve the one-dimensional problem of a particle subjected to a stepped potential energy function, where the energy is infinite everywhere expect for a finite line segment of length L. The equation under these conditions is:

$$\frac{\partial^2 \Psi}{\partial^2 x^2} = \frac{2m}{\hbar^2}(E - \infty)\Psi = 0 \qquad (2.3)$$

where Ψ outside the box is zero, and inside the box

$$\Psi = c_1 e^{i\theta} + c_2 e^{-i\theta} \qquad (2.4)$$

and

$$\theta = (2mE)^{\frac{1}{2}}\left(\frac{x}{\hbar}\right) \qquad (2.5)$$

The solution of eq. 2.3 using eq. 2.4 is

$$E = n^2 \frac{\pi^2 \hbar^2}{2mL^2} \text{ , with n = 1,2,3,...} \qquad (2.6)$$

which satisfies the boundary condition of continuity at x = L. The boundary condition allows only quantised energy levels. It can be seen that E is inversely proportional to the square of L; therefore the energy increases quadratically as the size of the box is reduced. This treatment can be applied to the problem of excitonic energy levels in semiconductor clusters.

The Schrödinger equation can be written for the cluster by using the bulk values of m_e^* and m_h^* and by approximating the exciton wave function by a few configurations of $\Psi_i(r_e)\Psi_j(r_h)$ of the particle in a spherical wave functions:

$$\left[\frac{-\hbar^2}{2m_e^*}\nabla_e^2 \frac{\hbar^2}{2m_h^*}\nabla_h^2 + V_0(\xi_e,\xi_h)\right]\Phi(\xi_e,\xi_h) = E\Phi(\xi_e,\xi_h) \tag{2.7}$$

where ξ_e and ξ_h represent the positions of two charges of magnitude e inside the sphere. The energy difference between the lower edge of the conduction band of the cluster and the vacuum level is in fact not infinite[10]. The vacuum level can be thought of as the wall of the sphere, with $V_0 = \infty$. Henglein showed that for aqueous systems $V_0 = 3.8$ eV[11]. In fact, this reduces slightly the cluster size required to see the same effects that would be expected if V_0 would be taken to be infinite. To solve this equation a basis set, the s wave functions for the particle in a sphere, is used,

$$\Psi_n = \frac{C_n}{r}\sin\left(\frac{n\pi}{R}\right) \tag{2.8}$$

where r is the radial position, C_n are normalised constants, R is the radius of the sphere and

$$E_n = \frac{\hbar^2\pi^2 n^2}{2mR^2} \tag{2.9}$$

Then one can find the energy of the lowest excited state by using the wave function $\Phi = \Psi_i(r_e)\Psi_j(r_h)$,

$$E = \frac{\hbar^2\pi^2}{2R^2}\left[\frac{1}{m_e^*}+\frac{1}{m_h^*}\right] - \frac{1.8e^2}{\varepsilon_2 R} + \left\langle\frac{e^2}{R}\sum\alpha_n\right\rangle \tag{2.10}$$

where < > means the average over Ψ_n. The first term is the quantum energy localisation, increasing as R^{-2} for both electron and hole. The second term is the Coulomb attraction, and the third term is the solvation energy loss, where

$$\alpha_n = \frac{(\varepsilon+1)(n+1)}{\varepsilon_2(\varepsilon n + n + 1)} \tag{2.11}$$

and $\varepsilon = \varepsilon_2/\varepsilon_1$. The terms ε_2 and ε_1 are the dielectric coefficients of the sphere and the medium (bath), respectively.

Some typical values of these three terms, taken from literature[9], are shown in Table 2.1:

	ZnO	CdS	GaAs	InSb
Kinetic	0.27	0.27	0.65	>1
Coulomb	-0.24	-0.15	-0.08	-0.06
Solvation	0.06	0.05	0.03	0.02
Total shift	0.09	0.17	0.6	>1

Table 2.1: Energy terms in eV from Eq. 1.8 for R = 3 nm spheres of the indicated materials

From this derivation it is very easy to find the band gap energy of particles with a radius R,

$$E_{(R)} = E_g + \frac{h^2}{8mR^2}\left[\frac{1}{m_e^*} + \frac{1}{m_h^*}\right] - \frac{1.8e^2}{\varepsilon R} + \left\langle \frac{e^2}{R} \sum \alpha_n \right\rangle \tag{2.12}$$

where E_g is the band gap of the bulk material.

It was apparent that this model fits well the experimental data for rather large particles but that the deviation from the measured values increased as the size decreased. For this reason a modified model was developed.

II.4   The hyperbolic band model and the tight-binding theory

In the case of PbS, Wang et al.[12] showed that the model developed above breaks down for particles with a diameter smaller than 10 nm. They claimed that this could be related either to the size-dependent Coulomb interaction or to the breakdown of the effective mass approximation. The dielectric screening decreasing with exciton radius[13] gave rise to the size-dependent Coulomb interaction hypothesis. The dielectric constant of the bulk PbS is large (ε_∞= 17.2) so that the third term of equation (2.12) contributes little to the result of the calculation. For sufficiently small particles, the effective dielectric constant becomes reduced and might influence equation (2.12). Nevertheless Wang et al. thought that for PbS this effect remains small as the exciton formation is due to the transfer of an electron from the S to the Pb atom. As PbS is highly ionic this results in a charge rearrangement, but essentially no new charge separation.

The most important effect is certainly the breakdown of the effective mass approximation. It was reported[12] that judging from the known band structures of PbS the band gap will not move to different points of the Brillouin zone, and that the direct gap will be located at the *L* point. This point has the coordinates *L = (±π/a, ±π/a, ±π/a)*, where *a* is the lattice spacing. For small deviations of *k* (defined in the molecular orbital approach) from the *L* point, as it is the case in rather large particles, equation (2.7) can still be used. However, the effective mass approximation, equivalent to energy surfaces of the parabolic form *ℏ²k²/(2m)*, is accurate only for very small *k*. From the effective mass approximation, *k=π/R* which can be compared to the lattice vector *G =2π/a*. For *k ≥ 0.1G (2R ≤ 10a)*, the calculation of the energies are no longer well approximated by the parabolic form in PbS.

Wang and his co-workers developed a modified model that circumvented this problem. It relies on the approximation that the lowest energy excitation of the PbS lattice leads to a simple electron transfer from S⁻ to Pb⁺, at an energy equal to the bulk band gap. One also assumes that for the calculations of the band gap only two bands are important, those at the *L* point which constitute the highest occupied valence band and the lowest unoccupied conduction band. This model is called the hyperbolic band model, and gives rise to the following equation:

$$\Delta E = \left[E_g^2 + 2\hbar^2 E_g \left(\pi / R \right)^2 / m^* \right]^{1/2} \qquad (2.13)$$

The band gap values obtained following this model are in good agreement with the experimental data for PbS particles down to 2.5 nm.

The experimental data of other semiconductors (like CdS, ZnS, CdSe) could well be fitted by the tight-binding approach, which was also used to model PbS particles with size under 2.5 nm. This semi-empirical theory, considering implicitly the atomic structure, has been intensively used in solid-state physics[14]. It has been adapted for small semiconductor particles of PbS by Wang et al.[12] and for CdS, ZnS[15,16] and CdSe[17] by Lippens and Lannoo. In this method the energy levels and the wave functions are, respectively the eigenvalues and the eigenvectors of the Hamiltonian matrix *H*. The matrix elements of *H* are expressed as a basis set of atomic orbitals (often sp³ orbital) or of linear combinations of them in terms of two-center integrals. As a semi-empirical approach, these integrals are considered free parameters and are obtained by adjustment to the experimental values already known. This means that the

bulk band structure has to be known experimentally. In the case of PbS, a three-parameter tight-binding calculation[12] explains the data quite well. For CdS and ZnS, a thirteen-parameter tight-binding model has been used, allowing good agreement with experimental data down to 2 nm in the case of CdS.

A graphical representation of the above mentioned models is shown on Figure 2.5:
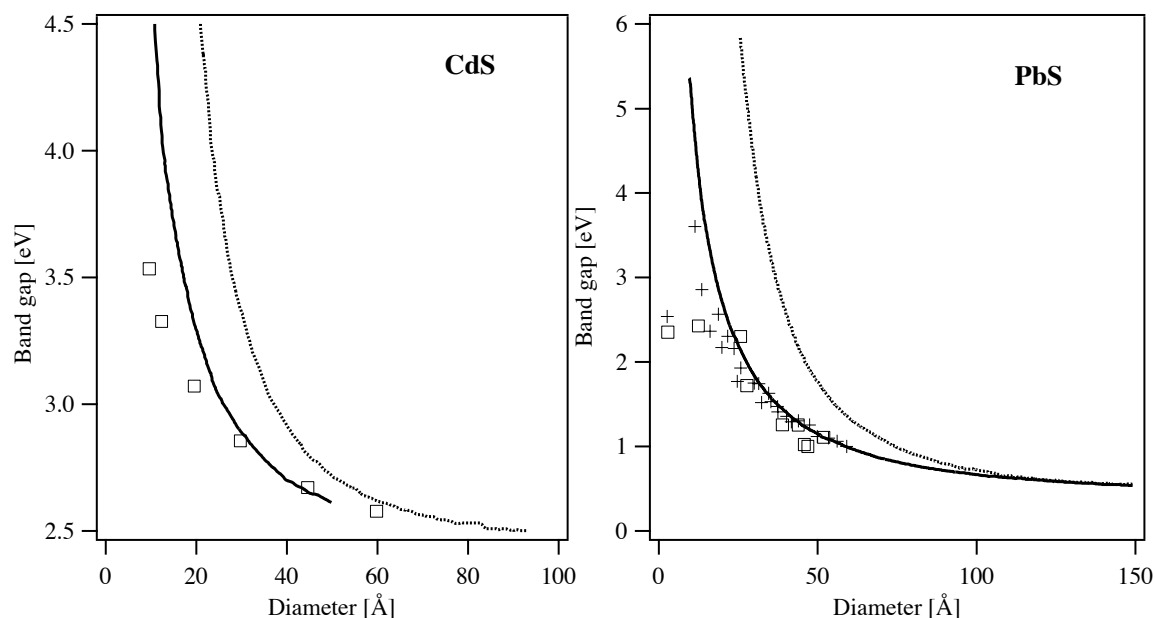
Figure 2.5: Dependence of the optical bandgap of PbS (taken from Ref. 11) and CdS (taken from Ref. 14) on the cluster size. The dashed lines are the calculation based on the effective mass approximation. The squares represent the experimental data. In PbS, the crosses are the results of the cluster tight-binding calculation and the solid line the representation of the hyperbolic band model. In CdS, the solid line is the results of the tight-binding calculation from Lippens et al.[16].

II.5   Bibliography

(1)   Alivisatos, A. P. *J. Phys. Chem.* **1996**, *100*, 13226.

(2)   Miller, R. J. D.; McLendon, G. L.; Nozik, A. J. electron transfer from quantum-confined states. In *Surface electron transfer processes*; Wiley-VCH, Ed. New-York, 1995.

(3)   Ekimov, A. I.; Onushchenko, A. A. *Soviet Physics Semiconductors-Ussr* **1982**, *16*, 775.

(4)   Efros, A. L.; Efros, A. L. *Soviet Physics Semiconductors-Ussr* **1982**, *16*, 772.

(5)   Papavassiliou, G. C. *Journal of Solid State Chemistry* **1981**, *40*, 330.

(6)   Burdett, J. K. *Progress in Solid State Chemistry* **1984**, *15*, 173.

(7)   Brus, L. E. *J. Chem. Phys.* **1983**, *79*, 5566.

(8)   Rossetti, R.; Ellison, J. L.; Gibson, J. M.; Brus, L. E. *J. Chem. Phys.* **1984**, *80*, 4464.

(9)   Brus, L. E. *Journal of Chemical Physics* **1984**, *80*, 4403.

(10)   Weller, H.; Schmidt, H. M.; Koch, U.; Fojtik, A.; Baral, S.; Henglein, A. *Chem. Phys. Lett.* **1986**, *124*, 557.

(11)   Henglein, A. *Berichte Der Bunsen-Gesellschaft-Physical Chemistry Chemical Physics* **1974**, *78*, 1078.

(12)   Wang, Y.; Suna, A.; Mahler, W.; Kasowski, R. *J. Chem. Phys.* **1987**, *87*, 7315.

(13)   Knox, R. S. In *Theory of excitons*; Academic, Ed. New-york, 1963; pp 91.

(14)   Slater, J. C.; Koster, G. F. *Physical Review* **1954**, *94*, 1498.

(15)   Wang, Y.; Herron, N. *Physical Review B* **1990**, *42*, 7253.

(16)   Lippens, P. E.; Lannoo, M. *Physical Review B* **1989**, *39*, 10935.

(17)   Lippens, P. E.; Lannoo, M. *Physical Review B* **1990**, *41*, 6079.

Chapter III

Nanoparticle Sensitised Solid-State Nanocrystalline Solar Cell

This chapter describes the different components of the quantum-dot sensitised solid-state device (QDSSD). The role and the properties of the different constituent components of the device, from the nanocrystalline network, the sensitiser, the hole-conductor, to the counter-electrode will be analysed.

III.1 The nanocrystalline network

The nanocrystalline network is composed of semiconductor colloids which are deposited on a glass coated with a doped transparent conducting oxide (TCO), fluorine doped tin oxide (SnO_2:F). Typically, TiO_2 was used as the nanocrystalline semiconductor; this material has the advantages of being non-toxic, and cheap. These properties make it very attractive for the industrial application as a white pigment in paints, paper, plastics, etc. In the present application the TiO_2 is used as a colloidal dispersion with very small particle size (15-20 nm). A paste based on this powder and containing organic polymers is used to form a film, which is then sintered. This process also creates interconnections between the particles, and thus achieves an electrical contact between them. The final film is mechanically stable, transparent and has a thickness of a few microns. The nanocrystalline semiconductor network, characterized by its high specific surface, has several design functions; it provides the

surface for the sensitiser adsorption, it accepts the electron from the light-excited dye and finally it conducts the injected electrons to the working electrode.

TiO_2 exists in two forms; anatase and rutile. For the building of solar cells, the anatase form, which has a pyramid-like crystal, was used mainly due to its higher stability at room temperature. The rutile form absorbs in the near-UV region leading to the formation of holes, which are strong oxidants able to react with the cell components.

It is known that the hole-conductor, spiro-OMeTAD described in section 3.3, forms an ohmic contact with $SnO_2:F$[1]. An operating cell composed of spiro-OMeTAD as hole-conductor, and of SnO_2 as working electrode would therefore be very inefficient, as an important short-circuit will occur at the SnO_2/spiro-OMeTAD interface. An easy way to prevent this problem is to coat the SnO_2 with a thin blocking TiO_2 layer deposited by spray-pyrolysis. Furthermore, beside its blocking electrical properties this layer also beneficially enhances the mechanical adhesion of the TiO_2 on the conducting glass. After deposition of the hole-conductor solution, the solvents are evaporated to form a solid film. During this process, a stress is exerted on the TiO_2 layer due to the shrinking of the hole-conductor layer.

III.2   The Sensitiser

The sensitiser adsorbed on the surface of the nanocrystalline semiconductor is used to absorb the incoming photon flux. The photochemical, electrochemical, and chemical properties of the sensitiser play an important role to achieve high conversion efficiencies.

Since the solar spectrum is centered on the visible light wavelength (400-800 nm), the sensitiser should be able to absorb optimally the light in this spectral region. In the present work, nanoparticles were used to sensitise the semiconductor. As we saw in Chapter 2, due to the quantum size effect the edge of the absorption spectra of a material can be tuned by varying the size of its particles. For the present application, the particle size distribution does not play an important role as long as the absorption occurs panchromatically (throughout the visible region) and that the injection is possible. The selected synthese for the QD do not achieve a unique particle size but rather a narrow size distribution[2-5].

A long-lived excited state of the sensitiser is necessary to ensure a good injection rate of the photoexcited electron from the sensitiser into the TiO_2. This is normally not a

limiting factor as the injection occurs on the femto- to picosecond time scale, thus faster than the other deactivation pathways. To achieve an efficient electron injection into the TiO_2, the energy level of the sensitiser excited state has to be higher than the energy of the lower edge of the conduction band of the semiconductor. In other words, the oxidation potential of the sensitiser excited state has to be more negative than the oxidation potential of the semiconductor, TiO_2. On the other hand, the energy level of the oxidised sensitiser has to be lower than the energy level of the reduced hole-conductor to ensure an efficient regeneration of the sensitiser. In the case of a QD size distribution, there will be a size limit above which the particles are no longer able to inject electrons into the TiO_2 [6]. Figure 1 shows a simplified injection model by showing relative positions of the valence band and the conduction band in the semiconductor and in the adsorbed QD.
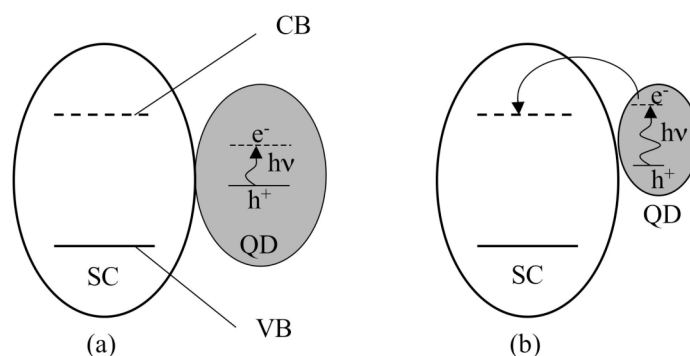
Figure 3.1: Electronic levels in semiconductor (SC) and QD particles. VB (full line): upper edge of the valence band, CB (dashed line): lower limit of the conduction band.
(a) Large PbS particle, (b) Small PbS particle

In case *a*, a large QD is adsorbed on the semiconductor, its band gap is rather small due to weak quantum confinement. The energy of the photogenerated electron in this particle is weaker than the energy of the lower edge of the semiconductor conduction band, and thus the driving force for the injection into the semiconductor is too weak to provoke this process. However, when the QD is smaller, case *b*, the energy of the photogenerated electron is greater than that of the LUMO of the semiconductor, and thus the electron rapidly tunnels to the TiO_2 particle.

To have a good adsorption of the sensitiser on the semiconductor, chemical bonds have to exist between both. In the case of organometallic dyes, the carboxyl groups are anchoring units; forming hydrogen bonds with the oxygen atom present at the TiO_2 surface. In the case of the QD, the situation is not so clear and may depend on the synthetic route. If the QD is grown directly on the surface of the semiconductor,

anchoring is certainly due to bonds appearing between the deposited metal ions and the oxygen atom at the surface. As explained in the following, QD may also be formed in the bulk of the deposition solution before migrating to the surface of the semiconductor. In this case the adsorption of the particle may not be due to metal/oxygen bonds as no metal valences are available for this. In the case of metal sulfides QD, hydrogen bonds can be formed between the sulfur atom and the oxygen at the surface.

III.3   The Hole conductor

The hole conducting material is responsible for the regeneration of the oxidised sensitiser after electron injection into the semiconductor, and for the transport of positive charges to the counter electrode.

On the one hand, to be able to regenerate the oxidised sensitiser, the hole conductor has to have a redox potential higher than that of the oxidised species. The difference between the two potentials should be large enough to ensure a good driving force for the process. On the other hand, as the photovoltage of the dye-sensitised solar cell depends on the redox potential of the hole conductor (as shown in Chapter 1), this potential should be as low as possible to achieve a maximal device voltage under illumination. Moreover the hole conductor should not be able to quench the excited state of the sensitiser; this recombination reaction has to be much slower than the injection of the excited electron into the semiconductor. Finally, the hole conductor should not absorb light in the visible range as this could compete with the sensitiser.

The hole conductor should be deposited on the substrates without damaging the sensitised semiconductor. Using high glass melting temperature materials can also ensure the stability of the deposited films; the hole conductor should be in an amorphous state rather than crystalline to ensure a better pore filling. Indeed hole-conductor crystallisation inside the pores reduces dramatically the pore filling. The hole conductor has to penetrate the pores of the nanocrystalline network. This limits the size of the molecules of the compound, as the pores have sizes in the nanometer scale. The contact with the counter-electrode should have an ohmic behaviour to minimize the internal resistance of the device.

The hole conductor has to be able to transport current without high resistances or diffusion losses. For many organic semiconductors the conductivity is low. The current can be estimated with the following equation:

$$J_n = \mu \cdot k \cdot T \cdot \frac{dn}{dx}$$

(3.1)

where μ is the mobility, n the number of charge carriers, dx the thickness of the hole conductor, k the Boltzmann constant and, T the temperature. One way to enhance this current is doping of the hole-conductor by oxidation, increasing the number of charge carriers.

Spiro-OMeTAD

The hole-conductor molecule spiro-OMeTAD (2,2',7,7'-tretakis(N,N-di-*p*-methoxyphenyl-amine)-9-9'-spirofifluorene), used as a hole conductor, was derived from TPD (N,N'-diphenyl-N,N'-bis(3-methylphenyl)-1,1'-biphenyl-4,4'-diamine)[7,8]. The main advantages of the spiro-OMeTAD over TPD is its high glass transition temperature of 121°C compared to 62°C. This property makes the spiro-OMeTAD a very good candidate for the use in solar cells. Thin spin-coated layers of this molecule showed no crystallisation even after storing for several years[1].
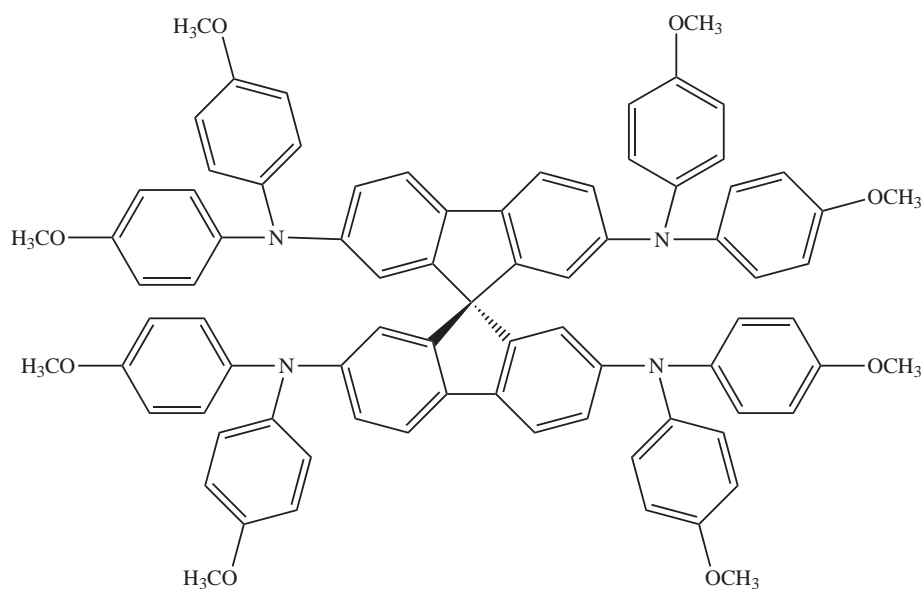
Figure 3.1: Structure of 2,2',7,7'-tretakis(N,N-di-*p*-methoxyphenyl-amine)-9-9'-spirofifluorene (spiro-OMeTAD)

The absorption spectrum of the spiro-OMeTAD in solution is shown in Figure 3.2. The absence of an absorption peak at higher wavelength then 420 nm fulfils the requirement of transparency of the hole-conductor.
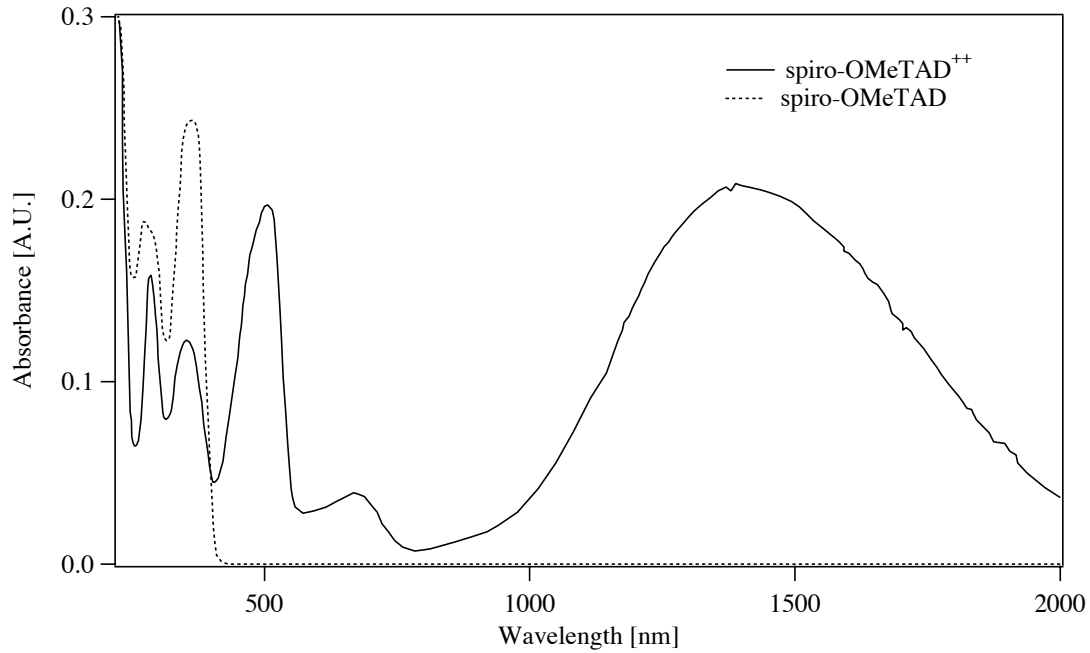
Figure 3.2: Absorption spectra of spiro-OMeTAD and spiro-OMeTAD[++] in solution (80:20 mixture of chlorobenzene and acetonitrile)

The conductivity of pure spiro-OMeTAD is very low, therefore the material cannot be used as is in the solar cells. The conductivity κ is a linear function of the charge carrier mobility μ and the charge carrier density N_h:

$$\kappa = \mu \cdot N_h \cdot e \qquad\qquad (3.2)$$

where $e = 1.602 * 10^{-19}$ C

This means that the doping level of the layer can be enhanced by partial oxidation of the hole conductor i.e. increasing the number of charge carriers increases the conductivity. Chemical oxidation is obtained using Tris(p-bromopheny)ammoniumyl hexachloroantimonate ($[N(p-C_6H_4Br)_3][SbCl_6]$)[1,9]. The absorption spectrum of spiro-OMeTAD[+] has a peak at 511 nm, a shoulder at 700 nm, and a large peak at 1400 nm. The spiro-OMeTAD[2+] should show the same features, as the electronic interaction between the two perpendicular π-systems is small. Weissörtel[10] showed that the diradical cation of the spiro-OMeTAD has in $CHCl_3$ absorption maxima at 511nm (ε = 40100) and 1400nm (ε = 32200) while spiro-OMeTAD[4+] shows an absorption maximum at 865 nm (ε = 118000). The maximum of the spiro-OMeTAD[2+] will be

very useful for the measurements of recombination reactions using nanosecond laser spectroscopy.

III.4   The Counter electrode

The counter electrode material should have a high conductivity and should be able to provide ohmic contact with the hole-conductor; the work function of the material should match the one of the hole-conductor. As it was shown that gold fulfills these requirements [1], this noble metal was used in the present work. It was deposited by evaporation in ultra high vacuum. Furthermore, gold reflects the incoming light from the photoelectrode allowing a second traversal of the sensitised TiO_2 film, thus enhancing the amount of absorbed light.

III.5   Bibliography

(1)   Bach, U. *Ph. D. Thesis* **2000**, *EPFL*.

(2)   Gorer, S.; Hodes, G. *Studies in Surface Science and catalysis* **1996**, *103*, 297.

(3)   Gorer, S.; Hodes, G. *Journal of Physical Chemistry* **1994**, *98*, 5338.

(4)   Weller, H. *Adv. Mater.* **1993**, *5*.

(5)   Vogel, R.; Hoyer, P.; Weller, H. *J. Phys. Chem.* **1994**, *98*, 3183.

(6)   Henglein, A. *Ber. Bunsenges. Phys. Chem.* **1995**, *99*, 903.

(7)   Salbeck, J.; Yu, N.; Bauer, J.; Weissörtel, F.; Bestgen, H. *Synthetic Metals* **1997**, *91*, 209.

(8)   Salbeck, J.; Weissortel, F.; Bauer, J. *Macromolecular Symposia* **1998**, *125*, 121.

(9)   Abkowitz, M.; Pai, D. M. *Phil Mag B* **1986**, *53*.

(10)   Weissörtel, F. Amorphe niedermolekulare Ladungstransportmaterialien für nanokristalline Solarzellen. Diplomarbeit, Universität Regensburg, 1996.

Chapter IV

The Device

IV.1   Materials

Thin compact TiO_2 layers were prepared by spray pyrolysis using as precursor di-iso-propoxytitanbis(acetylacetonate) (TAA[®], purchased from Aldrich). The TAA solution stored under argon was diluted with ethanol to 0.02 M prior to use, as the solution changed colour from yellow to orange in air.

Screen-printable TiO_2 pastes for the preparation of the nanocrystalline layers were prepared by Pascal Comte and Raphaël Charvet following the procedure described by Barbé et al[1]. In the framework of these studies different pastes were used. Their porosity, particle size, and surface area are summarised in Table 4.1.

Name	Porosity [%]	Particle size [nm]	Specific surface [m^2/g]
JDD1x-S7	69	15	104
PC100x-S2	65	15	105
PC147x	65	15	97
RC14x	65	18.5	84

Table 4.1: Characteristics for different screen-printable pastes, characterised by P. Comte using BET technique.

Doctor-blading pastes were prepared by diluting screen-printable pastes with ethanol making them more fluid.

The chemicals used for the preparation of the nanoparticles were purchased from different suppliers, unless otherwise stated, puriss p.a. grade was used. For the dip-coating synthesis method, sodium sulphate hydrate was purchased from Fluka, $Pb(NO_3)_2$ and $Cd(NO_3)_2$ from Merck. For chemical bath deposition, Na_2SO_3 anhydrous from Acros, selenium powder from Fluka, $Pb(CH_3COO)_2*3H_2O$ from Acros, and $CdSO_4$ from Fluka were used.

Spin-coating solutions were prepared using dry solvents, Chlorobenzene (Fluka) and Acetonitrile (Merck) stored under argon prior to use.

2,2',7,7'-tetrakis(N,N-di-p-methoxyphenyl-amine)-9,9'-spirobifluorene (spiro-OMeTAD) was supplied by Covion organic Semiconductor GmbH.

The spin-coating stock solution was prepared under inert atmosphere using additives like $Li[(CF_3SO_2)_2N]$ (purchased from Fluka).

IV.2   Device preparation

To study the current voltage characteristics a device (as shown in Figure 4.1) with four small diodes each possessing a surface area of 0.16 cm^2 was employed. Having four active cells on a single module allows having a measure of its homogeneity.
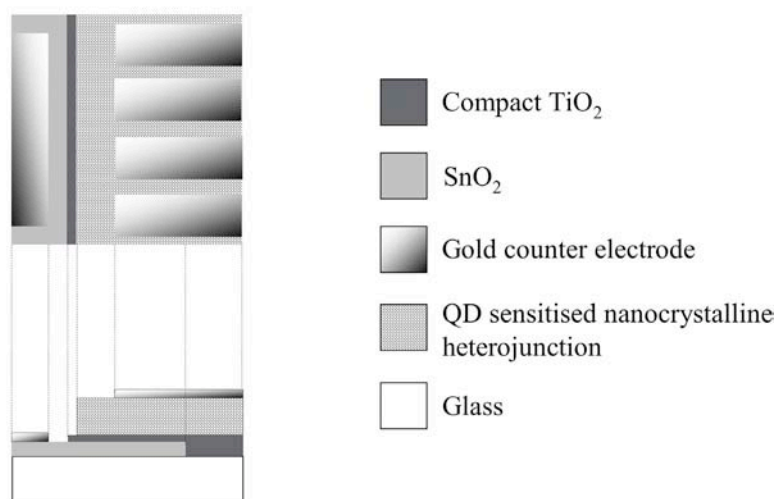
Figure 4.1: Scheme of the device

IV.2.1   Conducting glass substrates

From a variety of conducting glasses (TCO), Asahi glass was chosen for its low resistance (10 $\Omega/\square$) and its thinness (1 mm). This glass is based on fluorine doped SnO_2 as a conducting layer, which has a better thermal stability compared to indium doped tin oxide (ITO). The structuring of the TCO was done using a chemical etching method. Zinc granulates were spread on the glass (20 mg/cm^2) and reacted with 4 N HCl (1 ml/cm^2). Scotch© tape was used to mask the TCO area needed for the back contact. The fast reaction between HCl and Zn leads to the removal of the SnO_2. After two treatments of 3 min reaction time the SnO_2 is completely removed.

The structured glass is then cleaned by ultra-sonification in various solvents for 10 min in each solvent as shown below:

- 1x acetone
- 1x ethanol
- 1x Hellmanex® (2% in H_2O)
- rinse with water several times
- 1x H_2O
- 1x ethanol

The cleaned substrates were stored in ethanol. Prior to use the substrates were cleaned by an UV/Ozone treatment (UVO-Cleaner®, Model N°. 256-220, Jelight Company Inc.) for 15 min.

IV.2.2   Compact TiO$_2$ layer

The compact films of TiO$_2$ were deposited by spray pyrolysis of TAA® precursor. The procedure was described by Kay[2] and Kavan and co-workers[3].

The sample was heated on a massive titanium plate(10x280x200 mm). Temperature was set to 450°C and controlled by a NiCr/Ni thermopile. The precursor solution was sprayed from a distance of around 20 cm using a chromatographic atomiser. The sample surface was partially masked with 1 mm thin float glass in order to avoid complete coverage of the glass by the compact TiO$_2$ layer. Layer thicknesses of about 120 nm were built up with 20 spray processes[4]. To allow complete evaporation of the solvent, the spray process was performed with an interval of 10 sec. The overall consumption of precursor solution was 0.1 ml/cm^2[5]. The substrates were deposited on the massive plate 10 min prior to spraying for thermal equilibration and left on the

plate for 10 min after deposition of the precursor for complete transformation to TiO_2 and for complete burning of residual organics.

IV.2.3   Nanocrystalline TiO$_2$ layer

Two different techniques were used to deposit the nanocrystalline TiO_2 layer.

"Screen-printing"

A manual screen-printing set-up was used to deposit a 20 mm broad strip of colloidal TiO_2 on the substrates. A vacuum system was used to stick the substrates on the main plate of the set-up. By varying the mesh size one controls the thickness of the deposited layer. The screen was first filled up with paste then put on the substrate to deposit the paste. This procedure was repeated twice to improve the homogeneity of the layer. After deposition, the layers were stored in the dust-free container for 15 min.

"Doctor-blading"

The substrates were fixed on a glass support using Scotch$^{®}$ tape which determines layer thickness at the same time. The paste was deposited onto the substrates and was then spread out using a glass pipette. The thickness of the deposited layer is determined by the Scotch$^{®}$ tape. After deposition the layers were allowed to set in a dust-free container for 30 min.

For both techniques, the substrates were sintered using the following temperature profile:
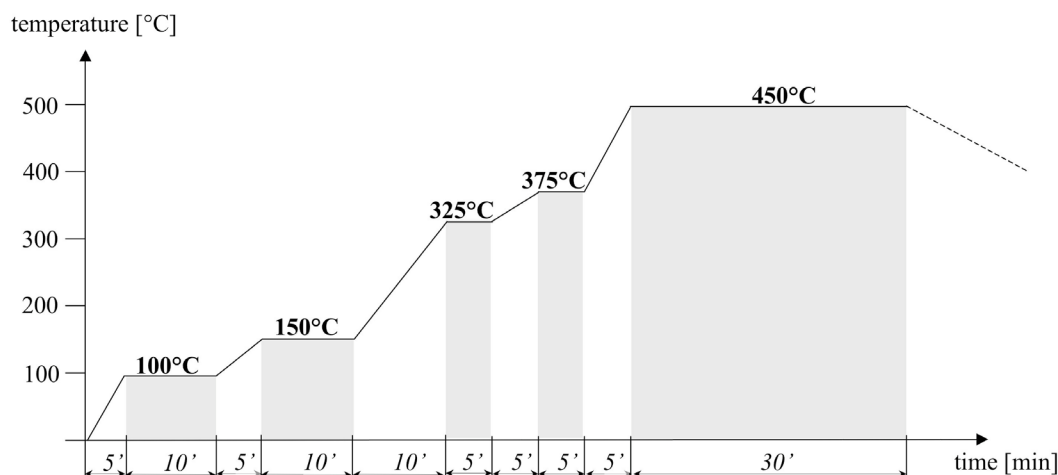
Figure 4.2: Temperature program for the substrate sintering.

The stages at 100°C and 150°C are done under normal atmosphere in order to evaporate all the solvents. The subsequent steps were carried out under an oxygen flux. It is very important to burn out all the organic compounds present in the paste without forming carbon inclusions in the pores. The chosen sintering program allows first the combustion of the additives and then the sintering. Pure oxygen was used to ensure sufficient combustion.

An increased surface area and the formation of a very pure TiO_2 could be obtained by a $TiCl_4$ post-treatment on the deposited nanocrystalline TiO_2. This treatment was shown to increase the injection of electrons into the TiO_2 and thus the current that is delivered by the solar cell. The precipitation of Ti complexes at the joining points of two particles increases the interparticle connection and the electron transit from one particle to another. Nevertheless, the treatment causes a decrease of the pore size and thus of the pore filling. $50\mu l/cm^2$ of a 0.02 M $TiCl_4$ solution in water were applied on the nanocrystalline TiO_2 layer for 12 hours at room temperature. The contact areas were protected with a water-resistant adhesive tape. After the treatment the substrates were washed with highly purified water, and sintered a second time for 15 min at 450°C just before the sensitiser was applied.

IV.2.4   Quantum dot sensitisation

Several types of nanoparticles were used during the present work, which can be classified into two main groups, the metal sulfides (PbS, CdS, ZnS, Bi_2S_3) and the metal selenides (PbSe, CdSe). All the QD were synthesised in-situ on the surface of the semiconductors (TiO_2, ZrO_2, Al_2O_3). The main reason for this is that the in-situ

synthesis on the TiO$_2$ is expected to yield a better contact between the two materials. Furthermore, the nanoparticles synthesised in solution have often to be stabilised with molecules like TOPO (trioctylphosphine oxide), which are then extremely difficult to remove.

IV.2.4.1 Metal sulphides

Two different methods were used for the synthesis of the metal sulphides. For the sake of simplification the "dip-coating " and "chemical bath deposition" terms will be used in the following descriptions.

"Dip-coating" [6]

TiO$_2$ substrates are dipped for 1 min into an aqueous saturated nitrate solution of a metal ion (Pb^{2+}, Cd^{2+}, Zn^{2+}, BiO$^+$). After rinsing thoroughly with pure water the substrate is dipped for 10 seconds into an aqueous 0.2 M Na$_2$S solution and rinsed again. This procedure represents "one cycle". These cycles are repeated several times, it was shown that the small particles formed during the first coating act as nucleation centers for the material which is brought about in the consecutive coating processes[7].

"Chemical bath deposition"

The idea of this method is to mix all the reagents together at the beginning of the synthesis. It was used for preparation of PbS sensitised TiO$_2$. In this procedure a large part of the lead ions are complexed to a complexing agent (triethanolamine) and only slowly released as the free lead ions react with the sulphur ions present in the solution. A more detailed explanation is given in the following when treating the deposition mechanism of the metal selenides. 50 ml of the starting solution consisted of:

- 1.25 ml of 1 M lead acetate
- 5 ml of 1 M sodium hydroxide
- 3 ml of 1 M thiourea
- 1 ml of 1 M triethanolamine
- rest was water

This composition found in the literature[8] was varied during the study to analyse the effect on the deposition of the different components. The substrates are immersed in this solution for a time varying from 10 min to several hours. As the synthesis is highly temperature dependent, the reaction temperature was set to 20°C and controlled by a thermostatic bath. After deposition the substrates were rinsed either with HCl 1 M or with pure water, and heated up to normally 150°C for 30 min under an argon atmosphere.

IV.2.4.2 Metal selenides

Chemical bath deposition[9-12] was used to synthesise the metal selenides (PbSe and CdSe). In this method three different complexing agents were used: trisodium citrate (TSC), potassium nitrilotriacetate (K_3NTA), and potassium hydroxide (KOH). Nitrilotriacetic acid was neutralised using three equivalents of KOH to obtain the non-commercially available K_3NTA.

The preparation of PbSe and CdSe is very similar; lead acetate is used for the PbSe and cadmium sulfate is used for the CdSe. For the deposition of PbSe using TSC as complexing agent, the following aqueous stock solutions were prepared: 0.5 M lead acetate, 1 M TSC and 0.2 M sodium selenosulfate (Na_2SeSO_3). The last solution was prepared by stirring 0.2 M Se with 0.5 M Na_2SO_3 overnight at 85°C. The lead acetate and the TSC solutions were mixed together and KOH was added to adjust the pH to 10. Then the Na_2SeSO_3 solution was added. The final concentration was 60 mM Pb^{2+}, 50 mM Na_2SeSO_3, and 160-320 mM TSC. The higher the concentration of complexing agent, the slower was the precipitation of PbSe. This effect was studied in more detail.

For the deposition using NTA as complexing agent the same stock solutions were used except for the TSC which was replaced by a 0.7 M K_3NTA solution. The deposition solution was prepared in the same way as for TSC and the final concentration was 60 mM Pb^{2+}, 50 mM Na_2SeSO_3, and 60 mM 0.7 M K_3NTA.

For the deposition using KOH as complexing agent 1 M stock solution was used. The deposition solution was obtained by adding first the Pb^{2+} solution to the KOH solution and then adding the Na_2SeSO_3. The final concentration was 60 mM Pb^{2+}, 50 mM Na_2SeSO_3, and 0.6-1.2 M KOH.

IV.2.4.2.1 Deposition mechanisms.

The ratio of complex to metal ions plays an important role by determining the deposition mechanism. There exists a critical ratio (R_c) around which the crystal size is highly dependent on this ratio, shifting the transition from one mechanism to the other. Apart from R_c, the crystal size varies only weakly with the changing ratio.

Two main mechanisms have to be considered during the CBD: ion-by-ion deposition onto the substrate with no precipitation in the solution, and the bulk precipitation with diffusion of the bulk formed colloids to the substrate. The latter mechanism is due to the presence of metal hydroxide M(OH)$_2$ in the solution. Nucleation can occur on this solid hydroxide phase more easily than if there were no nuclei present in the solution. Considering the formation of CdSe the following equations can be written [10]:

- *Formation of the selenide;* $2SeSO_3^{2-} + H_2O \rightarrow HSe^- + SeS_2O_6^{2-} + OH^-$

  This step is rate-determining in the overall reaction, it is activation-controlled

- *Cd-complex formation;* $Cd^{2+} \overset{NTA^{3-}}{\leftrightarrow} Cd(NTA)^- \overset{NTA^{3-}}{\leftrightarrow} Cd(NTA)_2^{4-}$

  The amount of free Cd^{2+} can be calculated knowing the initial concentration of Cd^{2+} and the stability constants of Cd(NTA)$^-$ and Cd(NTA)$_2{}^{4-}$.

These two reactions are common to the two types of mechanisms.

Ion-by-ion mechanism:

- *Nucleation of CdSe;* $Cd^{2+} + HSe^- + OH^- \leftrightarrow CdSe(s) + H_2O$
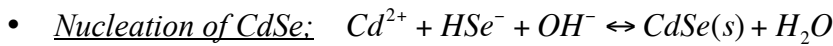
  The precipitation occurs if the product of the concentrations of the species exceeds the solubility product, K_{sp} (10^{-35}).

- *Crystal growth;* $(CdSe)_m + Cd^{2+} + HSe^- + OH^- \leftrightarrow (CdSe)_{m+1} + H_2O$

- *Aggregation or coalescence;* $(CdSe)_m + (CdSe)_n \leftrightarrow (CdSe)_{m+n}$
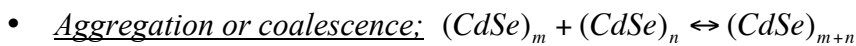
  The coalescence is the combination of two clusters to form one single crystal, and aggregation means that two or more separate but contacting crystals are formed.

Bulk precipitation:

- *Formation of Cd(OH)$_2$;* $Cd^{2+} + 2 \cdot OH^- \leftrightarrow Cd(OH)_2(s)$

- *Conversion to CdSe;* $Cd(OH)_2(s) + HSe^- \rightarrow CdSe + OH^- + H_2O$
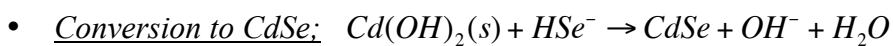
  The hydroxide nucleus is eventually converted to CdSe.

- *Nucleation of CdSe;*

  $$Cd(OH)_2(s) + Cd^{2+} + HSe^- + OH^- \leftrightarrow Cd(OH)_2 \cdot CdSe + H_2O$$
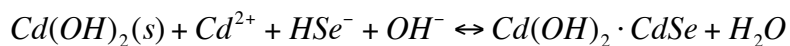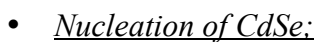
CdSe can also nucleate at the surface of the hydroxide, although in the long term, all the $Cd(OH)_2$ will be converted to the more stable CdSe. But as $Cd(OH)_2$ is transformed to CdSe more hydroxide will precipitate as the equilibrium is displaced. On the other hand, since the concentration of Cd^{2+} is decreasing with time and the concentration of NTA^{3-} is constant, $Cd(OH)_2$ will have a decreasing tendency to precipitate

IV.2.4.2.2 Reaction parameters[11]

Solution composition; As discussed before, the reaction is not very sensitive to the solution composition. Only when the complexing agent to metal ratio is near the critical ratio is the sensitivity increased. Below this ratio the solution is designated as low complex (LC) while, when above, it is called high complex (HC).

Deposition temperature; The crystal size is strongly dependent on the deposition temperature. A lower temperature results in smaller crystals. This parameter is one of the most important to control. However, the lower deposition temperature also leads to a slower deposition rate.

Illumination during deposition [12]; Illumination during deposition has a marked effect on the absorption characteristics of the produced particles. This can be explained by photo-electrochemical reactions occurring on the growing crystallites. Therefore, the deposition solution should be kept in the dark during deposition.

Nature of the substrate; One should ensure that the synthesised particles are able to adsorb at the surface of the substrate.

IV.2.5   Surface co-modification

Surface co-modification was achieved by immersing the sensitised TiO_2 layers into a ethanol solution containing the molecules to deposit at a concentration of 0.5 mM. The layers stayed two hours in the solution before drying in air prior to spin-coating of the hole-conductor. The concentration of the deposition solution was shown to have only a minor influence on the resulting device.

IV.2.6   *Spiro*-OMeTAD deposition

A spin-coating technique is used to apply the hole-conductor. The solution is deposited on the substrates and spun to form a flat layer at the surface of the substrate. The spin-coating solution is prepared as follows; spiro-OMeTAD is dissolved in dry

chlorobenzene to form a 0.25 M solution. Besides this a dry acetonitrile solution 4.3 mM in $N(p\text{-}C_6H_4Br)_3SbCl_6$ and 0.15 M in $Li(CF_3SO_2)_2$ is prepared. The two solutions are mixed together obtaining a final concentration of 0.23 M in spiro-OMeTAD, 13.6 mM in $Li(CF_3SO_2)_2$ and 0.4 mM in $N(p\text{-}C_6H_4Br)_3SbCl_6$.

The sample is placed in a chamber under argon flux for 1 min. 150 µl of the spin-coating solution was applied onto the substrate; the solution is allowed to set 1 min on top for good penetration into the pores. The substrate is spun up to a speed of 1000 rpm for 30 s with an acceleration of 200 rpm/s. The samples were then dried for 30 min in argon and 30 min under vacuum (0.1 mbar) before deposition of the counter electrode.

The thickness of the spin-coated hole-conductor layer on top of the sensitised heterojounction is about 400 nm as shown in Figure 4.3.
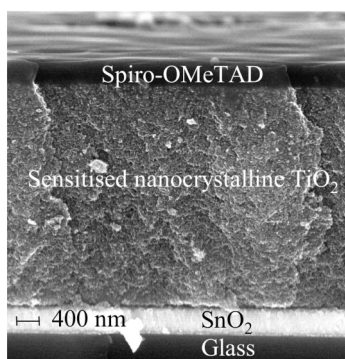
Figure 4.3: Scanning electron micrograph showing a cross section of a sample after spin-coating.

The spiro-OMeTAD film on top of the nanocrystaline semiconductor serves as a spacer to avoid the direct contact between sensitised heterojounction and the counter electrode. Previous work showed that diminishing the concentration of the hole-conductor solution by 50% did not increase the short circuit risk[5].

IV.2.7   Counter electrode deposition

A gold film of 30 nm was used as contact material. It was evaporated on the sample using an Edwards Auto 500 evaporator at a pressure of $7*10^{-6}$ mbar. The deposition rate was around 0.1 nm/s for the first 3 nm and then 0.3 nm/s until 2 nm before the desired thickness was obtained and then again 0.1 nm/s until the end. The typical thickness allowed having a strong enough layer which doesn't tend to peel off as thicker layers.

IV.3   Bibliography

(1)   Barbé, C.; Arendse, F.; Comte, P. *Journal of American Ceramics Society* **1997**, *80*, 31557.

(2)   Kay, A., EPFL, 1994.

(3)   Kavan, L.; Grätzel, M. *Electrochimica acta* **1995**, *40*, 643.

(4)   Bach, U. *Ph. D. Thesis* **2000**, *EPFL*.

(5)   Krueger, J. Interface engineering in solid-state dye-sensitized solar cells, EPFL, 2003.

(6)   Vogel, R.; Hoyer, P.; Weller, H. *J. Phys. Chem.* **1994**, *98*, 3183.

(7)   Vogel, R.; Pohl, K.; Weller, H. *Chem. Phys. Lett.* **1990**, *174*, 241.

(8)   Suarez, R.; Nair, P. K. *Journal of solid state chemistry* **1996**, *123*, 296.

(9)   Gorer, S.; Albuyaron, A.; Hodes, G. *Journal of Physical Chemistry* **1995**, *99*, 16442.

(10)   Gorer, S.; Hodes, G. *Journal of Physical Chemistry* **1994**, *98*, 5338.

(11)   Gorer, S.; Hodes, G. *Studies in Surface Science and catalysis* **1996**, *103*, 297.

(12)   Hodes, G. *Israel Journal of Chemistry* **1993**, *33*, 95.

Chapter V

Experimental Methods

In this chapter, the experimental techniques used are exposed. Absorbance and fluorescence spectroscopy as well as Fourier transform infrared spectroscopy were used to characterise the system. The performance of the solid-state device was measured using photovoltaic techniques. The reaction dynamics were studied using time resolved spectroscopy.

V.1   Absorption and fluorescence spectroscopy

Absorption spectroscopy was used to characterize the optical density of the deposited nanoparticles. From the absorption spectrum it was possible to estimate the particle size of the Q.D.. Absorption spectra were measured on a Cary 5 UV/Vis/NIR spectrophotometer. The solid samples were attached to a metal plate containing holes with double face adhesive tape. They were illuminated from the glass side.

The fluorescence spectroscopy was used to monitor a possible electron injection from the nanoparticle into the TiO_2, by comparing the obtained spectra with those of other semiconductors, such as ZrO_2 and Al_2O_3. The measurements were done using a SPEX Fluorolog 112 fluorimeter, which was equipped with a double monochromator for the emission spectrum. A Hamamatsu R2658 photomultiplier was used for the detection. The samples were excited with a Coherent Innova Kr laser at 468 nm or 520 nm.

V.2   FTIR spectroscopy

Infrared spectroscopy is one of the most powerful tools available to the chemists for identifying organic and inorganic compounds. Indeed most molecular species absorb infrared radiation. It is based on the fact that the absorbed radiation stimulates molecular vibration. These vibrations are characteristic for each organic functionality, such as methyl or aldehyde groups for example. Each molecular species has a unique infrared absorption spectrum. Thus, in an ideal case, an exact match between the spectrum of a compound of known structure and that of an analyte unambiguously identifies the latter. For quantitative analyses infrared spectroscopy is less efficient than UV/Vis spectroscopy because the narrow peaks that characterize infrared spectroscopy usually lead to deviations from Beer's law. Fourier-transform infrared spectroscopy (FTIR), offering the advantages of unusually high sensitivity, resolution and speed of data acquisition, became the standard technique for chemical characterisation. Fourier-transform instruments are detecting and measuring all the wavelengths simultaneously. In order to separate wavelengths, it is necessary to modulate the source signal in such a way that it can be decoded by a Fourier transformation, a mathematical operation.

There exist two major techniques able to enhance the sensitivity of the FTIR measurements; attenuated total reflectance (ATR), and photoacoustic spectroscopy (PAS). The non-destructive ATR technique is based on the reflectivity of a diamond crystal, which is influenced by the nature of the measured material. On the other hand PAS is based on the heat transfer. The radiation absorbed by the sample is transformed into heat, which diffuses to the environment and results in local pressure variations which are detected by a very sensitive microphone.

The FTIR spectra were measured using a Digilab FTS-7000 step-scan spectrometer, equipped with a DTGS detector. The total attenuated reflectance accessory is based on a diamond element (Specac, Orpington). The samples were contacted with the diamond using a sapphire anvil assembly mounted overhead on a unique swing bridge. A reproducible load of 3 kbar was applied on the sample. The PAS measurements were carried out using a MTEC 300 photoacoustic cell (Mtec).

V.3   Photovoltaic characterisation

The two widely used techniques for photovoltaic characterisations are, current-voltage measurements under simulated sunlight and monochromatic light generated current measurements; IPCE.

V.3.1   Current-voltage measurements[1-3]

The dye-sensitised solar cell device can be represented by an equivalent electric scheme shown in Figure 5.1.
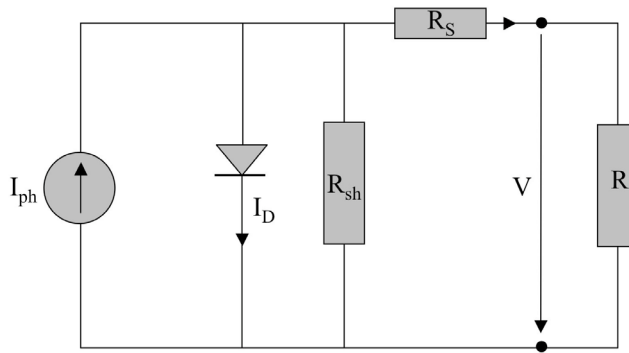
Figure 5.1: Equivalent electric scheme of the dye-sensitised cell.

Where I_{ph} is the photo current, I_D the diode current, R_S the series resistance (describes the resistances of the materials) and R_{sh} the shunt resistance.

The TiO_2/sensitiser interface is modelled as a Shottky diode. The equation of such a diode is:

$$I_D = I_S \left[\exp\left(\frac{V + I \cdot R_S}{\eta \cdot V_{th}} \right) - 1 \right] \qquad (5.1)$$

where I_S is the saturation current, η the ideality factor (typically varies from 1 to 2.4), and V_{th} the thermal voltage:

$$V_{th} = \frac{k_B \cdot T}{q} \qquad (5.2)$$

The equation for the equivalent electric scheme in Figure 5.1 is:

$$I = I_{ph} - I_s \cdot \left[\exp\left(\frac{V + I \cdot R_S}{\eta \cdot V_{th}} \right) - 1 \right] - \frac{V + I \cdot R_S}{R_{sh}} \qquad (5.3)$$

The shunt resistance is normally much larger than the series resistance. For this reason one can simplify Equation 5.3:

$$I = I_{ph} - I_S \cdot \left[\exp\left(\frac{V + I \cdot R_S}{\eta \cdot V_{th}} \right) - 1 \right]$$ (5.4)

During the current-voltage measurements the following parameter will be determined:

Short-circuit current (I_{sc})

The current equals the short-circuit current when the applied bias potential is zero:

$$I_{sc} = I_{ph} - I_S \left[\exp\left(\frac{I_{sc} \cdot R_S}{\eta \cdot V_{th}} \right) - 1 \right]$$ (5.5)

Open-circuit potential (V_{OC})

When no current is flowing through the cell the potential equals the open-circuit potential, using equation 5.4 one can find:

$$V_{OC} = \eta \cdot V_{th} \cdot \ln\left(\frac{I_{ph}}{I_S} + 1 \right)$$ (5.6)

Maximal power output (P_{max})

The power delivered from a solar cell at a certain potential equals the product of the current at this potential times the potential:

$$P(V) = I(V) \cdot V$$ (5.7)

To obtain a graphic representation of the power one has to vary the potential between V_{OC} and 0:
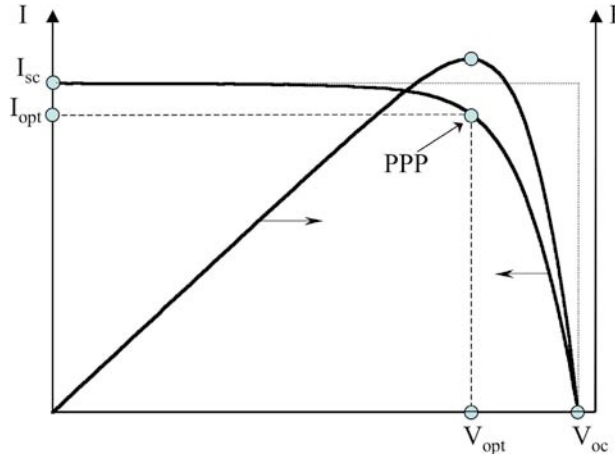
Figure 5.2: Representation of the I/V and the power curves. PPP is the point of peak power.

The point where the power is maximum (P_{max}) corresponds to the so-called peak power point (PPP) for the I/V curve. These are the optimal current and potential conditions (I_{opt}, V_{opt}) for the operating cell.

Fill-factor (*FF*)

The fill-factor quantifies the quality of the solar cell, it is the ratio between the areas of the two rectangles shown in figure 5.2:

$$FF = \frac{V_{opt} \cdot I_{opt}}{V_{oc} \cdot I_{sc}} \tag{5.8}$$

For a good cell the fill-factor lies between 0.7 and 0.85. These values are influenced by the values of the series and the shunt resistances. To obtain high fill-factor values the shunt resistance has to be as small as possible and the series resistance as high as possible.

Efficiency (η)

The overall conversion efficiency η is given by the following relation:

$$\eta = \frac{V_{opt} \cdot I_{opt}}{P_{in}} = \frac{V_{oc} \cdot I_{sc} \cdot FF}{P_{in}} \tag{5.9}$$

It expresses the ratio of produced power to the incoming power (P_{in}).

The experimental conditions have been fixed worldwide, in order to compare results coming from different research centers. An approximated power density value of 1000 W/m^2 has been set for the incident solar radiation, the temperature of the cell should be 25°C and the spectral power distribution of the incoming light should correspond to AM 1.5. The airmass (AM) is the ratio of the path length of incoming

sunlight through the atmosphere when the Sun is at an angle ϑ to the zenith, to the path length when the Sun is at the zenith:
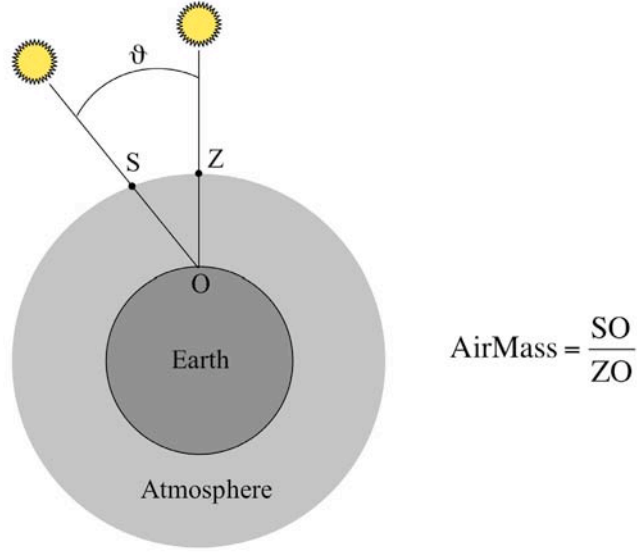
Figure 5.3: Representation of the AirMass concept.

AM1.5 corresponds to the spectral power distribution of light coming in with an angle ϑ of 48° to the zenith.

V.3.2   IPCE measurements[2,4]

The sensitivity of a solar cell varies with the wavelength of the incoming light. The incident-photon-to-electron conversion efficiency (IPCE) measures under monochromatic light the ratio of the number of electrons generated by the solar cell to the number of incident photons on the active surface:

$$IPCE(\lambda) = \frac{n_{electrons}(\lambda)}{n_{photons}(\lambda)} = \frac{I(\lambda)/e}{P_{in}(\lambda)/h \cdot \nu} = \frac{I(\lambda)}{\lambda \cdot P_{in}(\lambda)} \cdot \frac{hc}{\nu} \qquad (5.10)$$

where $I(\lambda)$ is the current given by the cell at wavelength λ and $P_{in}(\lambda)$ the incoming power at wavelength λ.

The spectral sensitivity $S(\lambda)$ is the product of the IPCE(λ) and the wavelength λ. If one knows the spectral irradiation intensity $E(\lambda)$ one can find the short-circuit current I_{sc} using:

$$I_{sc} = \int S(\lambda) \cdot E(\lambda) \cdot d\lambda \qquad (5.11)$$

This method is useful for an indirect determination of the short-circuit current of the solar cell.

V.3.3   Experimental Setup [3]

Current-voltage characteristics were measured using a computer controlled potentiostat (Keithley 2400 Source Meter) and a sulphur lamp (Solar 1000, Fusionlighting Inc/USA). The light intensity was varied using meshes in front of the sulphur lamp. The set up allowed measurements at 1%, 10%, 50% and 100% sunlight intensity and was calibrated using a Silicon photodiode.

The IPCE measurements were done on a set-up illuminated with a 300 W xenon lamp. The light wavelength was selected by a monochromator (Spex Gemini 180, Jobin Yvon Instruments SA). The beam was then split and directed on a calibrated Si cell and on the test cell. The Si cell was used as reference to measure the relative spectral response of the test cell as a function of the wavelength.

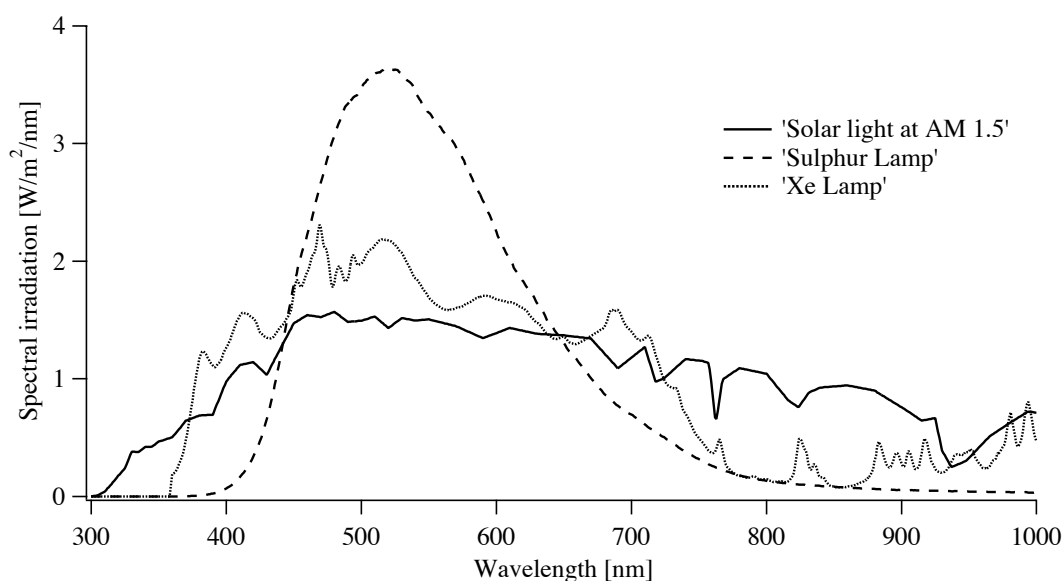Figure 5.4 shows the spectra of different light sources:

Figure 5.4: Spectral irradiance distribution of different lightsources; solar light at AM 1.5, sulphur lamp, and xenon lamp.

V.4   Laser spectroscopy

V.4.1   Nanosecond laser spectroscopy

The time resolved nanosecond laser spectroscopy was used to monitor the recombination reactions at the TiO_2/hole-conductor interface. The observed reaction

is the recombination of the injected electron in the TiO_2 with the hole in the oxidised hole-conductor:

$$e^-\left(TiO_2\right) + h^+\left(spiro - OMeTAD\right) \rightarrow \Delta \tag{5.12}$$

The samples were usually excited at 450 nm and an observation wavelength of 518 nm was chosen for the following reason; as shown in Figure 3.2 the oxidised state of the spiro-OMeTAD has a characteristic absorption peak at 518 nm. The optical density at this wavelength was monitored to observe the recombination reaction. Transient absorption difference spectra were also recorded by varying the observation wavelength from 480 nm to 700 nm.

The flash photolysis experiments were carried out using a Nd:YAG laser (Continuum Powerlite 7030) as excitation source, providing 6 ns pulses at a repetition rate of 30 Hz. The triplet of the laser fundamental (355 nm) was sent into a broadband optical parametric oscillator (OPO). The energy of the laser beam incident on the sample was measured using a thermopile. The beam was sent through a converging lens so that its size was roughly 1 cm^2 on the sample. An angle of 30° was kept between the surface of the sample and the laser beam to avoid the laser beam entering into the detector and to increase the illuminated area. The probe light from a Xe lamp (Osram, 450 W) was sent through a cut-off filter and a monochromator before illuminating the sample. After the sample, the light was sent through a cut-off filter and a grating monochromator. The light intensity was measured using a fast photomultiplier, and the data were averaged over 2000 laser shots by a 1 GHz band-pass digital oscilloscope (Tektronix DSA 602A).
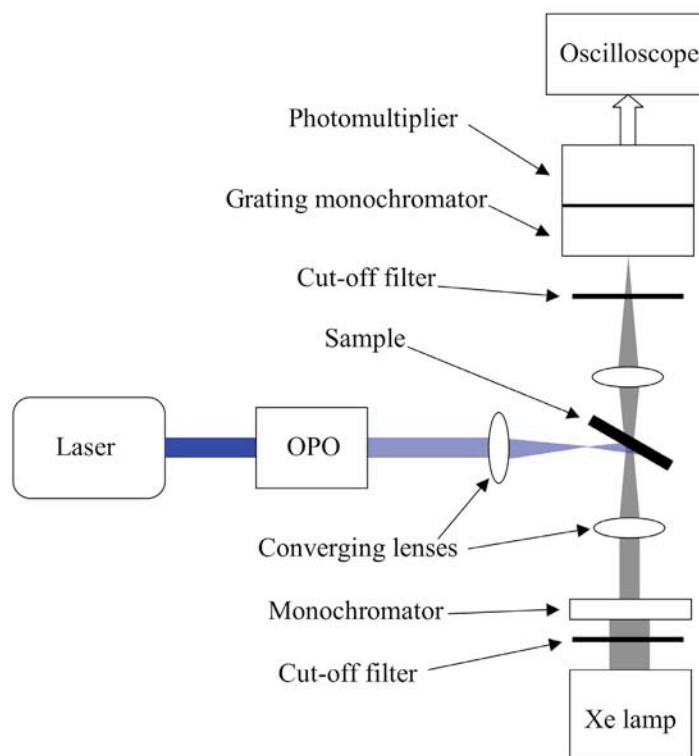
Figure 5.5: Nanosecond laser spectroscopy set-up

V.4.2   Femtosecond laser spectroscopy

To observe reactions occurring on the femto to picosecond time scale a pump-probe technique using a femtosecond laser source was used. It was possible to monitor the trapping of electrons at the surface of the PbS, the injection of these trapped electrons into the TiO_2, and the recombination of the exciton in the PbS. The samples were excited at 600 nm with the femtosecond laser. At this wavelength the PbS nanoparticles still absorb a large amount of light. A probe pulse centered on 778 nm was used to resolve the different reactions occurring inside the PbS. Another probe wavelength of 1400 nm was chosen, to monitor the electrons in the TiO_2 and the oxidised hole conductor. The absorption spectrum of the spiro-OMeTAD is shown in Figure 3.2.

A detailed explaination of the experimental set-up was given by Serge Pelet[5]. Briefly, the fundamental of the femtosecond laser source (CPA 2001 from Clark-MXR) was used to probe the sample at 778 nm, while the pump beam at 600 nm and the probe beam at 1400 nm were generated by two noncollinear optical parametric amplifiers (NOPA). After interaction with the pump pulse in a moving sample, the probe beam intensity was measured by a diode. The diode signal was analysed by a lock-in

amplifier tuned at the frequency of a chopper placed on the pump pathway. A schematic representation of the set-up is given in Figure 5.6
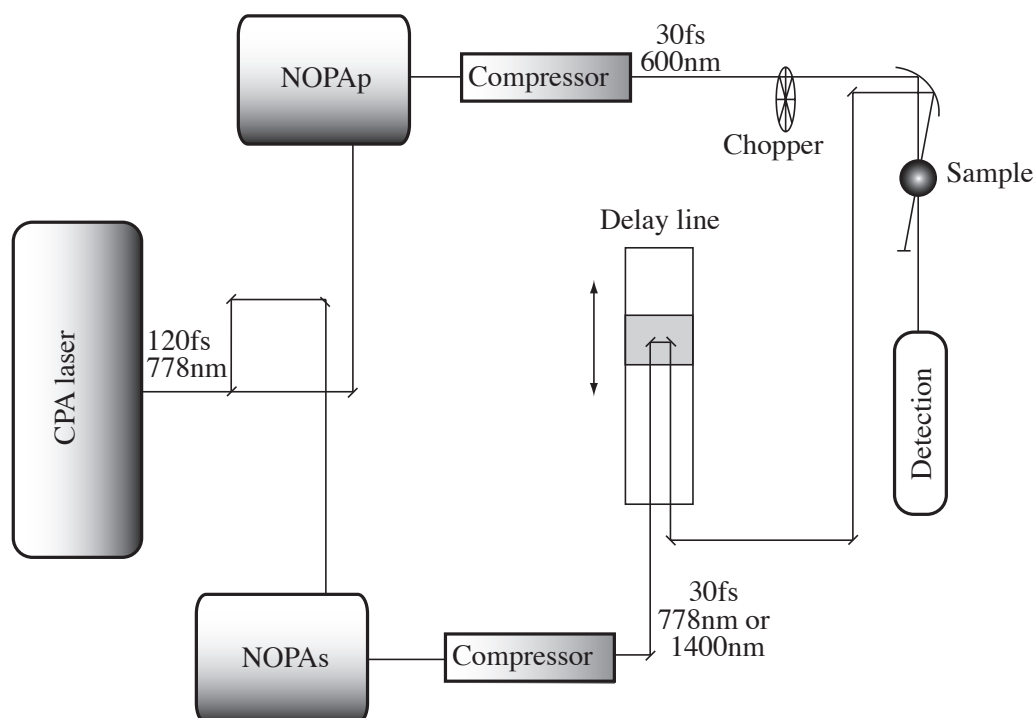
Figure 5.6: Scheme of the femtosecond laser spectroscopy set-up

V.5   Bibliography

(1)   Ricaud, A. *Photopiles solaires*; Presses polytechniques et universitaires romandes: Lausanne, 1997.

(2)   Planta, C. v. Die photoelektrische Charakterisierung der mit Farbstoff sensibilisierten nanokristallinen Solarzellen, EPFL, 1996.

(3)   Krueger, J. Interface engineering in solid-state dye-sensitized solar cells, EPFL, 2003.

(4)   Liska, P. Praktische Aspekte der Licht-Energieumwandlung am Beispiel einer TiO$_2$-Farbstoffzelle, EPFL, 1994.

(5)   Pelet, S. Femtosecond dynamics of electron transfer in the photsensitisation of wide band gap semiconductor, EPFL, 2002.

Chapter VI

The Metal Sulfide Sensitisation

Metal sulfide nanoparticles have been largely investigated in the past decade. PbS nanoparticles were intensively studied for their strong quantum confinement effects. The applications for such particles are for example IR detectors and sensitisers for solar energy conversion. CdS nanoparticles have been used, for example as biological markers due to their tuneable photoluminescence.

In the present study different synthetic techniques were used for producing different types of sensitising nanoparticles. For each technique the experimental parameters were optimised to obtain the maximal efficiency of a solar cell device. The best cells were achieved using PbS as sensitiser; efficiencies of nearly 1 % were measured.

VI.1   Dip-coating preparation

The dip coating technique was developed by Weller et al.[1], and used for the synthesis of a wide spectrum of materials. A detailed explanation of this technique is given in Chapter 4.

The in situ process of particle formation at the surface of the nanocrystalline semiconductor is governed by the interplay of the lattice energy of the formed particle and the strong adsorption of the metal ions at the surface. The lattice energy drives the combination of the metal sulfide molecules to large particles. On the contrary the strong adsorption of the metal ions at the surface arrests the particle growth already at small particle size. It was shown[2] that during the first coating cycle small particles are

formed. They will act as nucleation centers during the following cycles for the new incoming ions.

Good optical absorption of the nanoparticles over the entire visible region is necessary to achieve good solar cell efficiencies. Figure 6.1 shows the absorption spectra of CdS and PbS sensitised TiO_2 layers. The absorption of the CdS sensitised TiO_2 layers is much weaker than for PbS coated layers. The absorption edge of CdS lies around 500 nm while PbS easily absorbs light over the entire visible range. This wide spectral absorption difference makes the lead sulfide a better candidate for TiO_2 sensitisation in solar cell applications than cadmium sulfide, PbS sensitised TiO_2 hence was investigated in more detail in this work. The wave like features observable on the absorption spectra are due to interference phenomenon happening in thin nanocrystalline films. The interferences appear due to the reflection of the incoming light at the glass TiO_2 interface.
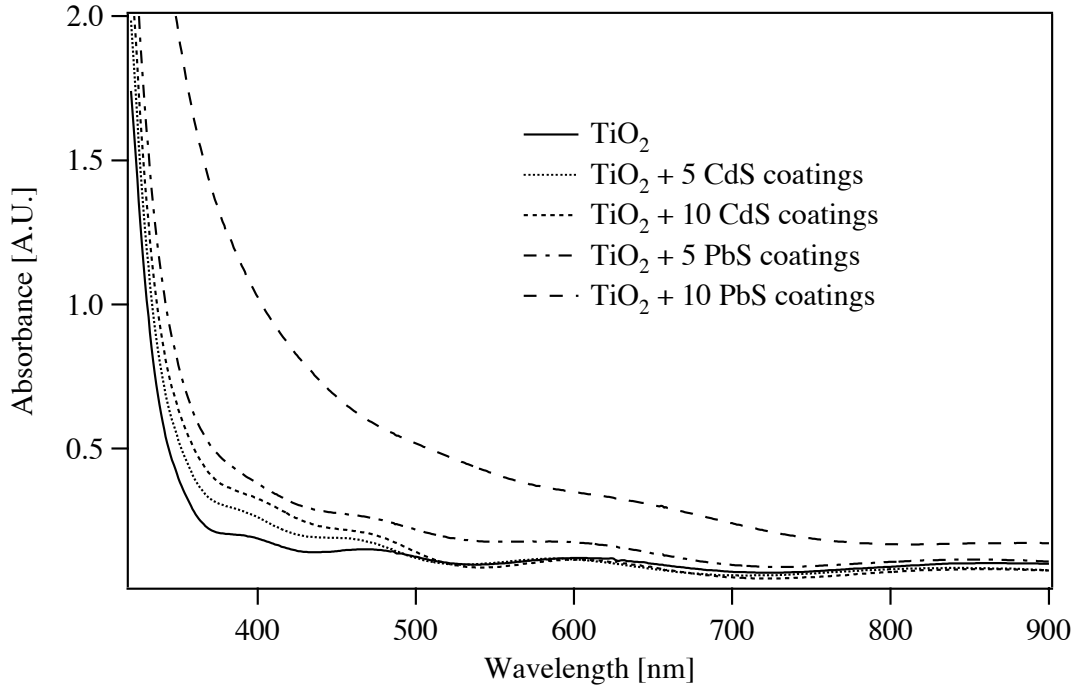
Figure 6.1: Absorption spectra of PbS and CdS sensitised 2μm thick TiO_2 layers.

VI.1.1   Lead sulfide

Lead sulfide is a direct band gap semiconductor. The band gap of the bulk material is 0.41 eV[3,4], which means an absorption band around 3350 nm[5]. The high dielectric constant ($\varepsilon = 17.3$) and the small electron effective mass (< 0.1 m[*]) create an exciton with a large effective Bohr radius (18 nm). The small band gap combined with the large exciton Bohr radius make PbS an interesting system for the observation of the

quantum size effect, as a strong effect would be expected to be observable at sizes smaller than 18 nm.

VI.1.1.1 Absorption spectroscopy

The absorption spectra of PbS give important information about the size and the size distribution of the nanoparticles. It was interesting to see the influence of each consecutive "coating cycle". Figure 6.2 shows the absorption spectra of TiO$_2$ layers sensitised with an increasing number of coatings:
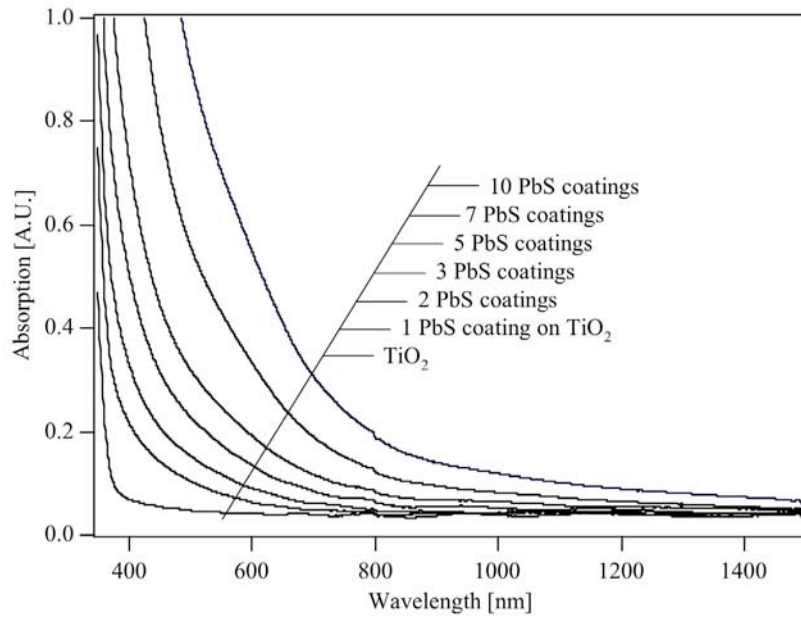
Figure 6.2: Absorption spectra of TiO$_2$ layer sensitised with different numbers of coatings

Two phenomena are observed when increasing the number of coatings; the absorption increase at a certain wavelength is clearly seen as well as the absorption edge shift to longer wavelength. The absorption increase is explained by the increasing amount of deposited PbS, while the increase in size leads to the shift towards longer wavelength, due to the quantum size effect[1,2]. The bigger the particle, the lower the quantum size confinement and thus the smaller the band gap, leading to higher wavelength for the absorption edge.

The particle size can be determined from the absorption spectra by using a theoretical equation derived by Wang[6]:

$$E = \left[E_g^2 + 2 \cdot E_g \cdot \hbar^2 \frac{(\pi/R)^2}{m^*} \right]^{\frac{1}{2}} \qquad (6.1)$$

$$\frac{m^*}{m_e} = 0.085 \qquad\qquad\qquad\qquad (6.2)$$

where E is the energy band gap of the size quantized PbS, E_g the band gap of bulk PbS (0.41 eV), R the particle radius, and m^* is given by Equation 6.2, where m_e is the free electron mass. Figure 6.3 gives a graphical representation of this relation;
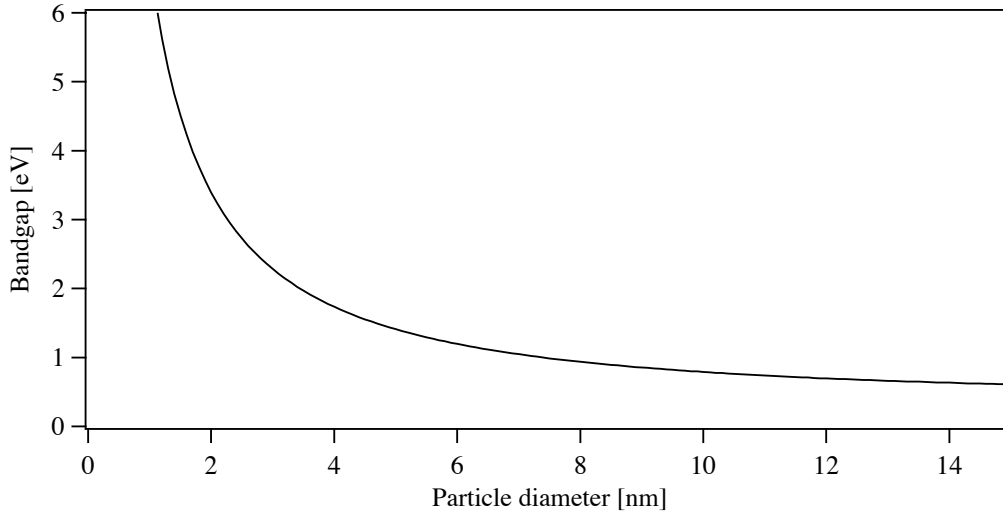
Figure 6.3: Bandgap of PbS as a function of particle size, theoretical calculation following the hyperbolic band model[6].

By applying the absorption onsets found in Figure 6.2, the diameter of the PbS particles Eq.(6.1) to a different number of coatings can be estimated. For one, three and five coatings particle diameters of 3.8 nm, 4.5 nm and 5.1 nm, respectively were found. The good agreement with experimental data is shown in the following by using high-resolution transmission electron microscopy.

VI.1.1.2 High-resolution transmission electron microscopy

High-resolution transmission electron microscopy (HRTEM) was used to confirm the existence of PbS nanoparticles on the TiO_2 surface after the coating treatment. This method also provides a direct measurement of the particle size.

The different materials were distinguished through diffraction pattern analysis. On the picture the small round particles of PbS can easily be distinguished from the much bigger more rectangular TiO_2 particles. The particle size is about 5-6 nm, and is in perfect accord with the calculated value based on the absorption behaviour of such a layer. Surprisingly, the TiO_2 surface is not well covered by the PbS. It is possible that not all the particles are visible as the focusing is very sensitive to the depth. This low coverage has certainly a negative effect on the charge collection at the interface. One

of the major loss mechanisms is the interfacial recombination reaction between an injected electron and a hole present in the hole-conductor. The bare TiO_2 can easily be in close contact with the hole-conductor; this proximity will favour the recombination as the two reactants are close to each other.
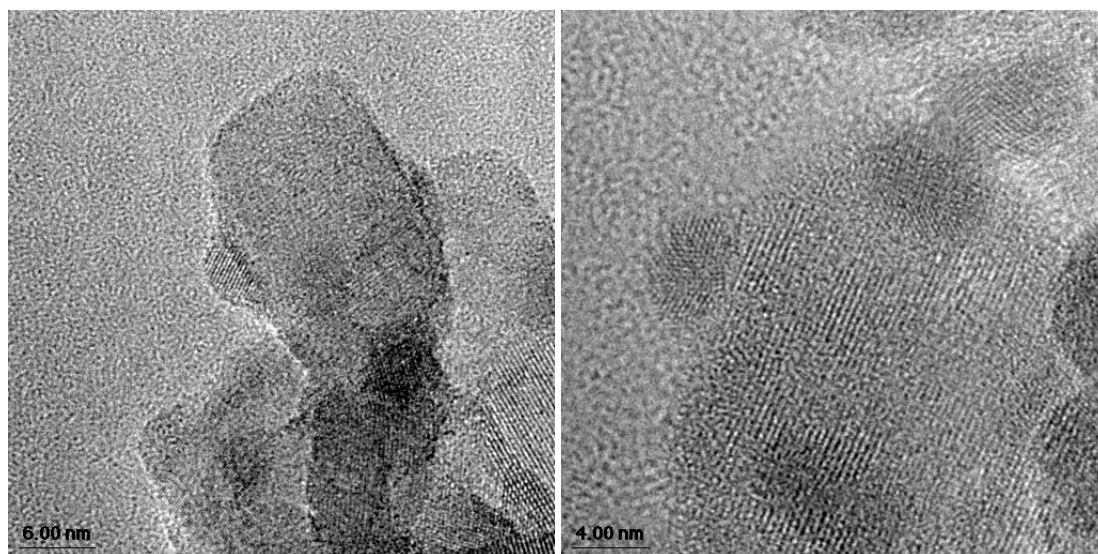
Figure 6.4: High-resolution transmission electron microscopy images of a TiO_2 layer modified with 5 coatings of PbS.

VI.1.1.3 Fluorescence spectroscopy

After light absorption, an exciton (electron-hole pair) is created in the nanoparticle. The recombination of this electron-hole pair induces the fluorescence. The exact mechanism in nanoparticles is very complex. In the case of PbS hot electrons are quickly trapped at the surface into shallow traps. Further trapping can occur into deep traps. The recombination leading to fluorescence occurs between the deep-trapped electron and the hole present in the valence band of the PbS. The fluorescence of PbS nanoparticles is generally weak, but can still be detected in the visible region[7].

In the present work, fluorescence was used to monitor the injection of an excited electron of the PbS into the conduction band of another semiconductor. The feasibility of electron injection into the semiconductor is limited by two parameters. On one hand, the energy level of the semiconductor conduction band and on the other hand, the PbS nanoparticle excited state energy.

As shown in Figure 3.1, the nanoparticle excited state energy level is size-dependent. Meaning that if the synthesised particles are too big, the quantum size effect will not be strong enough and the conduction band of the nanoparticle will be too low to allow

electron injection. Two semiconductors were used, TiO_2 and ZrO_2. TiO_2 (bandgap = 3.2 eV) used as substrate in the solar cell should demonstrate the possible use of such nanoparticles for sensitisation. ZrO_2 has a very large bandgap (about 5 eV), its conduction band is lying much higher than that of TiO_2, and thus, in this case, no injection should be possible. If an electron is injected into the semiconductor, the fluorescence is quenched since no recombination between the electron-hole pair is anymore possible. If the electron cannot be injected and stays on the PbS particle, recombination will occur and fluorescence will be detectable. 2 μm thick nanocrystalline semiconductor layers were used for the measurements, PbS sensitised layers were compared to bare layers. Figure 6.5 shows the measured fluorescence:
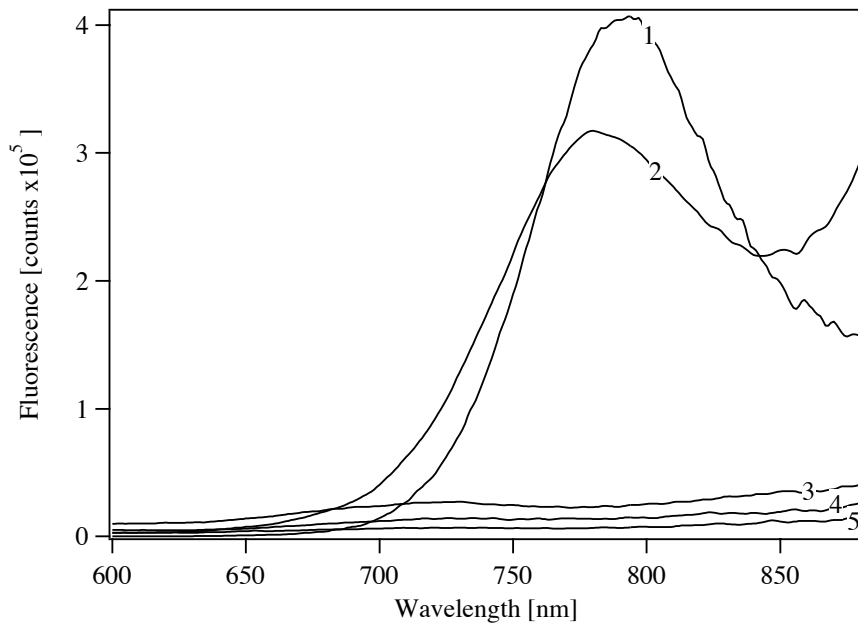
Figure 6.5: Fluorescence spectra of 2 μm thick TiO_2 and ZrO_2 layers, excited at 520 nm with a krypton laser. (1) PbS 8 coatings on ZrO_2, (2) PbS 5 coatings on ZrO_2, (3) bare TiO_2, (4) bare ZrO_2, (5) PbS 5 coatings on TiO_2.

First of all, the bare oxide layers showed no luminescence as expected. The PbS sensitised ZrO_2 samples exhibited a fluorescence peak around 780 nm. This demonstrates the impossibility to inject electron from the PbS nanoparticles into the ZrO_2 conduction band and shows that recombination between the trapped electron and the hole has occurred. On the contrary, the TiO_2 sample sensitised with PbS exhibited no fluorescence; showing the injection of the trapped electron into the TiO_2 which quenches the direct recombination.

Two ZrO_2 samples were sensitised using a different number of coatings (5 and 8). The two fluorescence peaks are slightly shifted from each other: the peak corresponding to

the smaller particles (5 coatings) is centered at 780 nm and the other at 794 nm. This shift is explained by the fact that the smaller particles have a larger bandgap, i.e. the electron-hole energy difference prior to recombination is larger than in the case of larger particles. The generated light through electron-hole pair recombination is of shorter wavelength (higher energy) than for the larger particles.

The minor differences in the signal intensities of the non-fluorescing samples can be attributed to measurement errors, since they depend strongly on the sample angle toward the excitation light, which is difficult to maintain constant. Small differences can also arise from the layer morphology, which differs from one semiconductor layer to the other.

VI.1.1.4 Kinetics of charge recombination

VI.1.1.4.1 The nanosecond laser spectroscopy

As fluorescence was used to demonstrate electron injection from an excited PbS nanoparticle into the TiO_2, nanosecond laser spectroscopy was used to demonstrate hole injection from the reduced PbS into the hole-conductor. This will allow the sensitiser to regenerate, resulting in the oxidation of the spiro-OMeTAD. In fact, this technique does not monitor the spiro-OMeTAD oxidation as it proceeds too fast, but it will measure as already shown in Chapter 5 the following electron-hole pair recombination:

$$e^-\left(TiO_2\right) + h^+\left(spiro-OMeTAD\right) \rightarrow \Delta \qquad (6.3)$$

The recombination will be followed using the oxidised species absorption peak of the spiro-OMeTAD at 518 nm.

A 3 μm thick TiO_2 layer was sensitised with 5 PbS coatings and used for transient absorption difference spectra measurements, shown in Figure 6.6.
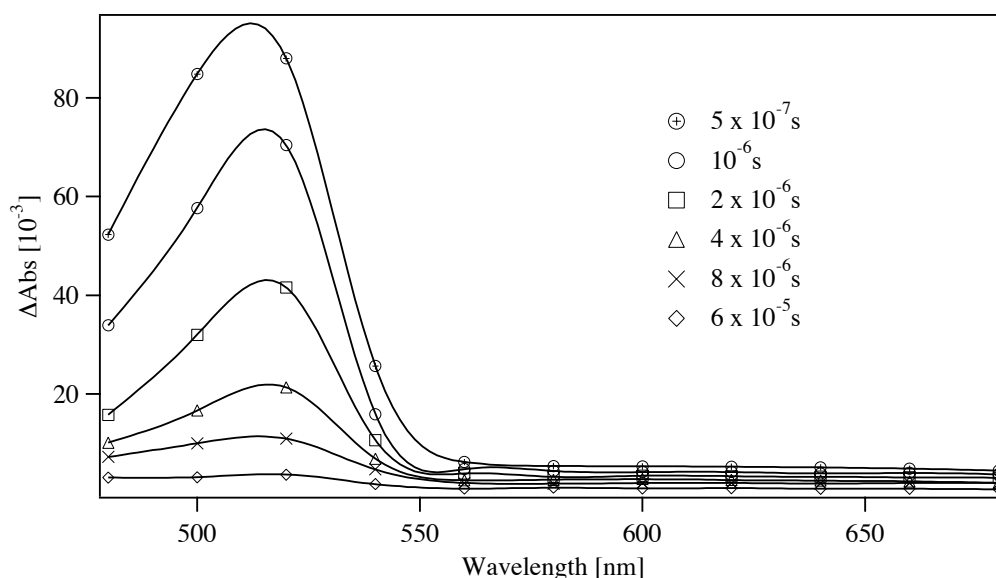
Figure 6.6: Transient absorption difference spectra, excitation wavelength 450 nm, of a 3 µm TiO$_2$ layer sensitised by 5 coatings of PbS and spin-coated with hole-conductor solution (0.25 M spiro-OMeTAD, 13 mM Li(CF$_3$SO$_2$)$_2$N, and 0.4 mM N(p-C$_6$H$_4$Br)$_3$SbCl$_6$) at different time delays.

The intensity of the characteristic oxidation peak at 518 nm is decreasing with time; showing the recombination (eq. 6.3). From this data, the recombination half-lifetime was measured to be 2 µs. This value has to be taken with some care as the recombination is dependent on the laser intensity and on the matrix composition of the hole-conductor. It was shown that the amount of additives, especially the concentration of lithium salt, in the spin-coating solution highly affect the recombination time constants[8].

The presence of oxidised spiro-OMeTAD is a proof for the regeneration of PbS nanoparticles by the hole conductor and that hole injection from the PbS into the spiro-OMeTAD is possible. These measurements are done under open circuit conditions that means the cells are not connected to an external electrical circuit. The generated electrons and holes will not be removed from the interface and will be much more likely to recombine as their concentration is much higher then compared to an operating cell.

VI.1.1.4.2 Femtosecond laser spectroscopy

Femtosecond laser spectroscopy allows the observation of ultra-fast reactions occurring in the system. It is possible to monitor the electron transfer from the PbS particle to a TiO$_2$ particle. It is also possible to observe the hole transfer from the PbS

particle to the hole-conductor. For these measurements, TiO_2 and ZrO_2 were used to allow a comparison between a conducting and an insulating material. Both semiconductors were sensitised with 5 coatings of PbS. To reduce discrepancies due to the use of two separate samples, measurements were first carried out without hole-conductor. The sensitised TiO_2 was then coated with spiro-OMeTAD (the spin-coating solution was 0.12 M spiro-OMeTAD, 7 mM Li $(CF_3SO_2)_2N$, 0.2 mM N(p-$C_6H_4Br)_3SbCl_6$ in chlorobenzene).

For an identical layer thickness ZrO_2 samples absorbed less light than TiO_2 ones. This arises from the fact that the ZrO_2 film porosity is lower than that of TiO_2 films. This explains the smaller signals observed with these samples. Two wavelengths were chosen to probe the system dynamics. A wavelength of 778 nm was chosen to reproduce the results published by Patel et al.[3] concerning the relaxation dynamics of the excited electron. At this wavelength neither the spiro-OMeTAD nor the electrons in the TiO_2 conduction band absorb, therefore these two species will only have a marginal contribution to these measurements. The experimental data are shown in Figure 6.7.

Figure 6.7: Ultra-fast dynamics measurements of PbS sensitised ZrO_2, TiO_2, and TiO_2 coated with spiro-OMeTAD, probed at 778 nm. The curves represent the multiexponential fits of the data for PbS on ZrO_2 (full line), TiO_2 (dashed line) and TiO_2 with spiro-OMeTAD (pointed line).

An other wavelength of 1400 nm was then chosen as probe light. This wavelength corresponds to an absorption maximum of the oxidised hole-conductor. A 600 nm

pump light was chosen because at this wavelength the PbS nanoparticles still absorbs enough light but the hole-conductor only weakly absorbs light. The experimental data are shown in Figure 6.8.
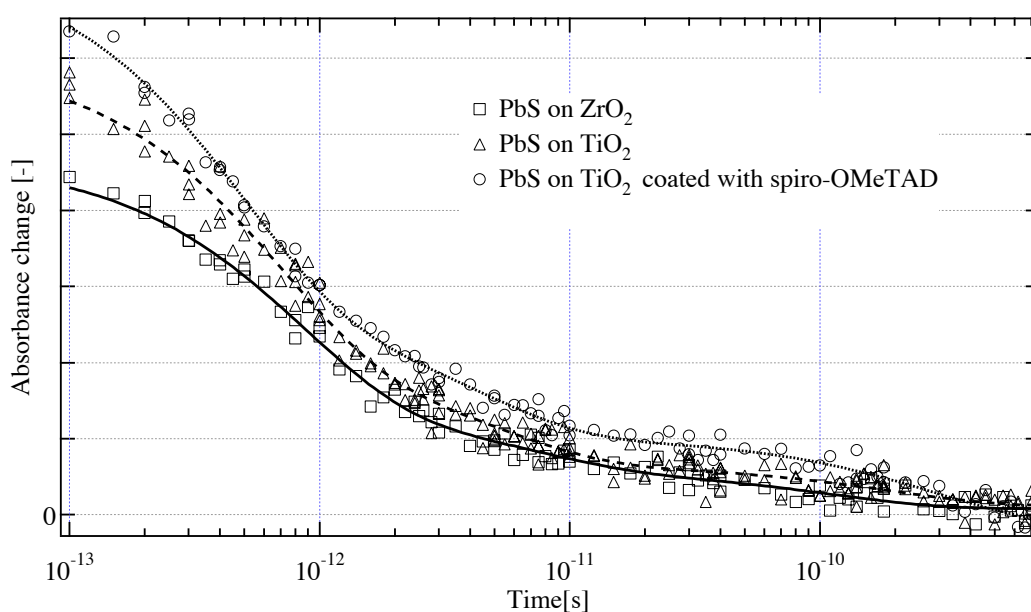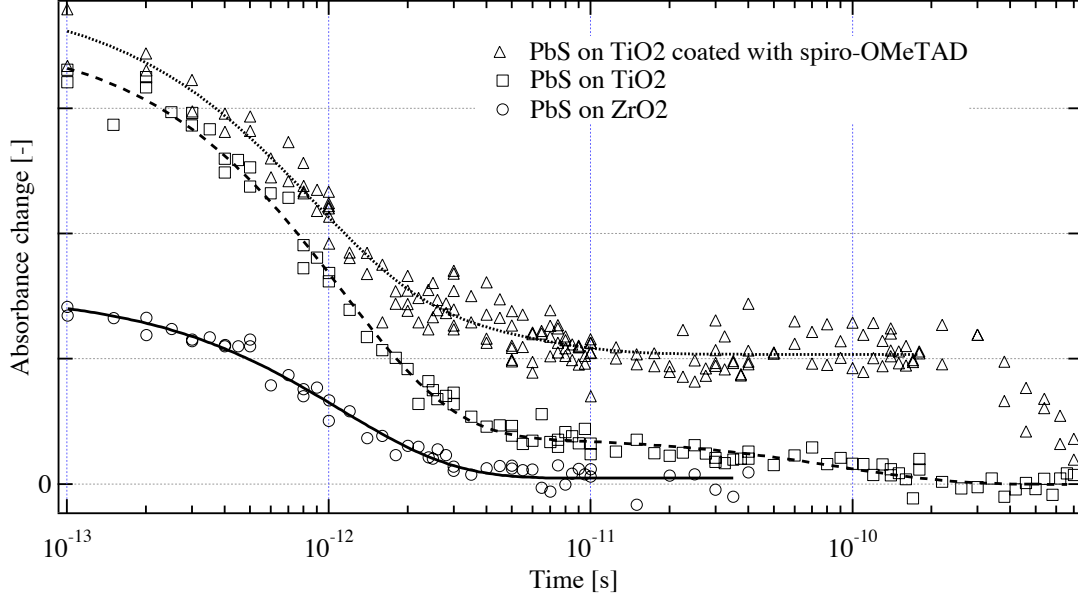

Figure 6.8: Ultra-fast dynamics measurements of PbS sensitised ZrO_2, TiO_2, and TiO_2 coated with spiro-OMeTAD, probed at 1400 nm. The curves represent the multiexponential fits of the data for PbS on ZrO_2 (full line), TiO_2 (dashed line) and TiO_2 with spiro-OMeTAD (pointed line).

The values obtained for the decay time constant from the multiexponential fitting of the experimental data are shown in Table 6.1.

	778 nm	1400 nm
PbS on ZrO_2	0.98 ps ± 0.1 (80%) 31 ps ± 10 (20%)	1.1 ps ± 0.1
PbS on TiO_2	0.83 ps ± 0.1 (81%) 19 ps ± 5 (19%)	1.1ps ± 0.1 (90%) 84 ps ± 43 (10%)
PbS on TiO_2 coated with spiro-OMeTAD	0.47 ps ± 0.07 (61%) 4.2 ps ± 1 (23%) 300 ps ± 150 (16%)	0.78 ps ± 0.2 (60%) 3.9 ps ± 3 (15%) (25%)

Table 6.1: Decay time constants of the experimental values obtained from different type of samples using multiexponential fitting.

The measurements done on ZrO_2 at 778 nm are in good agreement with the values found in the literature[3]. Patel et al. results showed a double exponential decay with time constants of 1.2 ps and 45 ps after light excitation (Equation 6.4). They assigned the rapid time constant to further trapping from shallow traps into deeper traps

(Equation 6.6). The hot electrons (having an energy level higher than the conduction band of the nanoparticle) relaxation and trapping in shallow traps occurs very rapidly, in less than 150 fs (Equation 6.5). The slower time constant was thought to be the recombination of the deep-trapped electrons with the holes present in the valence band of the nanoparticle (Equation 6.7).

$$PbS + h\nu \rightarrow e_{hot}^{-}(PbS) + h^{+}(PbS) \tag{6.4}$$

$$e_{hot}^{-}(PbS) \rightarrow e_{ShallowTrap}^{-}(PbS) \tag{6.5}$$

$$e_{ShallowTrap}^{-}(PbS) \rightarrow e_{DeepTrap}^{-}(PbS) \tag{6.6}$$

$$e_{DeepTrap}^{-}(PbS) + h_{VB}^{+}(PbS) \rightarrow h\nu' + \Delta \tag{6.7}$$

For the same sample the measurements at 1400 nm showed only the rapid part of the dynamics. At this wavelength the electrons in the deep traps are only weakly absorbing and so their presence was not detected.

The differences with the literature values are certainly due to the fact that the synthesis, and the size of the nanoparticles are different but also due to the absence of a capping agent in this work.

When the PbS was deposited on TiO_2, the measured dynamics were very similar to those measured with ZrO_2. This is contrary to what was found in the literature for CdS-TiO_2, where the fast decay slowed down in the presence of TiO_2[9]. The present measurements suggest that electrons are injected from traps in the PbS into the TiO_2 (Equation 6.8) rather than hot electrons (Equation 6.9). It was shown previously that in other systems, the injection into the semiconductor occurs with electrons having high kinetic energies[10,11].

$$e_{Trap}^{-}(PbS) \rightarrow e_{CB}^{-}(TiO_2) + \Delta \tag{6.8}$$

$$e_{hot}^{-}(PbS) \rightarrow e_{CB}^{-}(TiO_2) + \Delta \tag{6.9}$$

From these measurements, it is difficult to say if the electron transfer occurs from the shallow traps or from the deep traps. On one hand, the long lived signal at 1400 nm that could show the presence of the electron in the TiO_2 conduction band would predict that the electron transfer takes place from the shallow traps. On the other hand, at 778 nm the contribution of the two decays are identical for the two semiconductors, indicating that the same number of deep traps are formed in the

presence and the absence of TiO$_2$, showing that the transfer occurs from these lower lying states. The signal at longer times is too weak for the exclusion of one of the two possibilities.

Pelet[12] claimed that the absence of a difference between the two semiconductors shows that the electron transfer is only limited by factors depending on the PbS characteristics. For instance, the injection from shallow traps and deep traps would have the same time constants. This could be understood if both are limited by the same process, which could be the detrapping of the electron. Once the electron is again in the conduction band it can react extremely rapidly with an acceptor state, which can be for example the TiO$_2$ conduction band, or another trap.

The other reaction studied with these experiments is the injection of the hole present in the PbS valence band into the hole-conductor (Equation 6.10).

$$h^+\left(PbS\right) + spiro \rightarrow spiro^+ + \Delta \qquad\qquad (6.10)$$

This reaction is responsible for the 4 ps decay in both measurements at 778 nm and 1400 nm. In other semiconductors this reaction is much faster. This suggests that the holes are trapped as the electrons. The generated oxidised hole-conductor can be seen in the 1400 nm spectra as at this wavelength the spiro-OMeTAD absorbs and lives at least 200 ps. A similar study was done by Bach et al.[13], showing that this reaction occurs between 3 ps and 1 ns for the dye sensitised system. The time constant depends on the distance between the dye molecules and the hole-conductor, but also on the number of spiro-OMeTAD molecules around the dye molecule.

In the case of the measurements at 778 nm, the 4 ps decay cannot be associated with the formation of the oxidised hole-conductor as it has a minimum in its absorption spectrum around this wavelength. Pelet[12] proposes that the disappearance of the hole from the valence band could affect the absorption feature of the trapped electron. The removal of the hole lengthens the lifetime of the electron in the conduction band as a third decay component of 300 ps is necessary to fit correctly the decay of the electrons. This is about ten times longer than in the absence of the spiro-OMeTAD.

At 1400 nm, a third exponential component is also present but could not be fitted; it represents about 25 % of the total decay. Taking in account that during these measurements a high number of electron-hole pairs per particle are created due to the high power of the laser pulses, it is possible that the recombination (Equation 6.3) is accelerated comparing to the nanosecond laser measurements.

$$e^- \left(TiO_2 \right) + h^+ \left(spiro - OMeTAD \right) \rightarrow \Delta \qquad\qquad (6.3)$$

VI.1.1.5 Photovoltaic characterisation

Most of the previously reported work concerning nanoparticle sensitisation of semiconductors measured the photoelectrochemical behaviour using three electrode systems. The modified layer immerged in the electrolyte acts as working electrode whereas the counter electrode is often platinum and the reference electrode Ag/AgCl. The electrolyte is an aqueous Na_2S/Na_2SO_3[1,14-16] or ferro/ferricyanide[17] solution for example. In these systems, corrosion and photocorrosion are often observed mainly due to the aggressive nature of the electrolyte and the mass transport phenomena, which leads to photo-induced particle growth. Photocorrosion generally involves chemical reactions of charge carriers with the electrolyte or the bulk material itself. These problems should not exist in the present system based on a solid electrolyte, as there is no charge transfer involved in the regeneration process.

The photovoltaic measurements are operated on complete cells, the preparation of such devices as seen in Chapter 4 involves several critical steps. Many parameters play an important role in the photovoltaic behaviour of the final device, as for example the TiO_2 characteristics, the amount of deposited sensitiser or the composition of the hole-conductor matrix. For these reasons, the comparison from one cell to another will be done inside a same series but rarely from one series to the other. All the cells in one series are based on the same TiO_2 layer and are assembled at the same time.

VI.1.1.5.1 Number of coatings optimisation

As shown above, the consecutive coatings enhances the absorption of a semiconductor layer by increasing the particle size of the deposited nanoparticles. Vogel et al.[1] showed that the number of coatings has an optimum at which the photocurrent is maximum. On one hand, the more coatings are performed on a layer the more the layer will absorb photons and thus be able to generate more electrons. On the other hand, with an increased number of coatings the particles grow and consequently the lowest quantized level occupied by the photoexcited electron gradually decreased energetically to the conduction band of the bulk material. As the latter lies energetically below the conduction band of the TiO_2, an electron transfer from PbS into TiO_2 becomes impossible. The use of nanoporous electrodes introduces

another problem when many coatings are applied to a layer. The deposited material will fill up the smallest pores, leading to a decrease of the effective surface area of the nanoporous layer. Consequently, regeneration will not be possible any more as the hole-conductor cannot enter these pores, and so the charge transport decreases.

The optimum number of coatings in this work was determined by current-voltage and IPCE measurements. During the whole work the thickness of the TiO_2 layers was maintained around 2 µm, as this was previously found to be the optimal thickness for the solid-state system. This value can vary slightly from one colloidal paste to the other depending on its porosity, particle size and specific surface. The use of rather thin films in solid-state device comparing to the liquid electrolyte device is mainly due to the high viscosity of the hole-conductor solution prior to spin-coating. Only thin films allowed efficient pore filling.

A different number of coatings was tested. Some typically obtained values are given in Figure 6.9. At low light intensity (1% Sun) one can observe that the short-circuit current is decreasing with an increasing number of coatings. The "driving force" leading to the electron injection from the PbS into the TiO_2 decreases with increasing size, due to the quantum size effect; the energy difference between the excited electron and the conduction band of the TiO_2 decreases. At 10% Sun, the situation is different, both cells with three (PbS3x) and five (PbS5x) coatings have roughly the same I_{sc}. The above-explained phenomenon is still valid in this case, but is competing with others. The low absorbing layer will reach its absorption saturation at low light intensity; in this case PbS3x is saturated at lower light intensity than PbS5x. Thus at 10 % Sun, more photons are absorbed by the latter as the former is saturated and cannot absorb more even if the light intensity is higher. At full Sun illumination this effect is even more pronounced, the I_{sc} of PbS5x being higher than the one of PbS3x.

For 1 % and 10 % Sun, the ratio of the I_{sc} of PbS5x and PbS7x is constant, showing that at these light intensities, the difference arises only from the quantum size effect, i.e. the difference in the "driving force". At full Sun illumination, this ratio is smaller, indicating that the saturation effect is arising in the PbS5x layer. From this it can be extrapolated that at higher illumination intensities the PbS7x is performing even better than the PbS5x.
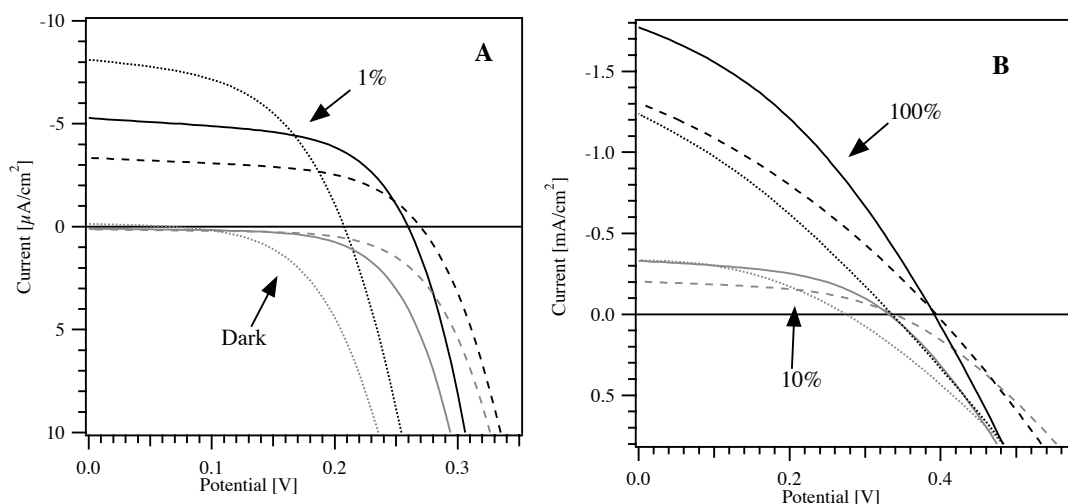
Figure 6.9: Current-voltage characteristics of TiO$_2$ layers modified with three coatings (dotted line), five coatings (full line), and seven coatings (dashed line) of PbS in the dark (grey lines on A), at an illumination intensity of 1% of Sun (black lines on A), of 10% of Sun (grey lines on B), and 100% of Sun (black lines on B) (corresponding to AM 1.5 1 mW/cm^2 10 mW/cm^2 and 100 mW/cm^2). The spin coating solution for the deposition of the hole conductor contained 0.25 M in spiro-OMeTAD, 13 mM in Li(CF$_3$SO$_2$)$_2$N and 0.4 mM in N(p-C$_6$H$_4$Br)$_3$SBCl$_6$.

It is also very interesting to see that the V$_{OC}$ is increasing with an increasing number of coatings. The open-circuit voltage is highly dependant on the interfacial recombination. The bigger the particles the more TiO$_2$ is covered. This could lead to a recombination decrease between the TiO$_2$ conduction band electron and the hole present in the hole-conductor, as the contact surface is shrinking. This point of view will be discussed in detail in a following section when discussing about PbS deposited by chemical bath deposition.

From these measurements, TiO$_2$ with five coatings was shown to be the optimum configuration for the present system. This conclusion from the current voltage measurements was confirmed by the IPCE measurements shown in Figure 6.10.

The IPCE spectra show the existence of an optimum number of coatings. It is interesting to compare the photovoltaic behaviour to the absorption spectra. The one time coated layer (PbS1x) and the ten times coated layer (PbS10x) have similar IPCE values, even if the absorption is much higher for the latter sample over the measured range. This arises from the duality explained above between absorption (absorption saturation) and the injection "driving force" ruled by the quantum size effect. The pore filling in the sample coated 10 times is certainly affected due to the large amount of deposited material, decreasing the charge regeneration.
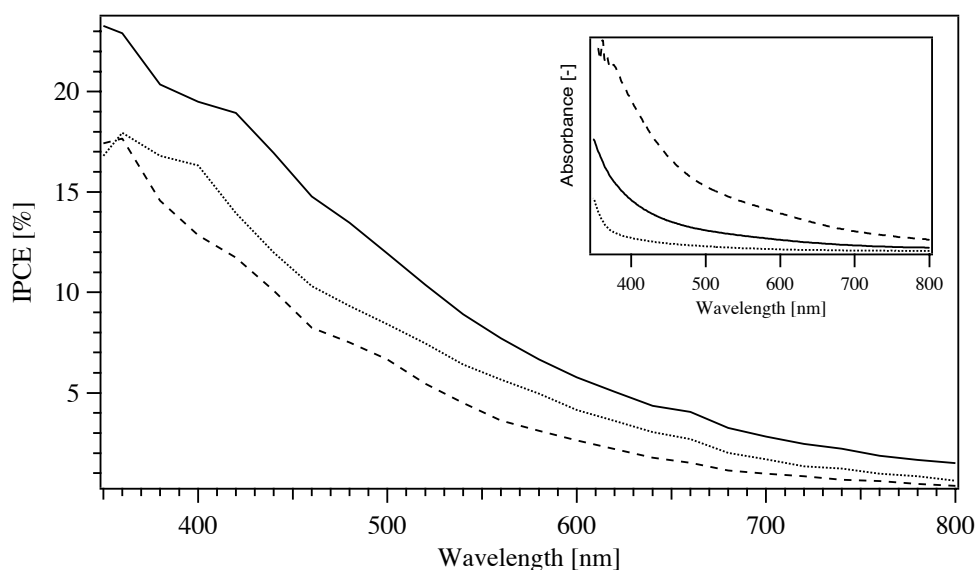
Figure 6.10: Dependence of the IPCE spectra on the number of coatings on a 2 μm thick TiO$_2$ layer; one coating (dotted line), five coatings (full line), ten coatings (dashed line). The inset shows the absorption spectra of these layers.

VI.1.1.5.2 Influence of the tert.-butylpyridine (tBP)

The influence of base on the solid-state device was investigated[8]. It was shown through Kelvin probe measurements that the semiconductor work function[*] could be varied by surface modification using different bases. In the case of tBP the modification effect is an increasing short-circuit current and open-circuit potential, leading to an increase of the overall efficiency. These effects are different in the classical dye-sensitised solar cell where only the U$_{OC}$ is shifted to higher voltage by modification with tBP[18,19]. It was shown[20] that the replacement of the water coordinated to Ti(IV) at the surface of the TiO$_2$ by an adsorbate decreases the surface state depth. If the Lewis basicity of the ligand is strong enough, the surface state electronic level will be pushed into the conduction band, eliminating the electron trapping. The U$_{OC}$ increase in the dye-sensitised solar cell can be explained by this phenomenon. In the solid-state device the effect of the additives was shown to be a screening effect more than an effect on the bands energetics.

---

[*] The work function of a semiconductor equals the energy difference between the vacuum level and the Fermi level. It can be measured using the Kelvin probe technique, measuring the work function difference between a reference and the sample.

The tBP addition to the hole-conductor matrix was supposed to have the same effect in the quantum dots-sensitised system. Indeed the U_{OC} increase was observed but was accompanied by a dramatic loss in collected current. The measured values are shown in Table 6.3:

	U_{OC} [mV]		I_{SC} [µA/cm^2]		FF [%]		η [%]	
	10 %	100 %	10 %	100 %	10 %	100 %	10 %	100 %
Without tBP	251±10	305±11	**386±36**	**1925±310**	44±2	29±1	0.44±0.04	0.18±0.02
With tBP 0.1 M	378±7	463±7	**3±0.4**	**28±5**	70±2	64±1	0.01	0.01

Table 6.2: Influence of the tBP in the device performance at 10% and 100% sun light illumination (AM1.5)

Several explanations could be found for this phenomenon. One could speculate about the PbS destruction by the tBP, but as no discoloration of the sample was observed after spin-coating the hole-conductor solution containing the tBP, this hypothesis was ignored. Since it was shown that the surface states can be pushed up into the conduction band of the TiO_2 by the use of tBP, the energetics for nanoparticles might be weaker than for dye sensitised systems. By applying tBP this driving force can be lowered or even cancelled. This would make the injection unfavourable, and explain the very low current for the tBP-modified devices.

VI.1.2 Capped PbS

It has been reported that PbS sensitised TiO_2 electrodes suffer from photocurrent instability under illumination[15,21]. These observations were made in systems using water-based electrolytes containing Na_2SO_3 and Na_2S. In the presence of light the sulfide is supposed to dissolve;

$$\left(PbS\right)_n \xrightarrow{\ hv\ } \left(PbS\right)_{n-1} + Pb^{2+} + S^{2-} \tag{6.12}$$

It was shown through absorption spectroscopy that upon illumination the particle size is increasing[22]. The explanation for this is the deposition of the released Pb^{2+} and S^{2-} on larger particles.

Several routes were followed to prevent the photocorrosion of the PbS sensitised TiO_2 electrodes: the deposition of a thiol layer at the surface was used[22] and the formation of co-sensitised electrodes with capped-sulfides was tested[16]. Both techniques lead to an enhancement of the stability. The thiols will form a protective layer around the PbS particles so that dissolution and particle growth will be hindered to a large extent, and the photostability improved.

The choice of CdS to co-sensitise PbS/TiO_2 was made for several reasons; a good crystal lattice matching, an increased injection driving force for excited electrons and an increased light absorption. To enhance the stability of PbS or the CdS capped PbS, ZnS was used. ZnS is a wide band gap semiconductor (E_g = 3.6 eV), stable under irradiation, and has similar chemical properties to the other sulfides allowing them to co-exist. CdS and ZnS are deposited using the same dip-coating method as for PbS.

These methods improve significantly the efficiencies of two and three electrodes systems using aqueous electrolytes. The solid-state device suffers less from instability, as no liquid electrolyte is present hindering the dissolution of the particles under illumination. The better charge separation by using CdS co-sensitisation should also be effective in the solid-state system. The use of ZnS should passivate the PbS surface, rendering the electron trapping less likely to happen.

VI.1.2.1 Absorption spectroscopy

Different combinations of PbS, CdS and ZnS were studied. All the electrodes were first sensitised with PbS before adding CdS and/or ZnS. The influence of each layer in the absorption spectra was measured and is shown in Figure 6.11.

It is astonishing to see that ZnS layer addition on top of PbS layers shifts the absorption edge towards the red. Similar effects have been observed previously[23,24]; the exciton is presumed to leak partially into the ZnS matrix. This effect is more pronounced in smaller dots where the leakage of the exciton into the ZnS shell has a more dramatic effect on the confinement energies of the charge carriers. The CdS layer increases also the absorption of the sample over the whole visible range. Five coatings of CdS were deposited using recommendations found in the literature[16].
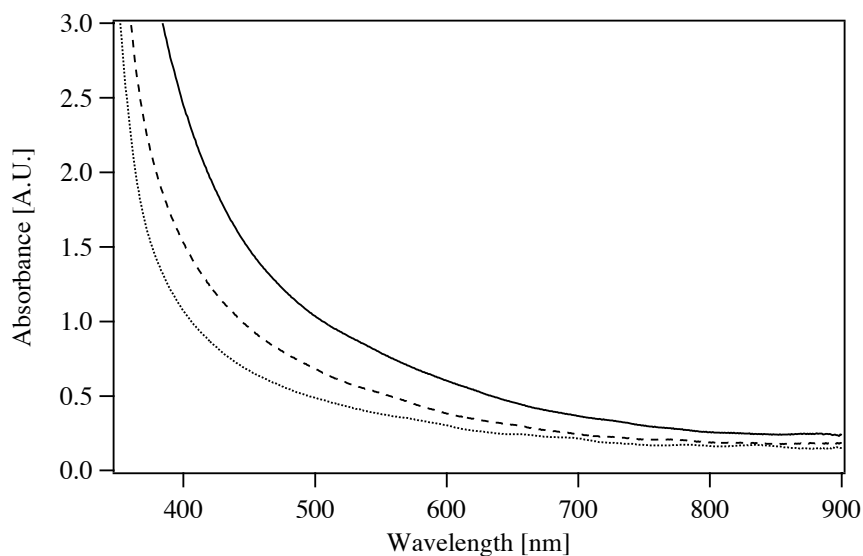
Figure 6.11: Absorption spectra of three TiO$_2$ layer modified with; (a) three coatings of PbS (dotted line), (b) three coatings of PbS and three coatings of ZnS (dashed line), (c) three coatings of PbS, five coatings of CdS and three coatings of ZnS (full line).

VI.1.2.2 Fluorescence spectroscopy

The fluorescence of core-shell like nanoparticles has been investigated recently, for a large variety of compounds. For example, CdSe/ZnS[23,25],CdSe/CdS[26], InP/ZnS[27], CdS/ZnS[28], or PbS/CdS[24] were studied. The goal of the epitaxial overcoating of a core nanocrystallite with a large band gap semiconductor is the surface passivation. This passivation strongly enhances the luminescence of those particles. Good epitaxial overcoating requires the use of a wide band gap material with compatible lattice constants and crystal structure. PbS as a rock-salt crystal structure, this is compatible with the zinc-blende structure of ZnS or CdS. The zinc-blende structure, like the rock-salt structure is a cubic structure. In the present work the situation is quite different, the PbS nanoparticles are already deposited on a substrate and are not in solution as in the previous studies. The semiconductor shell will not cover the contact surface between substrate and PbS. For this reason the passivation effect will not be as efficient; surface states will still exist at the interface between the nanoparticle and the TiO$_2$. The fluorescence spectra of ZnS capped PbS is shown on Figure 6.12. Clearly, bare PbS fluorescence is stronger than the capped PbS one. This result is astonishing as it is contrary to the above discussion. As the PbS surface is passivated, electron trapping is reduced and thus the exciton recombination more likely to happen. As explained previously, the exciton is able to leak from PbS to ZnS. Once in ZnS, the exciton, not energetic enough, is not able to recombine following a radiative pathway

as the band gap is above 3 eV (ZnS luminescence around 400 nm[29]). The observed quenching of the fluorescence is due this non-radiative exciton recombination occuring in ZnS.
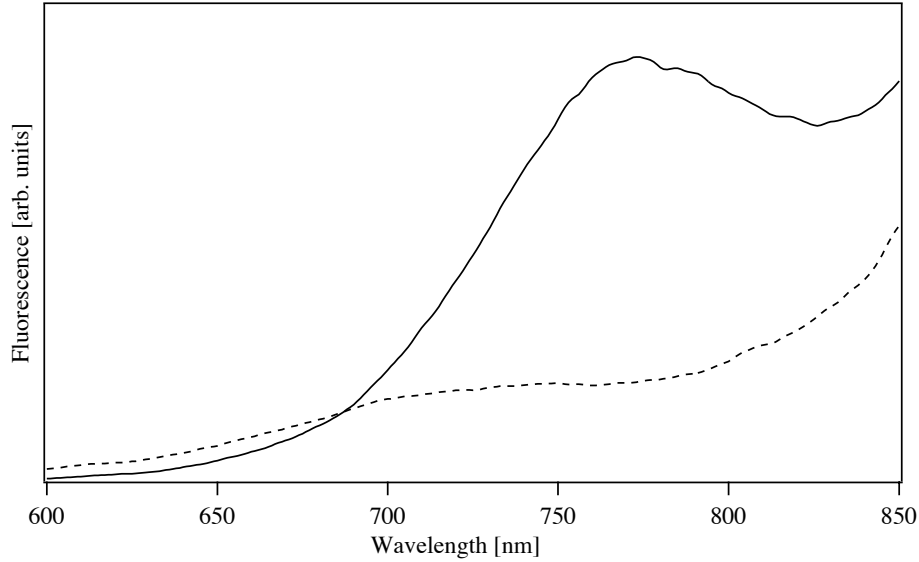

Figure 6.12: Fluorescence spectra of PbS (full lines) and ZnS-capped PbS (dashed lines) modified ZrO_2 layer with five coatings of PbS and three coatings of ZnS.

VI.1.2.3 Nanosecond laser spectroscopy

Nanosecond laser spectroscopy was used to see the influence of the capping of PbS on the recombination kinetics. Figure 6.13 illustrates the influence on the recombination kinetic decays.
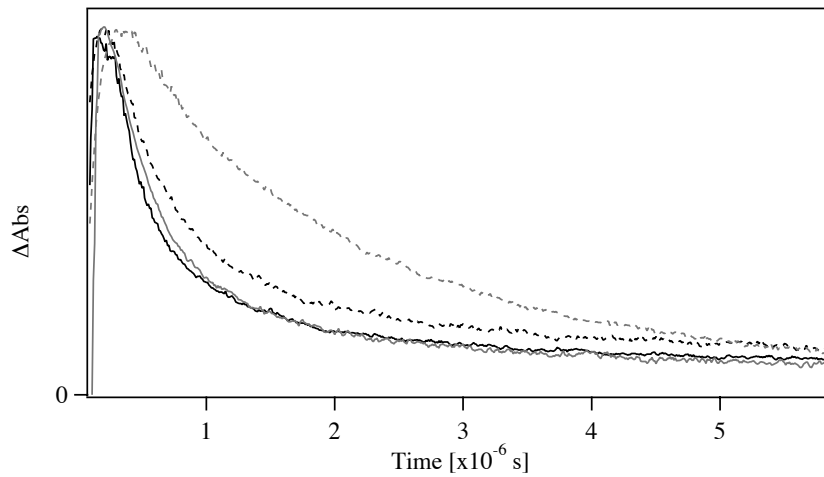
Figure 6.13: Transient absorption decay kinetics of the hole-conductor cation; PbS 3 cycles (dark full line), PbS 3 cycles capped with ZnS 3 cycles (grey full line), PbS 3 cycles capped with CdS 5 cycles (dark dotted line), and PbS 3 cycles capped with CdS 5 cycles and ZnS 3 cycles (grey dotted line). The spin coating solution for the deposition of the hole conductor contained 0.25 M in spiro-OMeTAD, 13 mM in $Li(CF_3SO_2)_2N$ and 0.4 mM in $N(p-C_6H_4Br)_3SBCl_6$.

It can be seen that the capping of PbS influences the interfacial recombination. The decay kinetics clearly show that the more coatings applied to a layer, the slower the recombination. It was oroginally assumed that the first coating deposits smaller growing centres on the TiO_2 and that the following coating would increase the size of these centers. The present results tend to indicate that increasing the number of coatings also increases the covered TiO_2 surface. Indeed the TiO_2 covering diminishes the direct contact between hole-conductor and TiO_2, reducing the interfacial recombination.

Good fitting of the decays kinetics could be obtained by using a single exponential function. The calculated time constants vary by a factor of three from PbS to PbS capped with CdS and ZnS.

Sample	k_r [s^{-1}]
PbS 3x	1.85e+06
PbS 3x + ZnS 3x	1.72e+06
PbS 3x + CdS 5x	1.43e+06
PbS 3x + CdS 5x + ZnS 3x	5.92e+05

Table 6.3: Single exponential time constants for different types of capped PbS nanoparticles

VI.1.2.4 Photovoltaic measurements

Following on from this previous work, the photovoltaic performance would be expected to be enhanced[16]. Adding the CdS layer and the ZnS layer could roughly double typical IPCE values at 540 nm as shown on Figure 6.14.

This observation is similar to the work of Yang et al.[22]. They claimed that the increased IPCE is due to the relative position of the conduction band of TiO_2, PbS and CdS. The conduction band of quantum sized PbS lies above the TiO_2 one; moreover the conduction band of CdS is more energetic than the PbS one. The energetic differences between the conduction bands of the semiconductors bring about a driving force, which facilitates the charge carrier transfer from the conduction band of CdS to PbS and then to TiO_2. This energetic cascade provides for a better charge separation and thus higher IPCE values.
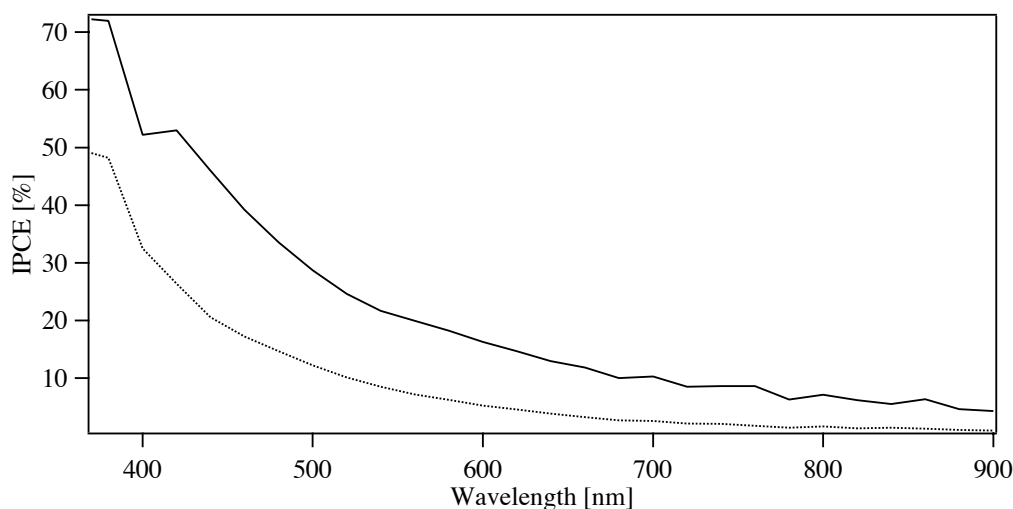
Figure 6.14: IPCE spectra of solid-state devices. The TiO_2 has been sensitised with three coatings of PbS (dotted line) and three coatings of PbS followed by five coatings of CdS and three coating of ZnS (full line). The spin coating solution for the deposition of the hole conductor contained 0.25 M in spiro-OMeTAD, 13 mM in $Li(CF_3SO_2)_2N$ and 0.4 mM in $N(p-C_6H_4Br)_3SbCl_6$.
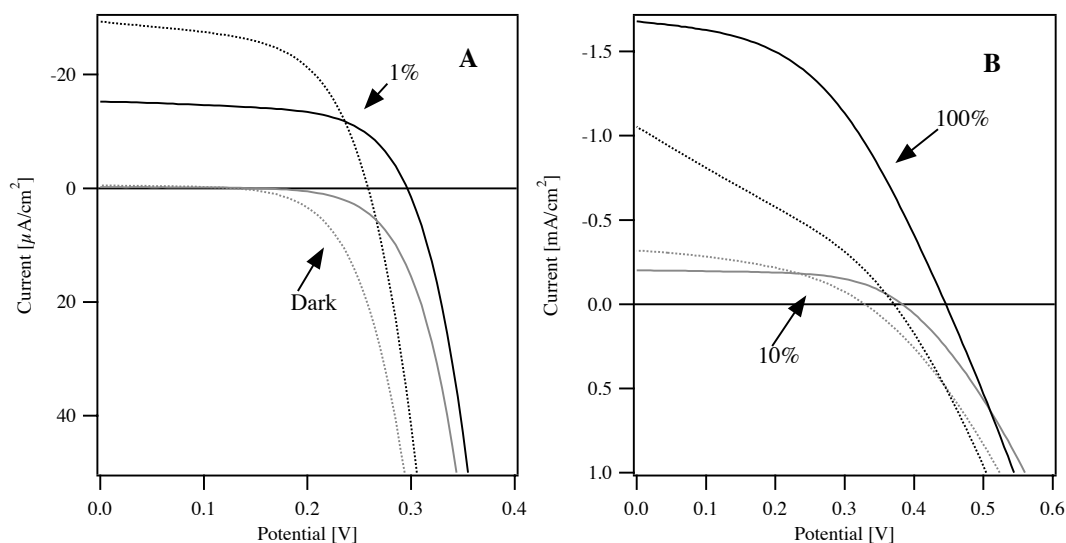
Figure 6.15: Current-voltage characteristic of TiO_2 layers modified with three coatings of PbS (full lines) and three coatings of PbS plus five coatings of CdS and three coatings of ZnS (dotted lines) in the dark (grey lines on A), at an illumination intensity of 1% Sun (black lines on A), of 10% Sun (grey lines on B), and 100% Sun (black lines on B) (corresponding to AM 1.5 1 mW/cm^2, 10 mW/cm^2, and 100 mW/cm^2). The spin coating solution for the deposition of the hole conductor contained 0.25 M in spiro-OMeTAD, 13 mM in $Li(CF_3SO_2)_2N$ and 0.4 mM in $N(p-C_6H_4Br)_3SbCl_6$.

The IPCE spectra are taken at very low light intensity (around 1 mW/cm^2). The current-voltage characteristics shown in Figure 6.15 correspond to this intensity; one

sees that the I_{SC} of the capped device is doubled in comparison with the non-capped device. This observation is in very good accordance with values of Yang et al.[22]. The situation is different when comparing the V_{OC} values of the two devices. This difference is even more astonishing when taking into account the recombination kinetics measurements. The decreased recombination reaction should lead to an increase in I_{SC}, as observed, but also an increase in V_{OC}. Unfortunately the sensitisation with capped nanoparticles leads to lower V_{OC} than PbS nanoparticles. Globally, the efficiency of the device sensitised with capped nanoparticles is higher than the non-capped one (0.53% and 0.35% respectively). It was observed with other materials that the coating of TiO_2 using a semiconductor inhibits the interfacial recombination[30-32], leading to higher V_{OC} values. Obviously, the PbS capping in the solid-state device does not follow this observation. One reason for this could be that the CdS and ZnS only deposit on PbS and not at all on TiO_2, but this is unlikely as the preparation technique is identical to the one of Yang et al.

The measurements done at higher light intensity may help for the understanding. At 10% Sun, the I_{SC} of the capped sensitised device is only slightly higher than the I_{SC} of the pure PbS device. This inversing tendency is confirmed by the full Sun measurement where the I_{SC} of PbS sensitised device is higher than that of the capped device. This tendency has not been observed in the characterisation of the two electrode system using a liquid electrolyte. The PbS capping certainly causes the shrinking of the pore sizes by bringing in more material. With this phenomenon some pores may be filled up, meaning that no hole-conductor will be present to regenerate the sensitiser. This leads a decrease of active surface area. As known, the I_{SC} of a solar cell depends strongly on the active surface area of its electrode; the lower the surface, the lower the current.

The current-voltage curves of the capped devices at 10% and 100% Sun are characterised by a low shunt resistance. This denotes some short-circuit problems inside the device, occurring for example at the interface when the injected electron recombines with the hole present in the non-regenerated sensitiser.

The capping of PbS nanoparticles with CdS and ZnS leads to a change of the morphology of the TiO_2 layer by filling up a certain amount of pores. At low light intensity this has no influence on the performance of such devices, thus the capping increases significantly the overall cell efficiency. At high light intensity, the lower surface area causes lower short-circuit currents, and thus lower efficiencies. To

measure the promised role of the capping, some stability measurements should be done on this type of device. In this framework, priority was given to the increase of the cell efficiency by trying other deposition techniques.

VI.2   Chemical bath deposition

The chemical bath deposition technique has been widely used for many years for the deposition of thin films of metal chalcogenide. This technique was developed for large-scale applications for which it is well suited. The goal of this technique in this work was to study the difference between sensitisation by distinct semiconductor nanoparticles and by thin layers of semiconductor, composed of nanoparticles. The interface reactions between TiO_2 and hole-conductor should be reduced as the sensitiser covers the interface. This supposition was made by comparison with recent work done on semiconductors (SnO_2, TiO_2) coated by several oxides[30-32], especially Al_2O_3. In the dye-sensitised cell the sensitiser is adsorbed on the Al_2O_3 and injects energetic electrons to the semiconductor, tunnelling across the Al_2O_3 barrier. Once the electrons relax to the conduction band of the semiconductor, the Al_2O_3 barrier prevents the recombination of the electron with the dye cation on one side, but it also prevent the recombination with I_3^- ions at the electrolytic interface. The deposition mechanisms of the PbS layer have already been explained in detail (see Chapter 4). Briefly, TiO_2 layers are immersed in a highly basic solution containing Pb^{2+} ions S^{2-} ions and the complexing agent, triethanolamine (TEA). The slow release of S^{2-} displaces the complexing equilibrium of Pb^{2+} by the reaction of free lead ions with the sulfide ions. Two main mechanisms can occur depending on the relative concentration of the species; ion-by-ion growth in situ on the substrates or bulk precipitation followed by migration to the substrate.

This chapter discusses only work done on lead sulfide, studies on lead selenide and cadmium selenide are presented in Chapter 7.

VI.2.1   Absorption spectroscopy

Absorption spectroscopy was used to monitor the influence of the different experimental parameters; deposition duration, sintering temperature, sintering atmosphere, and acid rinsing.

It can easily be understood that the deposition duration will influence the amount of deposited material, and thus the absorption characteristics of the layer. After deposition, previously reported work[15] indicated that a washing process using 1 M HCl was beneficial, the influence of this was also studied. Finally, the layers are sintered in a tubular furnace; the effects of the temperature and the atmosphere of this step were also examined.
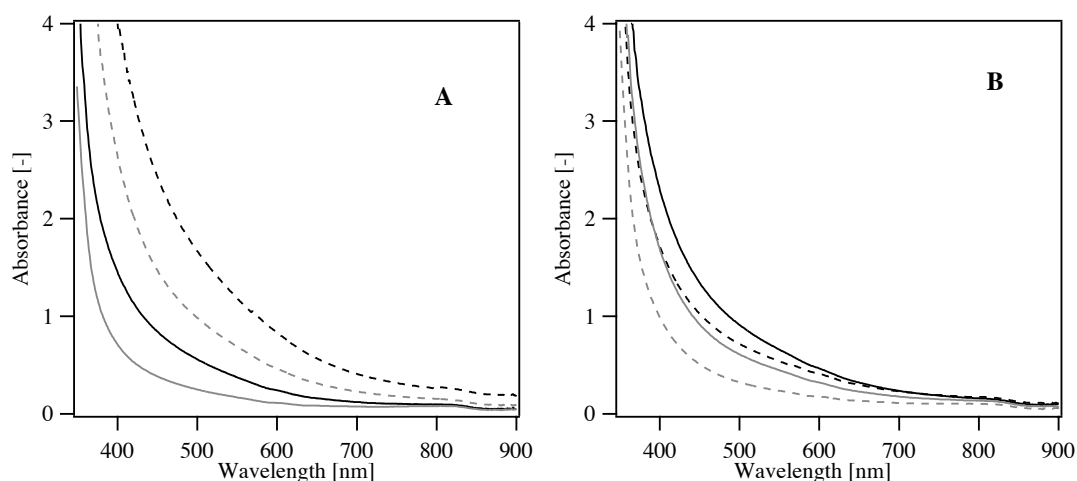

Figure 6.16: Absorption spectra of PbS modified TiO_2 using chemical bath deposition, and sintered at 150°C under an air atmosphere. Influence of the deposition time and effect of the sintering (A); 50 minutes of deposition (dashed lines), 30 minutes of deposition (full lines), before sintering (black lines) and after sintering (grey lines). Influence of the HCl 1 M treatment after deposition (B); sample rinsed with water (full lines), rinsed with HCl (dashed lines), before sintering (black lines) and after sintering (grey lines).

The deposition duration effect is clearly seen on Figure 6.16; the longer the sample is immersed, the more PbS is deposited, and the more the formed layer absorbs light. This parameter will be optimised using photovoltaic measurements as the duality between a more absorbing layer and pore filling is the same as for the dip-coating method, i.e. one has to be very careful not to fill up the TiO_2 pores. Acid treatment diminishes the layer absorption due to the removal of PbS present in the sample but not attached on TiO_2. After this treatment the layer coloration tended to be less homogenous than before. This indicates that the acid was too strong by destroying partially the PbS layer.

After sintering in air the layers exhibited a lower absorbance; this is explained by a partial PbS oxidation during the treatment. The oxidation could be minimised by operating the sintering under argon atmosphere.

As shown in Figure 6.17 (A), the furnace atmosphere influences largely the layer absorption. In air, the lower absorption over the entire spectrum is due to the partial oxidation of PbS. Using argon as atmosphere, the absorption is increased for wavelength shorter than 465 nm and decreased above this limit. This behaviour shows that the particles composing the deposited layer become smaller with sintering, an effect arising from the quantum size effect. The oxidation occurring under air and leading to a decrease of the absorption is avoided by using an argon atmosphere during the sintering. This oxidation was shown[15] to produce $PbSO_4$ following Equation 6.13;

$$\left(PbS\right)_s + 2O_2 \rightarrow \left(PbSO_4\right)_s \tag{6.13}$$

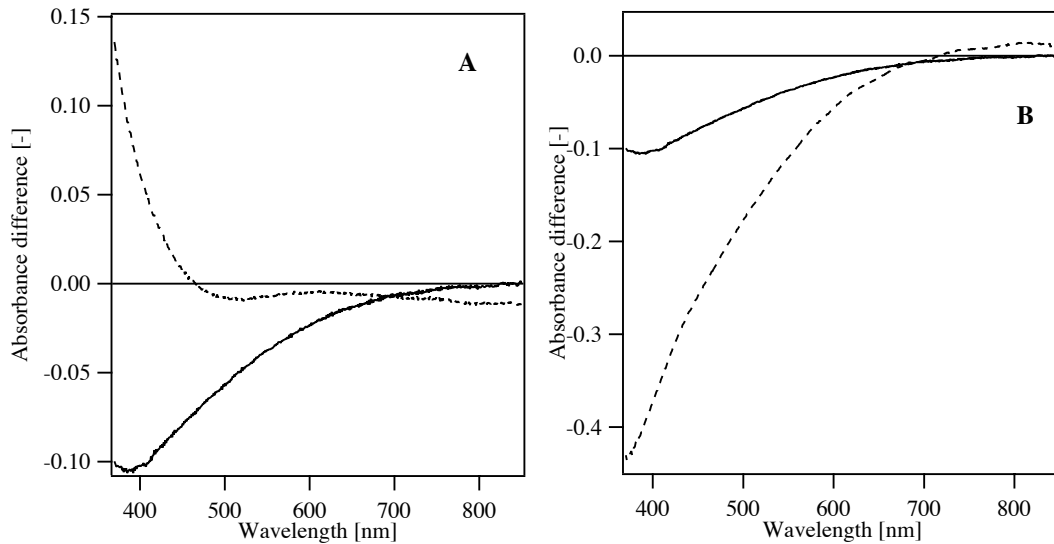where subscript "s" denotes the PbS/TiO_2 interface.

Figure 6.17: Absorbance difference spectra of PbS modified TiO_2 using CBD. The influence of the sintering atmosphere was tested (A) at a temperature of 150°C; in air (full line), and in argon (dashed line). The influence of sintering temperature in air (B) was examined; 150°C (dashed line), 200°C (full line).

The dependence on the temperature was shown to be negligible in argon; no significant absorption difference could be measured between samples heated at 150°C and 200°C. As shown on Figure 6.17 (B), in air the situation is different; the higher the temperature, the bigger the absorption loss. Differences denoted between 700 and 850 nm are due to the fact that different layers were used for these measurements. This optimisation showed that the HCl treatment leads to non-homogeneity and that the sintering has to be done under inert gas to avoid oxidation. The standard sintering temperature was set to 150°C.

VI.2.2   Nanosecond laser spectroscopy

As already shown for the other synthesis techniques, the nanosecond laser spectroscopy is used to monitor the reduction reaction of the hole-conductor, which can be assigned to the recombination between the hole present in the oxidised hole-conductor and an electron from the conduction band of the TiO_2.

The comparison between the recombination kinetics in a dip-coated sample and a sample prepared using CBD (in the following called CBD sample) is shown in Figure 6.18. From a general point of view, one can easily see that the recombination is much faster for the dip-coated sample than for the sample prepared using chemical bath deposition. The half-life time can roughly be estimated to be about 4 μs for dip-coating and 12 μs for chemical bath deposition. The slower recombination kinetics for the CBD sample are an indication of a better charge separation. As explained previously, the PbS layer on the surface of TiO_2, forms a blocking layer for the interfacial recombination. The direct contact between the oxidised hole-conductor and the electron-rich TiO_2 is hindered by the PbS layer. On the contrary, the fast recombination kinetics measured for the dip-coated sample, indicates that the TiO_2 can be in direct contact with the hole-conductor as PbS forms distinct particles on the TiO_2 surface.
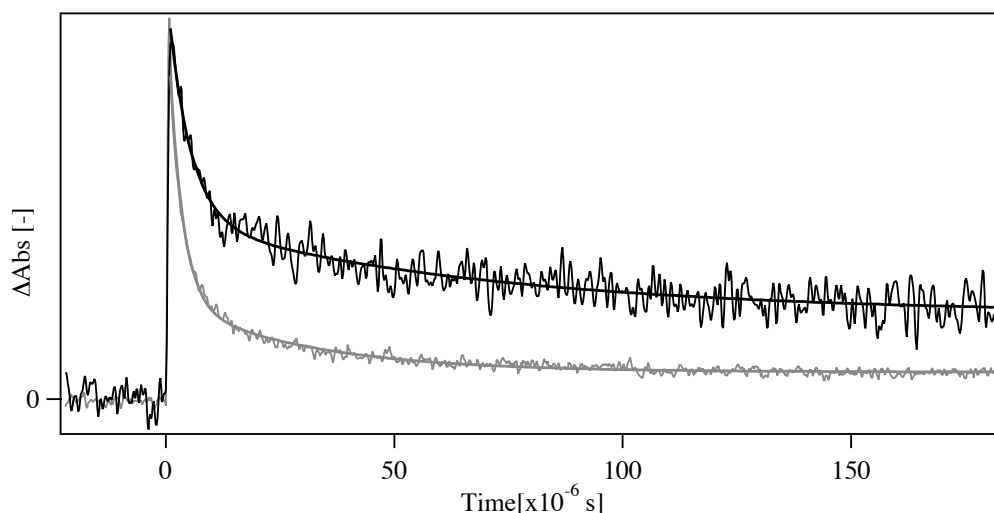

Figure 6.18: Transient absorption decay kinetics of the oxidised hole-conductor using different synthesis methods; chemical bath deposition (black lines) and dip-coating (grey lines). The spin coating solution for the deposition of the hole conductor contained 0.13 M in spiro-OMeTAD, 13 mM in $Li(CF_3SO_2)_2N$ and 0.4 mM in $N(p\text{-}C_6H_4Br)_3SBCl_6$.

Both decays were fitted by a double exponential, and the time constants are shown in Table 6.4. For the dip-coated sample the fast decay accounts for more than 80 % of the total decay. This proportion is less in the case of the CBD sample where it represents nearly 60 % of the decay. This difference may arise from electron trapping. Indeed deep-trapped electrons, not energetic enough to be injected into the TiO_2, may directly recombine with the oxidised hole-conductor molecules. This reaction would give rise to the slow decay portion.

	k1 [s^{-1}]	k2 [s^{-1}]
Dip-coated cell	$3.4*10^4 \pm 914$	$3.4*10^5 \pm 6.5*10^3$
CBD cell	$1.5*10^4 \pm 1.4*10^3$	$2*10^5 \pm 1.2*10^4$

Table 6.4: Double exponential time constants for a dip-coated sample and for a sample prepared using chemical bath deposition.

In the case of the chemical bath deposition technique, it was interesting to monitor the influence of some preparation parameters on the recombination time constants. As already shown before, changing the deposition time can vary the thickness of the PbS layer, and thus the absorption of the sample. The layer thickness could have an influence on the recombination probability between TiO_2 conduction band electrons and the oxidised hole-conductor, as the distance between both is varied. The recombination decay of samples with two different deposition times are shown in Figure 6.19.
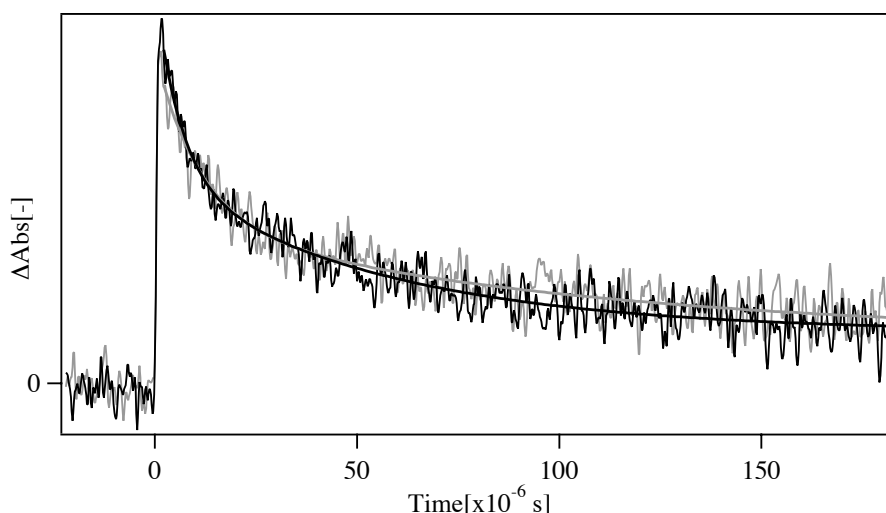

Figure 6.19: Transient absorption decay kinetics of the oxidised hole-conductor with different PbS deposition times; 15 min (grey lines) and 30 min (black lines). . The spin coating solution for the deposition of the hole conductor contained 0.13 M in spiro-OMeTAD, 13 mM in $Li(CF_3SO_2)_2N$ and 0.4 mM in $N(p-C_6H_4Br)_3SbCl_6$.

The two decays are nearly identical, showing no influence of the PbS thickness on the recombination rate. The intensities of the signals have not been normalised, so it is astonishing that the two measured signals have the same intensity. The optical absorption being different for the two samples at the exciting wavelength shows that the same amount of hole-conductor is oxidised during the measurement. As previously, the decays could be fitted with a double exponential, showing two possible recombination routes. The small difference between the two signals is certainly due to the experimental noise.

The concentration of the complexing agent in the deposition solution influenced the reaction rate. The higher the concentration, the slower the reaction. By varying the concentration, the absorption of samples having the same deposition time will vary. Figure 6.20 shows the influence of this parameter on the recombination kinetics.

No significant differences can be observed when comparing the decay kinetics of the sample prepared with different complexing agent concentration. This shows that the nature of the PbS layer does not influence the interfacial recombination. It has been shown[33,34] that the complex:Pb ratio can highly influences the particle size but only weakly the deposited layer thickness. As the distance between TiO_2 electrons and the oxidised hole-conductors stays constant, varying the complexing agent concentration does not influence the recombination kinetics.
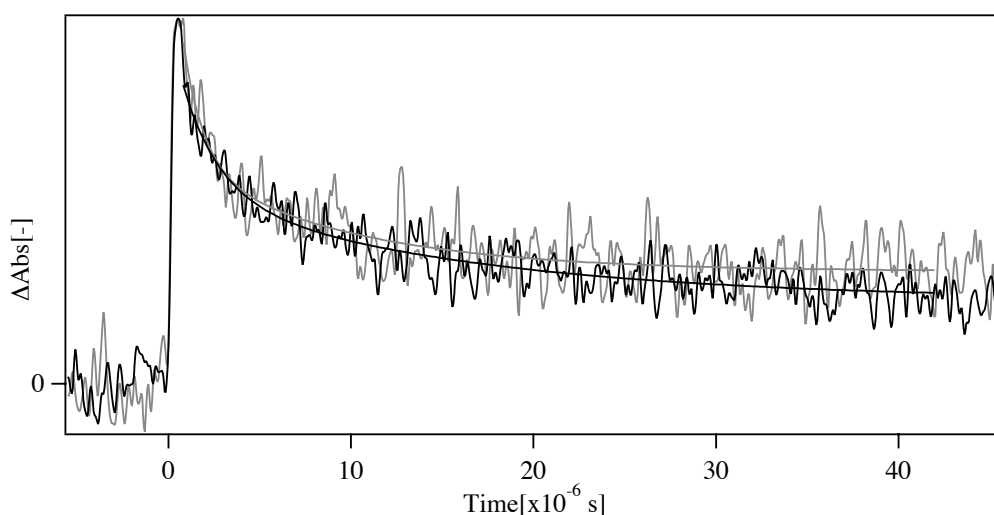

Figure 6.20: Transient absorption decay kinetics of the oxidised hole-conductor with different TEA concentration in the deposition solution; 0.02M TEA (black lines) and 0.04M TEA (grey lines). The spin coating solution for the deposition of the hole conductor contained 0.13 M in spiro-OMeTAD, 13 mM in $Li(CF_3SO_2)_2N$ and 0.4 mM in $N(p-C_6H_4Br)_3SBCl_6$.

VI.2.3   Photovoltaic measurements

The system optimisation has to take into account the photovoltaic response when varying parameters.

VI.2.3.1 Dip-coating versus Chemical Bath Deposition

The differences in current-voltage characteristics between a dip-coated electrode and a CBD electrode allows for many interesting observations. Table 6.5 reports the measured values.

	U_{OC} [mV]		I_{SC} [$\mu A/cm^2$]		FF [%]		η [%]	
	10 %	100 %	10 %	100 %	10 %	100 %	10 %	100 %
Dip-coating	388±2	455±2	123±8	1107±74	62±3	50±3	0.31±0.02	0.25±0.05
CBD	498±9	567±4	85±2	989±11	74±1	65±3	0.32±0.01	0.34±0.02

Table 6.5: Current-voltage measurements, of a 5 time dip-coated cell and a cell obtained using chemical bath deposition. The spin coating solution for the deposition of the hole conductor contained 0.13 M in spiro-OMeTAD, 13 mM in $Li(CF_3SO_2)_2N$ and 0.4 mM in $N(p-C_6H_4Br)_3SBCl_6$.

The first observation is about the U_{OC}. CBD cells reach much higher values (increase of more than 100 mV) than dip-coating cells. This difference confirms the supposition made at the beginning of this Section concerning the blocking effect of the PbS layer. The dip-coating technique was shown, in section 6.1, to form separated particles at the TiO_2 surface, contrarily to the CBD technique, which deposits a thin film as has been observed by Nair et al[35-37].This layer can hinder the interfacial recombination reaction. Figure 6.21 shows the measurements in the dark and at 10% Sun illumination.
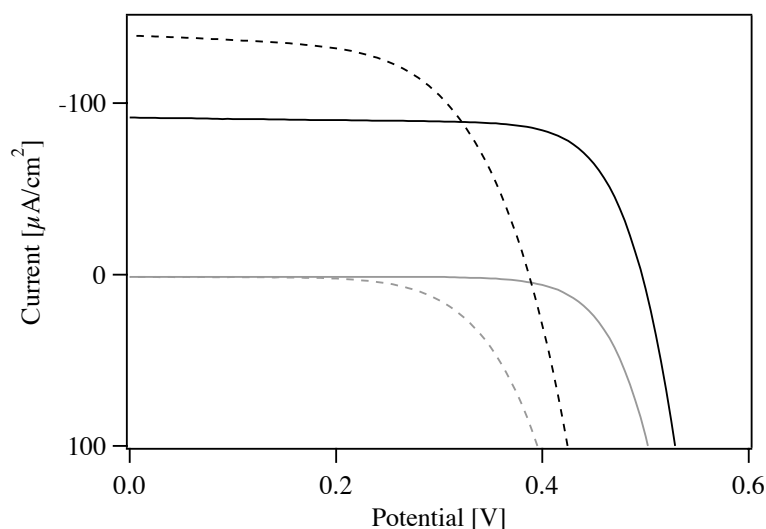
Figure 6.21: Current-voltage characteristics in the dark (grey lines) and at 10% Sun (10mW/cm^2) illumination (black lines) of dip-coated (dashed lines) and CBD deposited (full lines) PbS sensitised solid-state devices.

At low light intensity, the cell potential loss for the dip-coated sample is compensated by a higher I_{SC} than for the CBD sample, resulting in identical overall efficiencies. The performance of the CBD cells is linear with respect to the light intensity, which is not the case for the dip-coated cells. In section 6.1, it was shown that the efficiency of the dip-coated cells was always decreasing with increasing light intensity. This phenomenon can have several reasons; on one side the charge transport in the hole-conductor may be insufficient to regenerate the sensitiser, on the other side this phenomenon can arise due to recombination reactions. As more incident photons generate more injected electrons, the recombination between a conduction band electron and a hole-conductor molecule is more likely to happen. The I/V characteristics of dip-coated cells often denote low shunt resistance, especially at high illumination; as a consequence the fill factor of these cells is low. The CBD cells have similar efficiencies when varying the illumination from 10% to 100% Sun. The I_{SC} values are linearly depended of the light intensity, showing that the charge collection does not suffer from recombination enhancement. As PbS is covering the TiO$_2$, the contact between the hole-conductor and the TiO$_2$ is hindered, making the recombination more unlikely to happen.
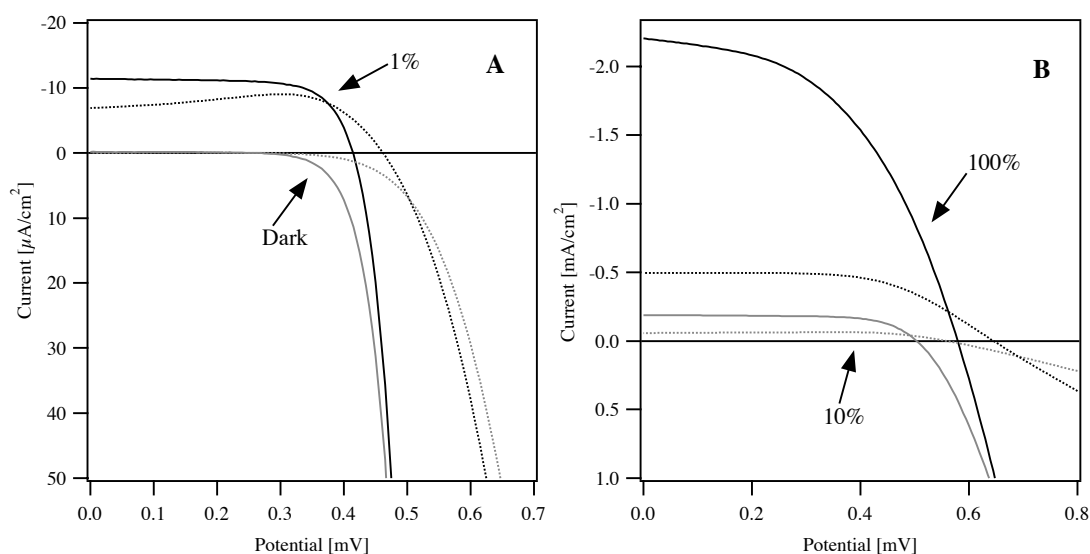
VI.2.3.2 Influence of tert-butylpyridine

Figure 6.22: Current-voltage measurements of devices prepared using CBD in dark (grey line on A) at an illumination intensity of 1% of Sun (black lines in A), of 10% Sun (grey lines on B), and 100% Sun (black lines in B) (corresponding to AM 1.5 $1 mW/cm^2$ $10 mW/m^2$ and $100 mW/cm^2$), without tBP (full lines) and with tBP 0.1M (dotted lines) in the hole-conductor matrix. The spin coating solution for the deposition of the hole conductor contained 0.13 M in spiro-OMeTAD, 13 mM in $Li(CF_3SO_2)_2N$ and 0.4 mM in $N(p-C_6H_4Br)_3SBCl_6$.

We saw previously that the addition of tBP into the hole-conductor matrix led to a strong decrease of the short-circuit current for dip-coated devices. As shown in Figure 6.22, this loss in I_{SC} is also measured in devices prepared with CBD, although the reduction is not as drastic as in devices prepared with dip-coating. The tBP is supposed to passivate the surface of TiO_2, increasing the Fermi level of the semiconductor. Due to the good PbS coverage of TiO_2 using CBD, the effect of tBP on the surface is hindered. The gain in U_{OC} by using tBP is about 50 mV depending on the light intensity. This is less than in the case of the dip-coated device. As the cell potential is determined by the difference between the Fermi level of the semiconductor and the redox potential of the hole-conductor, this results shows that the former is less influenced by tBP in the CBD devices.

VI.3   Conclusions

In this chapter three different types of PbS sensitisation were presented; dip-coating, PbS capping and chemical bath deposition. It was shown that using the dip-coating method, particles are synthesised in situ on the TiO_2. These particles were measured

to have a diameter of 5 nm using absorption spectroscopy confirmed by HRTEM pictures. The excited electron injection from PbS into TiO_2 was shown to occur using fluorescence spectroscopy. Once the electron is injected into the conduction band, one of the possible loss mechanism is the recombination with the oxidised hole-conductor. This reaction was monitored by nanosecond laser spectroscopy. Femtosecond laser measurements were used to monitor electron trapping in PbS, and injection of PbS trapped electrons into the conduction band of TiO_2. Photovoltaic characterisation determined that five dip-coatings were the optimum. Unfortunately the current-voltage measurement at full sun illumination exhibited large shunt resistances assigned to massive interfacial recombination.

It was shown that the capping of PbS using CdS and ZnS could significantly decrease the interfacial recombination, certainly due to a better coverage of the TiO_2 surface which hinders the direct contact between TiO_2 and hole-conductor. From the point of view of light conversion, the effects depended on the light intensity, but the overall conversion efficiency at full sun power illumination could not be increased with this method.

Chemical bath deposition was used to synthesise a PbS layer in situ on TiO_2. As dip-coating deposits distinct particles on TiO_2 it was thought that a better coverage could increase the cell efficiency. It turned out that the open circuit voltage was largely increased; unfortunately this was compensated by a decrease in short circuit current. The cells gave similar efficiencies to dip-coated ones. The increased U_{OC} was assigned to a reduced interfacial recombination using nanosecond laser spectroscopy, and the decrease of I_{SC} to poor pore-filling due to the formation of smaller pores.

VI.4   Bibliography

(1)   Vogel, R.; Hoyer, P.; Weller, H. *J. Phys. Chem.* **1994**, *98*, 3183.

(2)   Vogel, R.; Pohl, K.; Weller, H. *Chem. Phys. Lett.* **1990**, *174*, 241.

(3)   Patel, A. A.; Wu, F.; Zhang, J. Z.; Torres-Martinez, C. L.; Mehra, R. K.; Yang, Y.; Risbud, S. H. *J. Phys. Chem. B* **2000**, *104*, 11598.

(4)   Lifshitz, E.; Sirota, M.; Porteanu, H. *J. Cryst. Growth* **1999**, *196*, 126.

(5)   Huang, W.; Shi, J. *J. Mater. Res.* **2000**, *15*, 2343.

(6)   Wang, Y.; Suna, A.; Mahler, W.; Kasowski, R. *J. Chem. Phys.* **1987**, *87*, 7315.

(7)   Chen, S.; Truax, L. A.; Sommers, J. M. *Chem Mater.* **2000**, *12*, 3864.

(8)   Krueger, J. Interface engineering in solid-state dye-sensitized solar cells, EPFL, 2003.

(9)   Evans, J. E.; Springer, K. W.; Zhang, J. Z. *J. Chem. Phys.* **1994**, *101*, 6222.

(10)   Nozik, A. J. *Annu. Rev. Phys. Chem.* **2001**, *52*, 193.

(11)   Diol, S. J.; Miller, C. C.; Schmuttenmaer, C. A.; Cao, J.; Gao, Y.; Miller, R. J. D. *J. Phys. D: Appl. Phys.* **1997**, *30*, 1427.

(12)   Pelet, S. Femtosecond dynamics of electron transfer in the photsensitisation of wide band gap semiconductor, EPFL, 2002.

(13)   Bach, U.; Tachibana, Y.; Moser, J.-E.; Haque, S. A.; Klug, D. R.; Grätzel, M.; Durrant, J. R. *J. Am. Chem. Soc.* **1999**, *121*, 7445.

(14)   Peter, L. M.; Wijayantha, K. G. U.; Riley, D. J.; Waggett, J. P. *J. Phys. Chem. B* **2003**, *107*, 8378.

(15)   Hong, J. S.; Choi, D. S.; Kang, M. G.; Kim, D.; Kim, K.-J. *Journal of Photochemistry and Photobiology A: Chemistry* **2001**, *143*, 87.

(16)   Yang, S.-m.; Huang, C.-h.; Zhai, J.; Wang, Z.-s.; Jiang, L. *Journal of materials chemistry* **2002**, *12*, 1459.

(17)   Rincon, M. E.; Gomez-Daza, O.; Corripio, C.; Orihuela, A. *Thin Solid Films* **2001**, *389*, 91.

(18)   Nazeeruddin, M. K.; Kay, A.; Rodicio, I.; Humphry-Baker, R.; Müller, E.; Liska, P.; Vlachopoulos, N.; Grätzel, M. *J. Am. Chem. Soc.* **1993**, *115*, 6382.

(19)   Huang, S. Y.; Schlichtörl, G.; Nozik, A. J.; Grätzel, M.; Frank, A. J. *J. Phys. Chem. B* **1997**, *101*, 2576.

(20)   Moser, J.; Punchihewa, S.; Infelta, P. P.; Grätzel, M. *Langmuir* **1991**, *7*, 3012.

(21)   Weller, H. *Angew. Chem. Int. Ed. Engl.* **1993**, *32*, 41.

(22)   Yang, S.-m.; Wang, Z.-s.; Huang, C.-h. *Synthetic Metals* **2001**, *123*, 267.

(23)   Hines, M. A.; Guyot-Sionnest, P. *J. Phys. Chem.* **1996**, *100*, 468.

(24)   Fernée, M. J.; Watt, A.; Warner, J.; Cooper, S.; Heckenberg, N.; Rubinsztein-Dunlop, H. *Nanotechnology* **2003**, *14*, 991.

(25)   Dabbousi, B. O.; Rodriguez-Viejo, J.; Mikulec, F. V.; Heine, J. R.; Mattoussi, H.; Ober, R.; Jensen, K. F.; Bawendi, M. G. *J. Phys. Chem. B* **1997**, *101*, 9463.

(26)   Peng, X.; Schlamp, M. C.; Kadavanich, A. V.; Alivisatos, A. P. *J. Am. Chem. Soc.* **1997**, *119*, 7019.

(27)   Haubold, S.; Haase, M.; Kornowski, A.; Weller, H. *ChemPhysChem* **2001**, *5*,
        331.

(28)   Qi, L.; Ma, J.; Cheng, H.; Zhao, Z. *Colloids and Surfaces A: Physicochemical
        and Engineering Aspects* **1996**, *111*, 195.

(29)   Wageh, S.; Ling, Z. S.; Xu-Rong, X. *Journal of Crystal Growth* **2003**, *255*,
        332.

(30)   Zhang, X.-t.; Sutanto, I.; Taguchi, T.; Tokuhiro, K.; Meng, Q.-b.; Rao, T. N.;
        Fujishima, A.; Watanabe, H.; Nakamori, T.; Uragami, M. *Solar energy
        materials and solar cells* **2003**, *80*, 315.

(31)   Kay, A.; Grätzel, M. *Chem Mater.* **2002**, *14*, 2930.

(32)   Kumara, G. R. R. A.; Tennakone, K.; Perera, V. P. S.; Konno, A.; Kaneko, S.;
        Okuya, M. *J. Phys. D: Appl. Phys.* **2001**, *34*, 868.

(33)   Gorer, S.; Albu-Yaron, A.; Hodes, G. *Chem. Mater.* **1995**, *7*, 1243.

(34)   Gorer, S.; Albu-Yaron, A.; Hodes, G. *Journal of Physical Chemistry* **1995**, *99*,
        16442.

(35)   Suarez, R.; Nair, P. K. *Journal of solid state chemistry* **1996**, *123*, 296.

(36)   Nair, P. K.; Nair, M. T. S.; Garcia, V. M.; Arenas, O. L.; Pena, Y.; Castillo,
        A.; Ayala, I. T.; Gomezdaza, O.; Sanchez, A.; Campos, J.; Hu, H.; Suarez, R.;
        Rincon, M. E. *Solar Energy Materials and Solar Cells* **1998**, *52*, 313.

(37)   Nair, P. K.; Ocampo, M.; Fernandez, A.; Nair, M. T. S. *Solar Energy
        Materials* **1990**, *20*, 235.

Chapter VII

The Metal Selenide Sensitisation

Metal selenides have already been largely investigated and used in a large variety of applications. PbSe has found applications in IR detectors, photographic plates, photovoltaic absorbers[1,2] and so forth. CdSe has been used as photoconducting device owing to its high photosensitivity. These materials can be obtained in thin film form by evaporation, sputtering, pyrolysis and chemical bath deposition techniques (CBD). Of all these techniques, CBD is relatively inexpensive, simple, and convenient for large area deposition of II-VI and IV-VI compounds. Already known in the 1960's[3], this technique allows film deposition on a variety of substrates (insulators, semiconductors and metals).

The first systematic study of the influence of deposition parameters was published by R.C. Kainthla et al.[4]. But until 1981, no size quantization was reported on CBD films. Such effects were published for the first time by Papavassilou[5] who found blue shifts in the photoluminescence spectra of CdS films. In the present work, metal selenides were deposited using a method developed by Gary Hodes and his co-workers[6-9]. The selenides are very interesting for sensitisation due to their broad absorption spectrum covering a large part of the visible range. The work of Hodes et al. showed that the absorption edge is easily tuned by changing the experimental conditions. Lead selenide (PbSe) and cadmium selenide (CdSe) were investigated during this work, but in less detail than metal sulfides, mainly because of a lower overall efficiency of the obtained devices.

VII.1   Absorption spectroscopy

As shown previously[9], the absorption features of PbSe and CdSe can easily be tuned by varying the experimental conditions, such as reaction temperature, nature of the complexing agent, or complexing agent concentration. Figure 7.1 shows the absorption spectra of CdSe sensitised TiO_2 layers under various conditions.
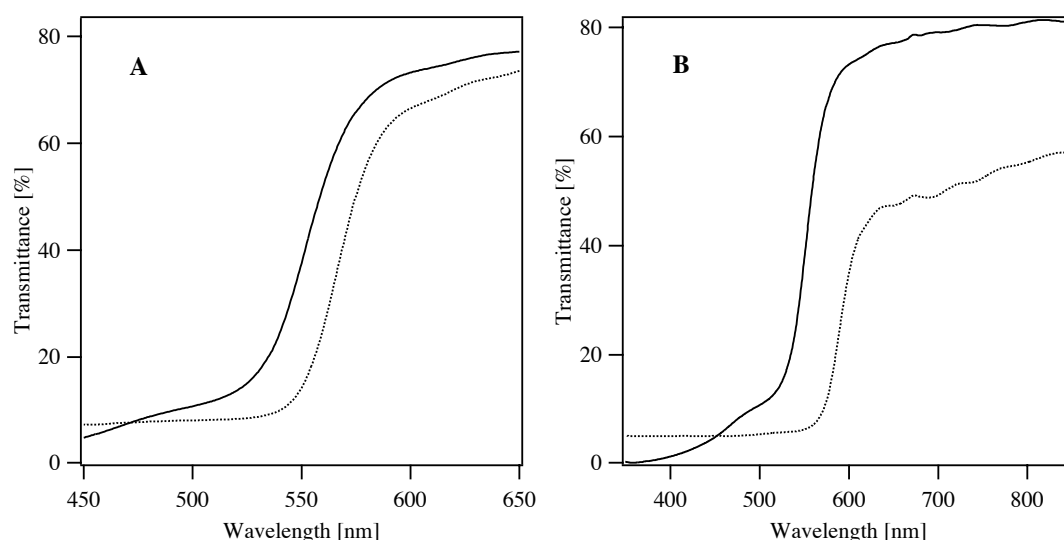

Figure 7.1: Transmittance spectra of CdSe sensitised TiO_2 (3μm) using chemical bath deposition technique, using nitrilotriacetic acid (NTA) as complexing agent. (A) shows the influence of the concentration of NTA; ratio $[NTA]/[Cd^{2+}]= 1.47$ (full line), and ratio $[NTA]/[Cd^{2+}]= 2.1$ (dotted line). (B) shows the influence of the reaction temperature; 20°C (full line), 40°C (dotted line).

The absorption edge of CdSe is very abrupt, showing that the synthesis produces a narrow size distribution of particles. As already discussed in Chapter 5, there exists a critical complexing agent to metal ratio (R_C), which indicates a change in the chemical bath deposition mechanism. For a ratio larger than R_C the ion-by-ion mechanism is predominant, but when the ratio is smaller than R_C due to the presence of $Cd(OH)_2$ in the solution, the bulk precipitation is the major mechanism. The ratio used in this work bracketed each side of R_C, using published values[8]. The red shift for a higher ratio can clearly be observed, indicating bigger particle size. The shift measured in this experiment is small (0.02 eV) comparing to known values (0.1-0.2 eV). This could arise from the fact that in this work the substrate is nanocrystalline. To reach efficient optical absorption, only short deposition times are necessary due to the high effective surface area. As the particle size is dependent of the deposition duration, the particle size is reduced. This is confirmed by comparing these absorption

edges with those found in previous studies, a blue shift of 50-60 nm can be noticed for the spectra of this work.

The effect of reaction temperature on the absorption spectra is strong. For the same complexing agent to metal ratio the spectrum is shifted towards the red (about 40 nm) when passing from a temperature of 20°C to 40°C. A linear dependence of the optical band-gap, estimated from optical transmission spectra, as a function of deposition temperature was found[10]. It was shown that R_C varies with the temperature. As the equilibrium constants of the complex and the solubility product of $Cd(OH)_2$ varies with the temperature, the critical ratio will also depend on the temperature.

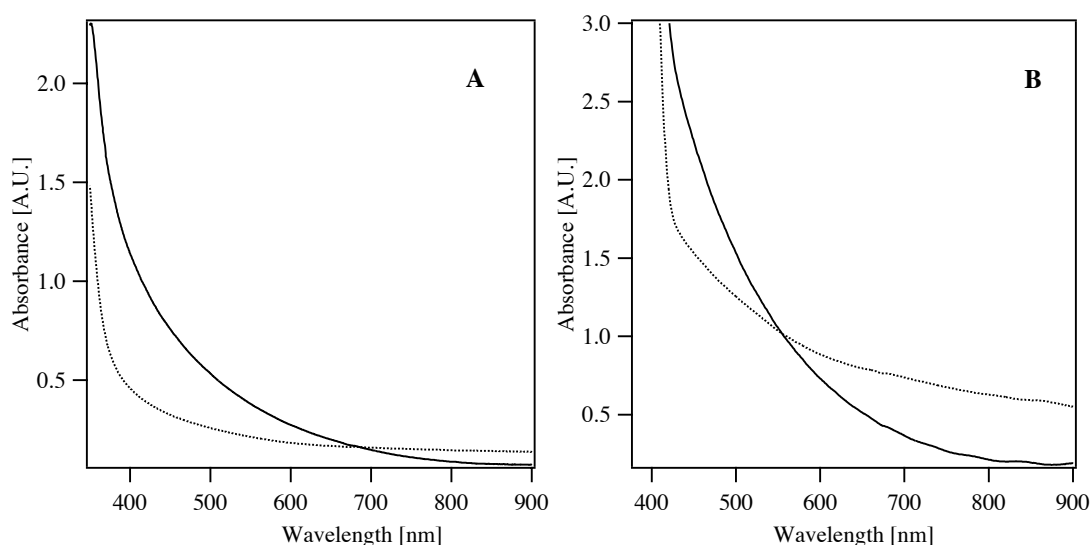The absorption behaviour for different experimental conditions of PbSe is shown on Figure 7.2.

Figure 7.2: Absorption spectra PbSe sensitised TiO_2 nanocrystalline layer. (A) shows the influence of the reaction temperature; 0°C (dotted line) and 20°C (full line). (B) shows the influence of the deposition time; 15 min (full line) and 45 min (dotted line).

The absorption spectra of PbSe do not exhibit an abrupt band edge as in the case of CdSe, a larger particle size distribution is causing this effect. It is difficult to compare the obtained spectra with those found in the literature[6,7]; the substrates used in the literature are not porous as in this work. For flat substrates the deposition time was typically several hours, but could range from tens of minutes to days depending on the conditions[9]. The obtained films were 20-100 nm thick. In this work, the substrates have been treated less than one hour, resulting in much thinner films.

As already shown for CdSe the temperature plays an important role in the deposition mechanism, and thus in the deposition rate. In Figure 7.2 A, it can be seen that the

higher the deposition temperature, the higher the absorption of the processed layer. Figure 7.2 B compares deposition times of 15 min and 45 min. It can be seen than during the deposition the particles are growing; the absorption edge has moved to higher wavelength. This observation was made by Gorer et al.[7] as for a thicker film the particle size increased.

VII.2   Fluorescence spectroscopy

Fluorescence has already often been reported for PbSe and CdSe. Due to its very small band gap (0.28 eV), bulk PbSe has a fluorescence situated in the infrared. Although strong confinement is easily achieved in relatively large particles due to the large exciton Bohr radius (46 nm), which displaces the luminescence to the near-infrared[11] or even into the visible region[12]. CdSe has a bulk band gap of 1.74 eV[13]. Consequently, the luminescence of this material is observed around 730 nm[14].

In the present experiments the CdSe photoluminescence could be observed by exciting the samples with 520 nm laser light. The CdSe deposited on different semiconductors showed luminescence on Al_2O_3 and on ZrO_2, but this phenomenon was largely quenched when the particles were deposited on TiO_2. This quenching observation suggests the possible electron injection from the excited CdSe into the TiO_2.
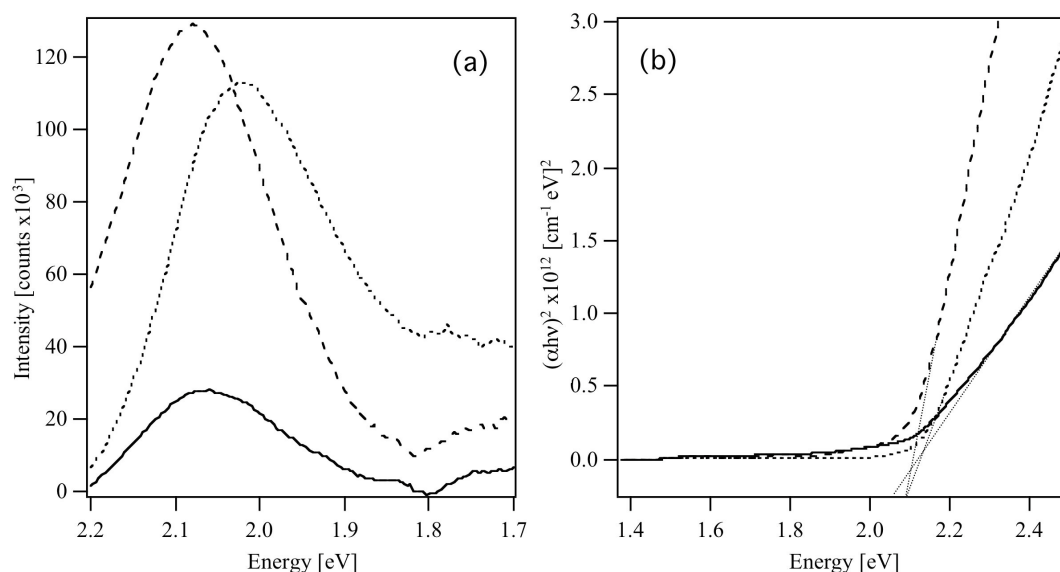
Figure 7.3: (a) Fluorescence spectra of semiconductor layers sensitised with CdSe nanoparticles: deposition on TiO_2 (full line), ZrO_2 (dashed line), and Al_2O_3 (dotted line). The samples were excited using a Kr laser at 520 nm and 0.1 W. (b) Plots of $(\alpha h\nu)^2$ vs $h\nu$ for CdSe sensitised semiconductors: TiO_2 (full line), ZrO_2 (dashed line), and Al_2O_3 (dotted line).

Although quenching occurs on TiO_2 the emission peak has not completely disappeared, showing incomplete electron injection into the semiconductor. In Figure 7.3a one can observe that the luminescence peak is slightly shifted towards lower energies when depositing CdSe on Al_2O_3. This might arise from the fact that a small part of the excited electron energy is lost through non-radiative pathways before fluorescence occurs. One could also argue that the shift occurs from a difference in particle size. This explanation was refuted by plotting $(\alpha h\nu)^2$ versus $h\nu$, shown on Figure 7.3b. This plot allows the determination of the band gap of the CdSe particles, by extrapolating the linear part of the curve to the x axis. The extrapolation of the plots for the three oxides gives a band gap for the CdSe nanoparticles of 2.1 eV

Fluorescence of PbSe could unfortunately not be observed on any of the semiconductors. The reason for this may be that the peak was hidden by the second order generation of the grating of the fluorometer. The electron injection into TiO_2 from PbSe could therefore not be monitored using this technique. Injection will be shown to occur using nanosecond laser spectroscopy and photovoltaic measurements.

VII.3   Nanosecond laser spectroscopy

As before, nanosecond laser spectroscopy was used to monitor the recombination of the reduced hole-conductor and the TiO_2 injected electron. The electron injection from PbSe into TiO_2 could not be shown using fluorescence spectroscopy. Consequently, nanosecond spectroscopy will be used to monitor the regeneration of the oxidised hole-conductor, proving the possibility to inject excited electrons from the PbSe into TiO_2.

The kinetics measured for PbSe and CdSe sensitised systems are shown in Figure 7.4. It can be seen that the recombination in such systems is much slower than for PbS. The thickness of the deposited layer certainly plays an important role in the blocking behaviour, and might not be constant in the three cases. The decay kinetics are fitted by a double exponential function, the time constants are shown in Table 7.1. A very fast decay is followed by a very long lasting decay. The fast time constant is almost identical for PbSe and CdSe (1.4 μs) and accounts for roughly the half of the decay. In the case of PbS the fast time constant is about 0.7 μs and represents approximately 80 % of the decay. The slower decay arises from the fact that the excitation energy was able to excite more than one nanoparticle per TiO_2 particle due to the high power of the laser.
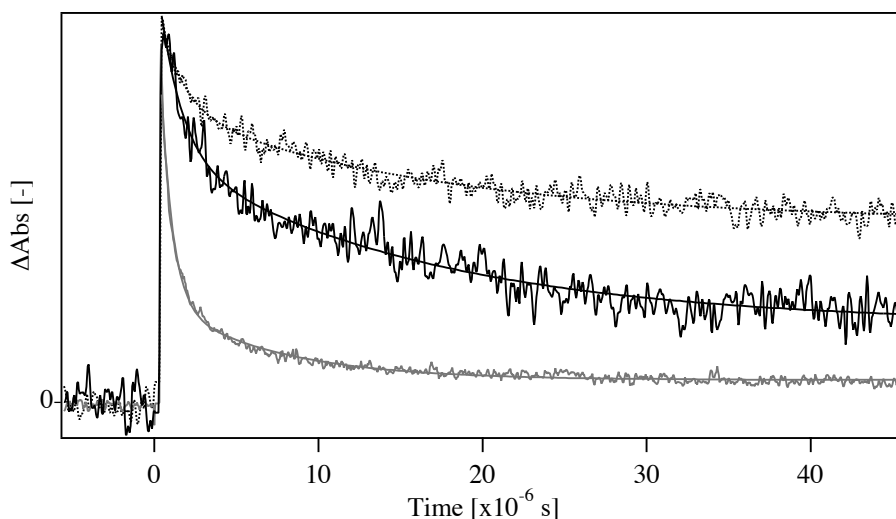

Figure 7.4: Transient absorption decay kinetics of the oxidised hole-conductor with PbSe (black line), CdSe (dotted line), and PbS deposited by CBD (grey line). The spin coating solution for the deposition of the hole conductor contained 0.13 M in spiro-OMeTAD, 13 mM in $Li(CF_3SO_2)_2N$ and 0.4 mM in $N(p-C_6H_4Br)_3SBCl_6$.

	k_{r1} [s^{-1}]	k_{r2} [s^{-1}]
CdSe	$6.3*10^4 \pm 3.4*10^3$ (50%)	$7.1*10^5 \pm 6.3*10^4$ (50%)
PbSe	$6.3*10^4 \pm 3.6*10^3$ (47%)	$7.3*10^5 \pm 6.2*10^4$ (53%)
PbS	$1.5*10^5 \pm 3.5*10^3$ (17%)	$1.4*10^6 \pm 2.9*10^4$ (83%)

Table 7.1: Double exponential time constant for CdSe, PbSe and PbS coated TiO$_2$ electrodes.

VII.4 Photovoltaic measurements

The photovoltaic measurements showed that CdSe or PbSe sensitised solid-state cells have a photovoltaic activity when exposed to sunlight. The obtained IPCE spectra are shown in Figure 7.5 and the current-voltage measurements are summarised in Table 7.1.

For both sensitisers, the measured IPCE values are quite low when compared with values obtained for PbS sensitisation, but still exhibit the characteristic shape of the absorption spectra. These low values certainly arise from an injection problem, the energy level of the excited electron lying too near or below the energy level of the TiO$_2$ conduction band. Similar work using CdSe sensitisation of TiO$_2$ but using liquid electrolytes achieved a maximum IPCE of 3% at 500nm[1].
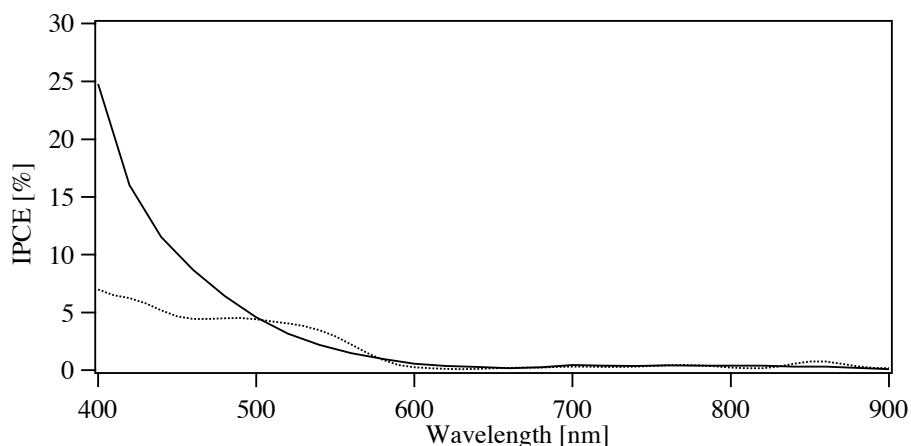
Figure 7.5: IPCE spectra of PbSe (full line) and CdSe (dotted line) sensitised solid-state device. The spin coating solution for the deposition of the hole conductor contained 0.25 M in spiro-OMeTAD, 13 mM in Li(CF$_3$SO$_2$)$_2$N and 0.4 mM in N(p-C$_6$H$_4$Br)$_3$SBCl$_6$.

It was explained above that the size of the particles in the layer could easily be tuned by varying the experimental conditions; larger particles having absorption edges at longer wavelengths. But the larger the particles are, the weaker is the quantum size

effect. Therefore, larger particles cannot be used to achieve broader IPCE spectra. The energetic level of the CdSe CB will lie below the TiO_2 CB. On the other hand, using smaller particles could lead to a better injection, but their absorption will be shifted towards blue wavelengths, i.e. a poor overlap of the visible spectrum.

	U_{OC} [mV]		I_{SC} [μA/cm^2]		FF [%]		η [%]	
	10 %	100 %	10 %	100 %	10 %	100 %	10 %	100 %
CdSe	455±22	508±21	5±0.1	37±1	65±1	71±1	0.02	0.01
PbSe	453±6	528±5	48±0.5	488±3	69±1	58±2	0.16	0.15

Table 7.2: Photovoltaic performance of PbSe and CdSe sensitised solid-state solar cell at 10 % and 100 % Sun illumination (AM 1.5)

From the values shown in Table 7.2, one can see that the open-circuit potential of the metal selenide sensitised devices are very similar to those found for the sensitisation using CBD PbS (440 mV @ 10 % Sun, 510 mV @ 100% Sun). The same deposition method has been used, forming a layer at the surface of the TiO_2. As already discussed in the case of PbS, this layer certainly acts as a blocking layer and inhibits the interfacial recombination, leading to a high device voltage.

Unfortunately the short-circuit current of these devices is very low, as already seen on the IPCE spectra, especially for CdSe sensitised devices. This problem arises from the poor energy level positioning. The excited electrons cannot inject into the TiO_2 because its energy is not high enough.

Very few comparable studies have been found in the literature. For as-deposited CdSe films on conducting glass and immersed in a polysulphide electrolyte, respectable photovoltaic characteristics have been found (I_{SC} ~ 1 mA/cm^2 and V_{OC} ~ 0.4 V)[10]. Rincon et al.[1,15] used spray-painted TiO_2 on which a CdSe layer was deposited by chemical bath deposition. After sintering at 400°C in air for one hour, the photovoltaic performance was impressive using the polysulfide electrolyte; I_{SC} ~ 5 mA/cm^2, V_{OC} ~ 0.48 V, η = 1.2% @ 100 mW/cm^2. Such a sintering procedure was also used in the present work, leading to the discoloration of the samples, i.e. destruction of the CdSe layer. At a lower sintering temperature no beneficial effect on the cell performance could be shown. Gorer et al.[9] reported photoelectrochemical

activity of PbSe layers deposited on conducting glass. The measured quantum efficiencies were one order of magnitude lower than corresponding CdSe ones, indicating heavy recombination. They also demonstrated the influence of the crystal size and size distribution on the spectral response of the photocurrent.

VII.5   Conclusions

This study of metal selenide sensitised solid-state system showed that the chemical bath deposited layer can be used for light energy conversion in such devices.

The somewhat weak photovoltaic performance might be explained by a bad fitting of the energy levels between the sensitiser and the hole-conductor. It could therefore be interesting to try an optimisation by using nanocrystalline SnO_2 which has a lower conduction band than TiO_2.

VII.6   Bibliography

(1)   Rincon, M. E.; Gomez-Daza, O.; Corripio, C.; Orihuela, A. *Thin Solid Films* **2001**, *389*, 91.

(2)   Rincon, M. E.; Sanchez, M.; Olea, A.; Ayala, I.; Nair, P. K. *Solar energy materials and solar cells* **1998**, *52*, 399.

(3)   Chopra, K. L. Thin Film Phenomena; Co, M.-H. B., Ed. new-York, 1969.

(4)   Kainthla, R. C.; Pandya, D. K.; Chopra, K. L. *J. Electrochem. Soc.* **1980**, *127*, 277.

(5)   Papavassiliou, G. C. *Journal of Solid State Chemistry* **1981**, *40*, 330.

(6)   Gorer, S.; Albuyaron, A.; Hodes, G. *Journal of Physical Chemistry* **1995**, *99*, 16442.

(7)   Gorer, S.; Albu-Yaron, A.; Hodes, G. *Chem. Mater.* **1995**, *7*, 1243.

(8)   Gorer, S.; Hodes, G. *Journal of Physical Chemistry* **1994**, *98*, 5338.

(9)   Gorer, S.; Hodes, G. *Studies in Surface Science and catalysis* **1996**, *103*, 297.

(10)   Hodes, G. *Israel Journal of Chemistry* **1993**, *33*, 95.

(11)   Du, H.; Chen, C. L.; Krishnan, R.; Krauss, T. D.; Harbold, J. M.; Wise, F. W.; Thomas, M. G.; Silcox, J. *Nano Letters* **2002**, *2*, 1321.

(12)   Guha, S.; Leppert, V. J.; Risbud, S. H.; Kang, I. *Solid state communications* **1998**, *105*, 695.

(13)   Woggon, U. Optical properties of semiconductor quantum dots. In *Springer Tracts in Modern Physics*; Springer, Ed. Berlin, 1997; Vol. 136.

(14)   Wang, W. Z.; Geng, Y.; Yan, P.; Liu, F. Y.; Xie, Y.; Qian, Y. T. *Journal of the American Chemical Society* **1999**, *121*, 4062.

(15)   Rincon, M. E.; Jimenez, A.; Orihuela, A.; Martinez, G. *Solar energy materials and solar cells* **2001**, *70*, 163.

Chapter VIII

Interface Optimisation

The interface where the charge separation occurs in a solar cell is certainly the most striking part of the whole device. The charge separation is the fundamental phenomenon for the "production" of electrons, and thus the building-up of an electrical current. For every type of solar energy converter a lot of work has been focused on the optimisation of this interface. On one hand the separation mechanism was investigated to minimise the losses due to direct recombination of the electron-hole pair after excitation (K_{des} on Figure 8.1). In the dye-sensitised cell, this separation is very efficient due to ultra-fast electron injection from the sensitiser to the semiconductor (K_{inj} on Figure 8.1). This separation generates a charge on each side of the interface. On the other hand, the interfacial charge recombination was intensively studied, as it appeared that it was leading to high losses. In the dye-sensitised solar cell, due to the mesoporous network the distance between the electron and the holes is rather small. Even more in the solid-state device, where no liquid electrolyte is present, and thus less charge screening occurs in this system. Several recombination routes can be pointed out.

The recombination of the injected electron with the oxidised sensitiser (K_{rec2} on Figure 8.1) before the regeneration of the sensitiser (K_{reg} on Figure 8.1), has been studied for the organo-metallic dyes[1,2]. This process was shown to be very slow (in the *ms* time range), demonstrating that the short-circuit potential will not suffer from this recombination. It is supposed that the process is similar when replacing the dye by semiconductor nanoparticles. The electrons already collected in the conducting

SnO_2 layer may recombine with the oxidised hole-conductor. To prevent this reaction, a compact TiO_2 layer has been deposited between the conducting glass and the nanocrystalline TiO_2 (see Chapter 3). This blocking layer is very effective rendering this pathway negligible.
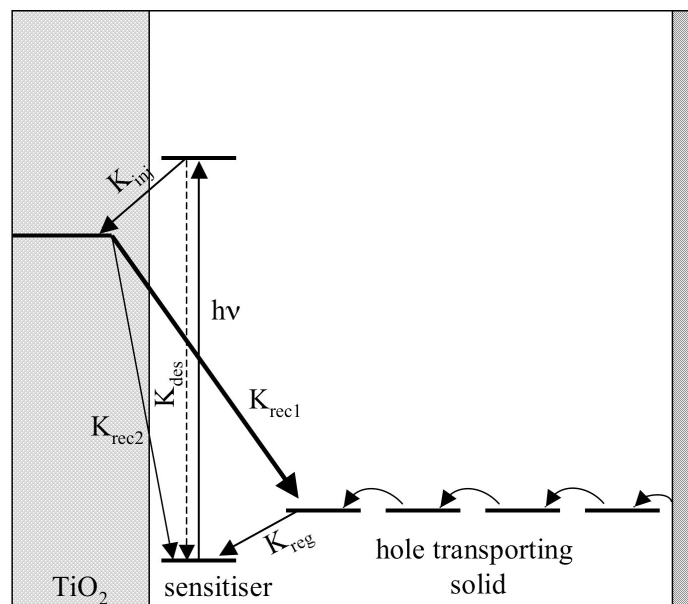

Figure 8.1: Different possible recombination routes in the solid-state nanocrystalline solar cell

The major recombination process occurs between the injected electron in the TiO_2 and the oxidised hole-conductor (K_{rec1} on Figure 8.1), the exciton recombination inside the particle being inhibited by the electron injection. This reaction leads to an enhancement of the dark current, i.e. a diminution of the voltage of the cell. As already discussed in the Chapter 6, this recombination happens due to the electron trapping in the surface states. The nanocrystalline TiO_2 used in the dye-sensitised solar cells has a large surface area, thus a large quantity of these states are present at the junction between TiO_2 and electrolyte or hole-conductor. To have a quantitative measurement of the occupancy of the surfaces states one uses the energy level of the Fermi level.

Several strategies have been used to inhibit the interfacial recombination. The use in the solid-state device of an interfacial dipole layer has been studied using a series of benzoic acids with different dipole moments[3]. The dipole field is supposed to change the difference in the work function of the neighbouring materials. As a consequence,

the barrier for charge transfer can be increased, and thus the dark current can be suppressed. The nanosecond laser measurements showed a drastic diminution of the recombination rate, but current-voltage characteristics showed high series resistance, leading to low device efficiencies.

As shown in Chapter 6, the deposition of a thin semiconductor layer covering the TiO_2 can increase the efficiency by preventing a contact between the oxidised hole-conductor and the TiO_2. For example, ZnO[4], Al_2O_3[5], Y_2O_3[6]and more recently $SrTiO_3$[7] have been used in this sense to increase the photovoltaic device performances. However, in the SSD no significant improvement could be made by this approach.

It was also shown that an effective charge screening can be obtained by adding to the hole-conductor solution Li^+ ions[8]. Under illumination, a positive space charge is formed in the hole-conductor matrix, inducing a local field and hindering the current flow. The lithium was shown to screen the field, and thus to eliminate the influence of the space charge on the photocurrent.

As discussed in Chapter 6, the use of tBP increases the performance of the dye-sensitised device by passivating the surface of TiO_2, i.e. filling up the surface states, shifting to higher energies the Fermi level of the semi-conductor. It was shown and discussed, in Chapter 6, that this strategy does not work for the nanoparticle sensitised solid-state system.

As the above mentioned strategies had no beneficial effect on the SSD and more precisely on nanoparticle sensitised solid-state devices, an alternative way to improve the performance of this type of cells has to be found. An effect similar to tBP is required to passivate the surface states in order to hinder the recombination. Screening different types of bases has already been tried[9] without success for the dye-sensitised system. However, long chain alkyls have been used to passivate the surface of some semiconductors like SiO_2[10,11]. More recently, similar compounds have been used to increase the photoresponse of dye-sensitised solar cells. These compounds were alkyls with at least one phosphonic or carboxylic group; 1-decylphosphonic acid (DPA)[12], hexadacylmalonic acid (HDMA)[13] or 3-phenylpropionic acid[14] .The phosphonic or carboxylic groups are necessary for efficient adsorption at the surface, and the long alkyl chain increases the distance between the surface and the electrolyte. The influence of theses molecules on quasi-solid devices[15,16] was studied. All these compounds enhanced the short-circuit current, but the open-circuit voltage was only increased with HDMA. It is supposed that the alkyl chains form with

ruthenium dyes, containing two long alkyl chains, a compact layer that decreases the back electron transfer rate from TiO_2 to the triiodide in electrolytes. It was also shown that photoanodes based on TiO_2 sensitised by an amphiphilic dye and these types of coadsorbers maintain stable performance under thermal stress and long-term light illumination.

It was thought that these compounds might also help to increase the photoactivity of the nanoparticle sensitised solid-state device, by blocking the back reaction of the injected electron. Several molecules, shown in Figure 8.2, have been tested and their influence on dip-coated and CBD sensitised electrodes has been studied using nanosecond laser measurement, Fourier transform infrared spectroscopy (FTIR), and photovoltaic characterisation.
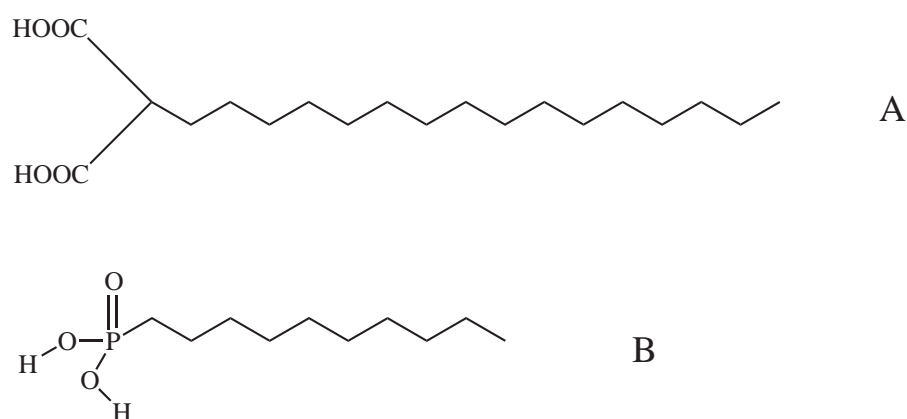

Figure 8.2: Molecules used for the surface modification; (A) hexadecylmalonic acid (HDMA), (B) 1-decylphosphonic acid (DPA)

VIII.1 Nanosecond laser spectroscopy

Laser spectroscopy was used to monitor the effect of the co-deposited molecules on the interfacial recombination kinetics. It was supposed that these molecules are able to block the back electron transfer by forming a compact layer between TiO_2 and the hole-conductor.

The measurements have been done on dip-coated samples and on CBD deposited ones. The obtained decays are shown in Figure 8.3.
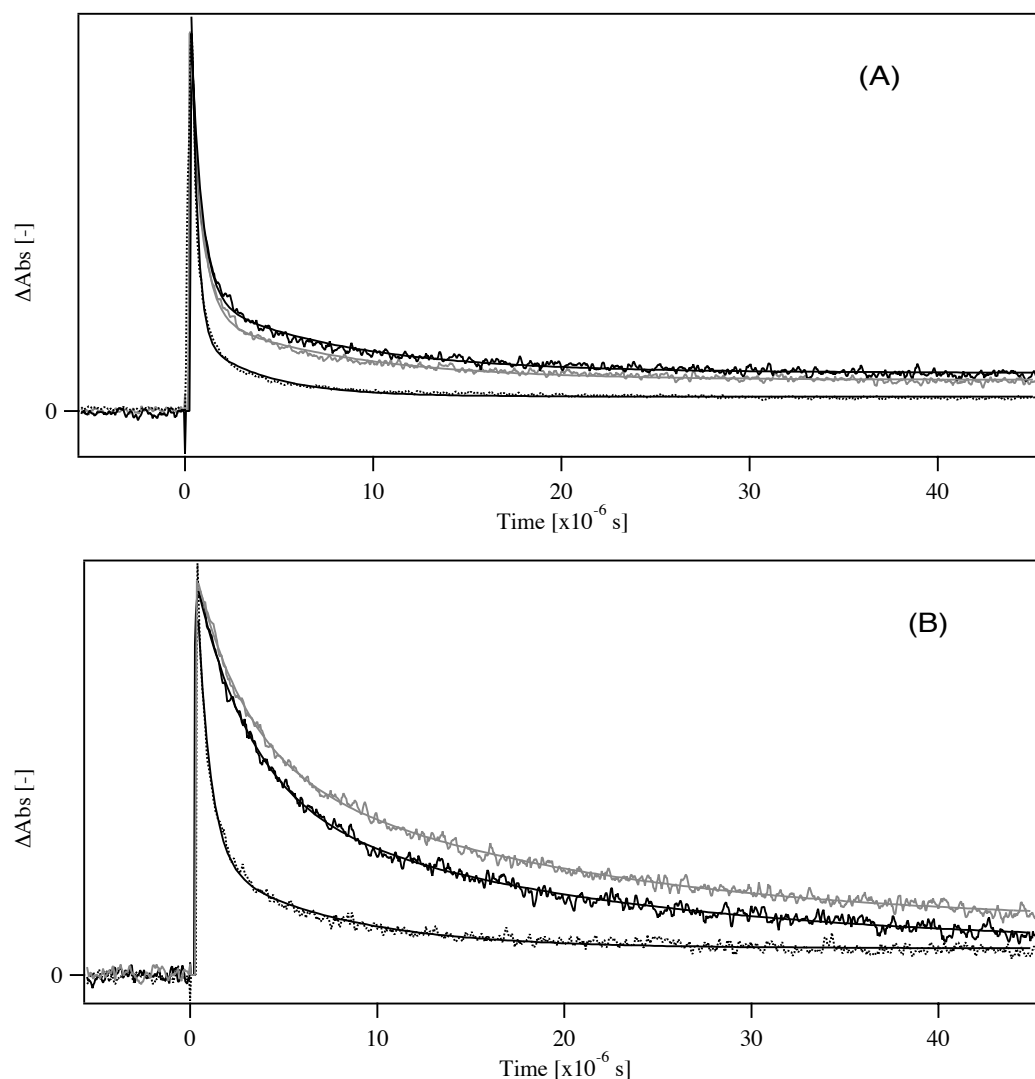
Figure 8.3: Transient absorption decay kinetics of the hole-conductor cation; (A) Dip-coated samples, (B) CBD deposited samples. The samples were modified with; DPA (black line) and HDMA (grey line). Samples without co-adsorption (dotted lines) were taken as reference. The double exponential fitted curve (full lines) are also shown.

The influence of the co-adsorbed molecule is clearly seen on the decay kinetics. The interfacial recombination is slowed by the addition of DPA and HDMA on the surface. The decay could be well fitted by a double exponential, the corresponding time constants are given in Table 8.1.

Dip-coating	k_{r1} [s^{-1}]	k_{r2} [s^{-1}]	CBD	k_{r1} [s^{-1}]	k_{r2} [s^{-1}]
No coadsorber	$2.76*10^5$	$3.19*10^6$	No coadsorber	$1.47*10^5$	$1.45*10^6$
DPA	$1.31*10^5$	$1.77*10^6$	DPA	$5.61*10^4$	$3.41*10^5$
HDMA	$1.32*10^5$	$1.69*10^6$	HDMA	$5.89*10^4$	$3.75*10^5$

Table 8.1: Double exponential time constant for dip-coated and CBD samples modified with HDMA and DPA.

The fast decay always accounts for a large part of the signal. For dip-coated samples, 85 % to 90 % of the signal is due to the rapid decay, whereas this part is about 60 % in CBD samples. This phenomenon has already been observed in Chapter 6 and explained by the fact that electrons in CBD samples are more likely to be deeply trapped and thus are not energetic enough to be injected into TiO$_2$. These deeply trapped electrons recombine with the oxidised hole-conductor.

By comparing the relative effect of the co-adsorbed molecules on the decay kinetics, one can easily notice that the influence is stronger in CBD samples than in dip-coated ones. For example the fast exponential decay is slowed down by a factor of two in dip-coated samples and of four in CBD samples. This result is contrary to a previous supposition. If the role of the co-adsorbed molecules is to block the interfacial recombination by the formation of a dense layer between the surface of the TiO$_2$ and the hole-conductor, then its effect should be stronger in dip-coated samples as it has been shown that the recombination is much faster due to the presence of bare TiO$_2$.

Small differences in the kinetics can be noticed when comparing the signals of DPA and HDMA. The recombination kinetics of DPA co-modified dip-coated samples are slightly slower than HDMA modified ones. This can be explained by the fact that phosphonate groups bind stronger to oxide surfaces by the formation of P-O-Metal bonds than carboxylate entities, explaining a better coverage of the surface with DPA. In the case of CBD samples, this tendency is inversed. The recombination kinetics of the HDMA co-modified samples is slower than DPA modified ones. As here PbS covers TiO$_2$, the molecules will absorb on PbS. This inversed tendency may arise from the fact than the stronger binding of phosphonate groups is in competition with another factor which is the length of the alkyl chain. HDMA (C$_{16}$) has a longer alkyl chain than DPA (C$_{10}$), hence the thickness of the formed barrier is larger for HDMA. Furthermore, as the recombination kinetics depends on the distance between the two

recombining charges, the co-adsorption of HDMA should have a stronger influence than DPA. Even though the measured kinetic differences are small, the two effects might influence the system.

VIII.2 Fourier Transform Infrared Spectroscopy

Fourier transform infrared spectroscopy (FTIR) was used to monitor the adsorption of the co-modifying molecules at the surface. Figure 8.4 shows the spectra obtained using attenuated total reflectance FTIR (ATR-FTIR) for samples modified with DPA.
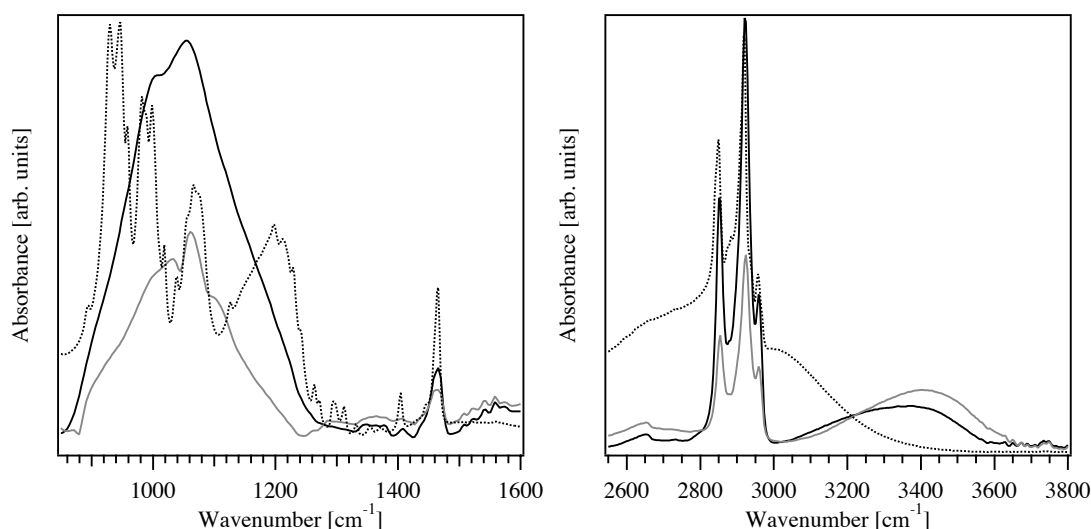

Figure 8.4: ATR-FTIR absorption spectra of crystalline DPA (dotted line) and PbS sensitised TiO_2 layer co-modified with DPA using dip-coating (black line) and CBD (grey line).

The spectrum of DPA exhibits sharp peaks at 947 and 1200 cm^{-1}, assigned to P-OH and P=O respectively. The peaks at 1000 and 1066 cm^{-1} are characteristic for the vibrational modes of the PO_3 group[17]. When DPA is deposited on the sensitised TiO_2, the sharp peaks characteristic for the solid-state change to much broader signals. The large peak centred around 1060 cm^{-1} is attributed to terminal or bridging phosphonate-metallic interactions[18]. Methylene deformation bands are observed on the three spectra at 1465 cm^{-1}. Other characteristic features of the alkyl chains are observed at 2856, 2920 and 2952 cm^{-1} and correspond to (ν_{asym} CH_2), (ν_{sym} CH_2), and (ν_{asym} CH_3) respectively. Finally, the broad peak around 3400 cm^{-1} is due to the presence of adsorbed water at the surface.

The relative signal intensity for the dip-coated and CBD sample gives an indication of the relative amount of DPA deposited on the surface. The signal being weaker for the

CBD sample, one can conclude that less DPA is present. One reason for this is the smaller effective surface area, arising from the partial pore filling due to the deposition of PbS.

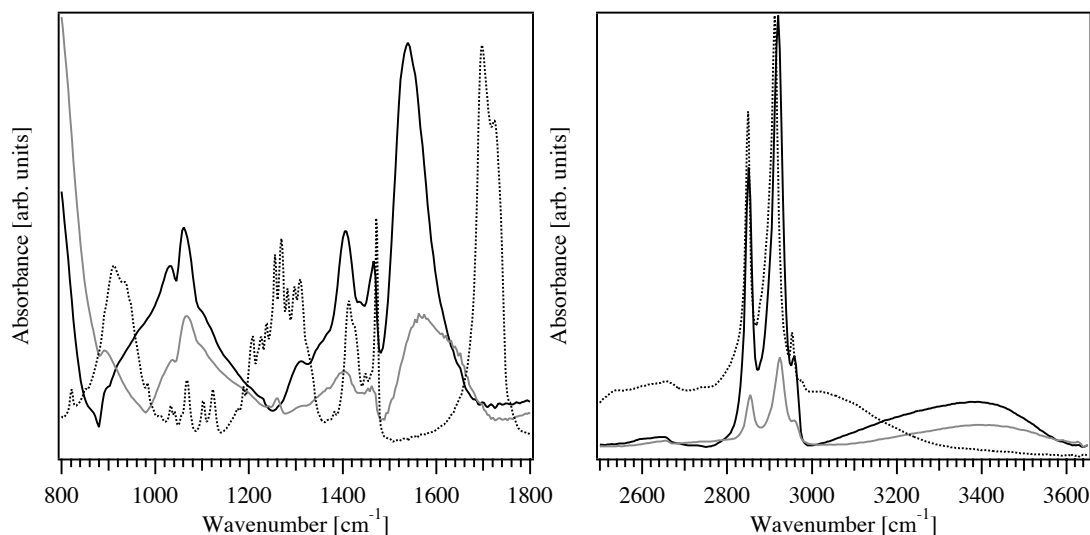Figure 8.5 shows the spectra of samples modified with HDMA.

Figure 8.5: ATR-FTIR absorption spectra of crystalline HDMA (dotted line) and PbS sensitised TiO$_2$ layer co-modified with HDMA using dip-coating (black line) and CBD (grey line).

The HDMA spectrum is characterised by a sharp peak at 1700 cm^{-1} due to the C=O stretch, and by a large peak around 3000 cm^{-1} arising from the OH group. The typical peaks for the alkyl chain between 2800 and 3000 cm^{-1} are also clearly visible. When HDMA is placed on the sensitised surface of TiO$_2$, the features due to C=O and OH disappear, but a strong sharp peak at 1550 cm^{-1} appears due to the asymmetric stretch of the COO^{-} entity.

Again the relative intensity of the peak between the CBD sample and the dip-coated sample indicates a lower amount of HDMA at the surface due to a lower effective surface area in the case of the CBD sample.

Wang et al.[12] observed a restricted access of water to the TiO$_2$ surface when DPA is co-adsorbed on the surface, which was clearly monitored by the suppression of the broad peak at 3400 cm^{-1}. On the contrary, when HDMA was co-adsorbed no water removal was observed. The reason for this is the stronger binding energy of the phosphonate group compared to the carboxylic group on the metal oxide surface. In the present measurements, shown in Figure 8.6, no significant change in the amount of water was measured when co-modifying the surface with DPA or with HDMA.
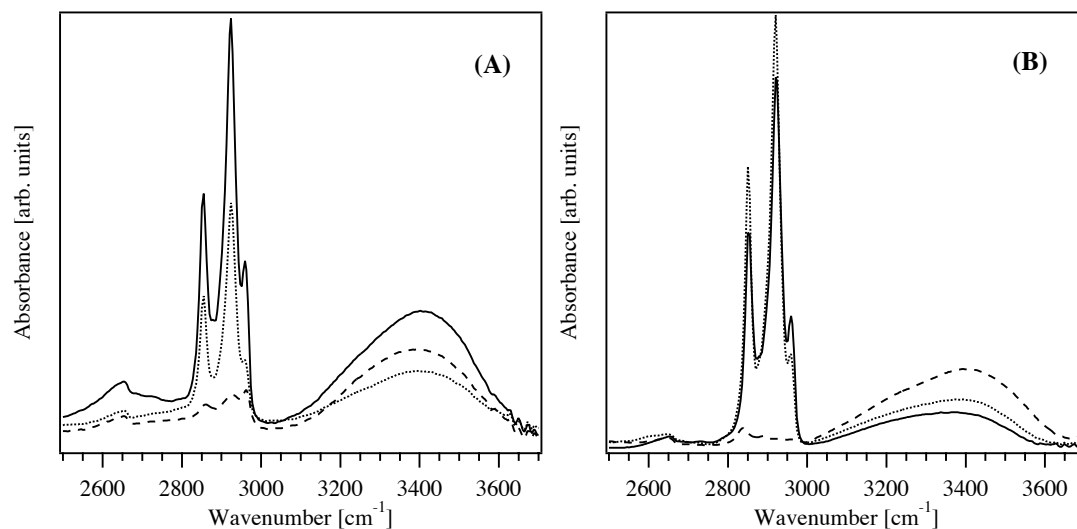
Figure 8.6: ATR-FTIR absorption spectra of TiO$_2$ modified layers; (A) TiO$_2$ sensitised using CBD, (B) using dip-coating. Sensitised layers were co-modified with DPA (full line), HDMA (dotted line). A sample without co-modification is also shown (dashed line).

VIII.3 Photovoltaic characterisation

Photovoltaic measurements were used to monitor the influence of the co-adsorbed molecules on the performance of the cell. Particular attention was paid to the variation of V_{OC} and I_{SC} when modifying the interface of the device. The first step was to screen the molecules shown in Figure 8.2.
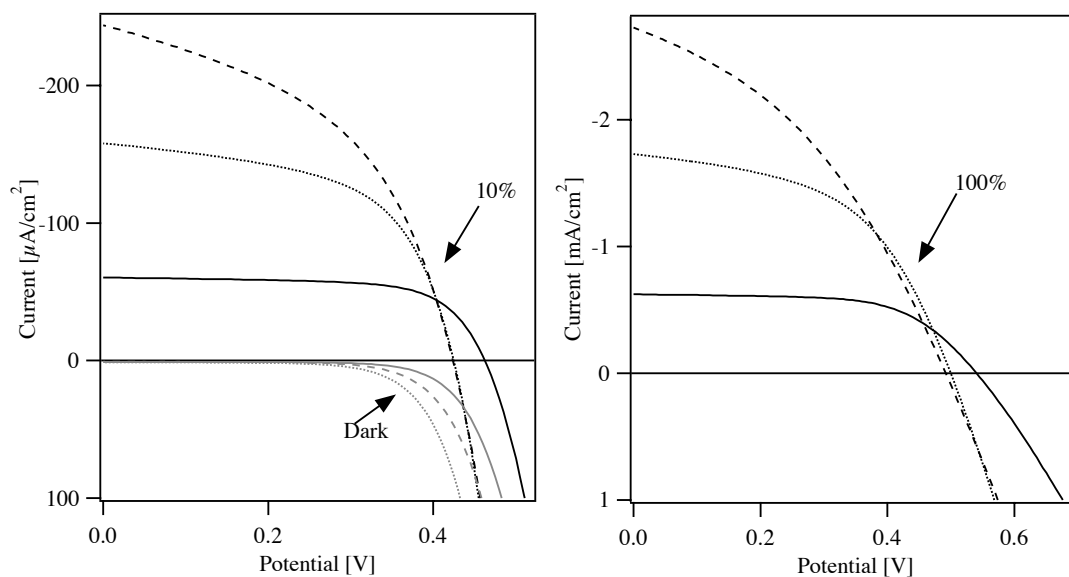
Figure 8.7: Current-voltage characteristics of TiO$_2$ electrodes sensitised with PbS deposited by CBD and derived with different types of aliphatic molecules; HDMA (dashed line), DPA (dotted line), and without co-adsorbed molecules (full line). Measurement (left) in the dark (grey lines) and at 10 % Sun illumination (10 mW/cm^2) (black lines), and measurement (right) at 100 % Sun illumination (100 mW/cm^2). The spin coating solution for the deposition of the hole conductor contained 0.13 M in spiro-OMeTAD, 7 mM in Li(CF$_3$SO$_2$)$_2$N and 0.2 mM in N(p-C$_6$H$_4$Br)$_3$SBCl$_6$.

In the case of a CBD device, the influence of the co-adsorbed molecules on the photovoltaic behaviour is shown in Figure 8.7. The short circuit current is strongly increased by both co-adsorbed molecules; I$_{SC}$ is nearly tripled with DPA and more than quadrupled with HDMA. This observation is true for low and high illumination intensities. But the open circuit potential is decreased in presence of the co-adsorbed molecules by 40 to 50 mV, depending on the molecules and the illumination intensity. The co-adsorption decreases the shunt resistance of the device but also the series resistance.
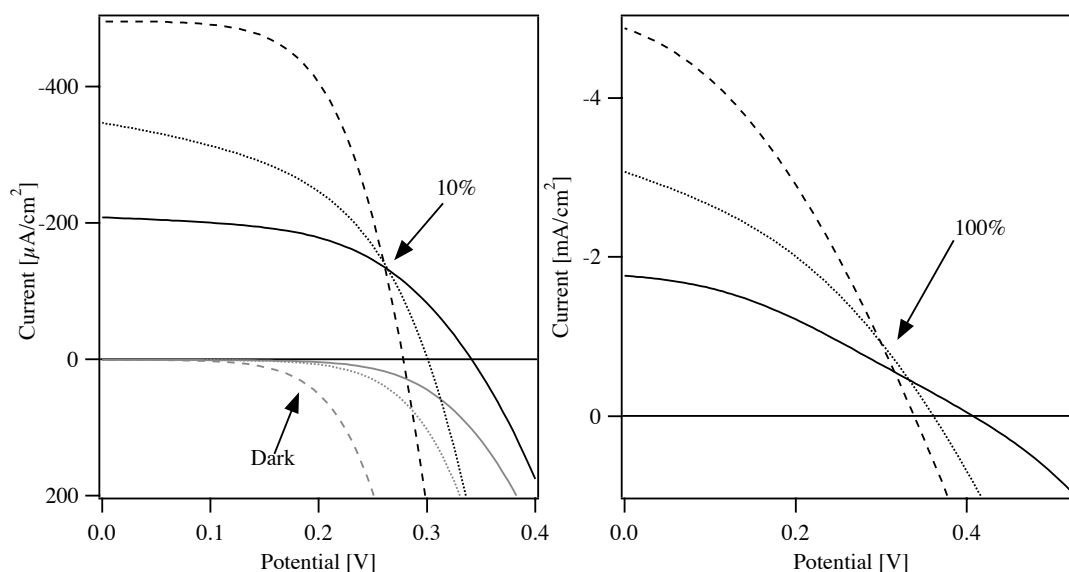
Figure 8.8: Current-voltage characteristics of TiO$_2$ electrodes sensitised with PbS deposited by three processes of dip-coating and derived with different types of aliphatic molecules; HDMA (dashed line), DPA (dotted line), and without co-adsorbed molecules (full line). Measurement in dark and at 10 % Sun illumination (10 mW/cm^2) (left), and measurement at 100 % Sun illumination (100 mW/cm^2) (right). The spin coating solution for the deposition of the hole conductor contained 0.13 M in spiro-OMeTAD, 7 mM in Li(CF$_3$SO$_2$)$_2$N and 0.2 mM in N(p-C$_6$H$_4$Br)$_3$SBCl$_6$.

When dip-coated electrodes are co-modified with HMDA and DPA, the effect on the photovoltaic behaviour, shown in Figure 8.8, is similar to CBD electrodes. The open-circuit voltage, as for CBD electrodes, is decreased, but in contrast to these electrodes the shift depends on the added molecule. While for DPA a decrease of 40 mV is observed in the case of HDMA, this shift reaches 70 mV.

HDMA modified electrodes yield higher currents than DPA modified ones, which give better currents than non-modified ones. Nevertheless, the current increase is not as spectacular as for CBD electrodes. I$_{SC}$ is more than doubled in the presence of HDMA and increased by 50% in the presence of DPA. This observation is in agreement with the nanosecond laser spectroscopy measurement, where it was observed that the recombination kinetics are slowed down more in the presence of HDMA or DPA on CBD electrodes than on dip-coated ones. As already mentioned, this result is astonishing, as one would have thought that covering the bare TiO$_2$ surface of dip-coated samples with the coadsorber affects more the operation of the device than in the case of CBD electrodes. One explanation for this phenomenon is PbS surface passivation. The two different synthetic routes used for the PbS

sensitisation of TiO_2 import different properties to the synthesised materials, not only in the surface morphology but also in their chemical characteristics. It was shown in Chapter 6 that the surface traps play an important role in the injection kinetics. Supposing that CBD gives rise to PbS containing more surface states than the dip-coating method, then the influence of a surface passivating agent would be more effective for CBD electrodes. This shows that the co-modification not only helps to block the interfacial recombination but also enhances the electron injection. This second possible mechanism could also explain the differences in the effects of the co-modification effects between the solid-state device and the ionic liquid-containing device used by Wang[12,14].
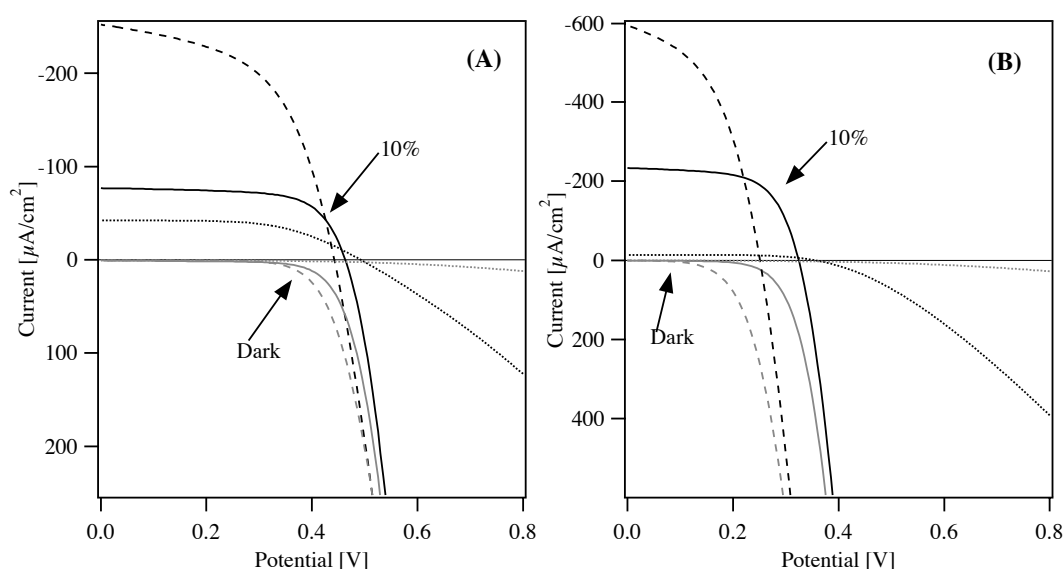

Figure 8.9: Current-voltage characteristics of TiO_2 electrodes sensitised with PbS deposited by CBD (A) or three processes of dip-coating (B). PbS sensitised electrodes (full lines) were modified by adsorption of HDMA (dashed line) or by adsorption of HDMA and 0.1 M tBP in the spin coating solution (dotted line). Measurements in dark and at 10 % Sun illumination (10 mW/cm^2) are shown on this Figure. The spin coating solution for the deposition of the hole conductor contained 0.13 M in spiro-OMeTAD, 7 mM in $Li(CF_3SO_2)_2N$ and 0.2 mM in $N(p-C_6H_4Br)_3SBCl_6$.

Figure 8.9 shows the influence of tBP in the hole-conductor matrix on the photovoltaic behaviour of HDMA co-modified electrodes. As already shown in Chapter 6 the influence on dip-coated electrodes is different to that on CBD electrodes. While for the tBP modified CBD electrodes, the I_{SC} is of same order of magnitude as the non-modified electrodes, in the case of dip-coated electrode the presence of tBP leads to a dramatic decrease of I_{SC}. In Chapter 6 it was shown that the open-cicuit voltage is increased by addition of tBP. The same observation can be

made for HDMA modified electrodes, where a shift of 50 mV is measured with CBD deposition and nearly 100 mV with dip-coating deposition.

By combining the co-modification with HDMA and the addition of tBP in the hole-conductor matrix, the beneficial effects of each treatment could be added together, to increase the I_{SC} but also the V_{OC} of the device. Unfortunately, no such effect was measured, certainly due to some sort of destructive interference between the two procedures.

VIII.4 Conclusions

The surface co-modification by using alkyl compounds containing either a phosphonic group or carboxylic group entity was shown to strongly increase the short-circuit current of the quantum-dot sensitised solid-state device by a factor of two or four. The long alkyl molecules adsorbed at the TiO_2 hole-conductor interface reduce the back electron transfer by forming a barrier at the interface.

The photovoltaic characterisation suggests also the existence of a second effect, which consists in the passivation of the PbS surface, thus enhancing the electron injection. Ultra fast spectroscopy studies are needed for a detailed understanding of this effect.

VIII.5 Bibliography

(1)   Haque, S. A.; Tachibana, Y.; Willis, R. L.; Moser, J. E.; Gratzel, M.; Klug, D. R.; Durrant, J. R. *Journal of Physical Chemistry B* **2000**, *104*, 538.

(2)   Kalyanasundaram, K.; Grätzel, M. *Coord Chem Rev* **1998**, *177*, 347.

(3)   Krüger, J.; Bach, U.; Grätzel, M. *Adv. Mater.* **2000**, *12*, 447.

(4)   Kumara, G. R. R. A.; Tennakone, K.; Perera, V. P. S.; Konno, A.; Kaneko, S.; Okuya, M. *J. Phys. D: Appl. Phys.* **2001**, *34*, 868.

(5)   Zhang, X.-t.; Sutanto, I.; Taguchi, T.; Tokuhiro, K.; Meng, Q.-b.; Rao, T. N.; Fujishima, A.; Watanabe, H.; Nakamori, T.; Uragami, M. *Solar energy materials and solar cells* **2003**, *80*, 315.

(6)   Kay, A.; Grätzel, M. *Chem Mater.* **2002**, *14*, 2930.

(7)   Diamant, Y.; Chen, S. G.; Melamed, O.; Zaban, A. *J. Phys. Chem. B* **2003**, *107*, 1977.

(8)   Bach, U.; Lupo, D.; Comte, P.; Moser, J. E.; Weissörtel, F.; Salbeck, J.;
        Spreitzer, H.; Grätzel, M. *Nature* **1998**, *395*, 583.

(9)   Krueger, J. Interface engineering in solid-state dye-sensitized solar cells,
        EPFL, 2003.

(10)   Liu, Y. J.; Yu, H. Z. *Journal of Physical Chemistry B* **2003**, *107*, 7803.

(11)   Selzer, Y.; Salomon, A.; Cahen, D. *Journal of the American Chemical Society*
        2002, *124*, 2886.

(12)   Wang, P.; Zakeeruddin, S. M.; Humphry-Baker, R.; Moser, J. E.; Grätzel, M.
        Adv. Mater. **2003**, *15*, 2101.

(13)   Wang, P.; Zakeeruddin, S. M.; Comte, P.; Charvet, R.; Humphry-Baker, R.;
        Grätzel, M. *J. Phys. Chem. B* **2003**, *107*, 14336.

(14)   Wang, P.; Zakeeruddin, S. M.; Humphry-Baker, R.; Grätzel, M. *Chem
        Commun.* **Submitted**.

(15)   Wang, P.; Zakeeruddin, S. M.; Moser, J. E.; Gratzel, M. *Journal of Physical
        Chemistry B* **2003**, *107*, 13280.

(16)   Wang, P.; Zakeeruddin, S. M.; Moser, J. E.; Nazeeruddin, M. K.; Sekiguchi,
        T.; Gratzel, M. *Nature Materials* **2003**, *2*, 498.

(17)   Gawalt, E. S.; Lu, G.; Bernasek, S. L.; Schwartz, J. *Langmuir* **1999**, *15*, 8929.

(18)   Frey, B. L.; Hanken, D. G.; Corn, R. M. *Langmuir* **1993**, *9*, 1815.

Chapter IX

General Conclusions and Outlooks

The goal of the present work was the replacement of the usually used organo-metallic dye in the solid-state nanocrystalline solar cell by inorganic semiconductor nanoparticles. Several types of nanoparticles have been studied to fulfil this function.

IX.1   General Conclusions

PbS nanoparticles have been synthesised in-situ on the TiO$_2$ surface following a simple synthetic route called dip-coating. The characterisation of the system using time resolved spectroscopy showed that the electron injection does not occur directly after photoexcitation but rather from trapped states located at the surface of the nanoparticles. It was also shown that the interfacial recombination between an injected electron and the oxidised hole-conductor represents the major loss reaction in the studied system. Overall conversion efficiency of 0.5 % at 0.1 Sun (AM1.5) was achieved with those systems.

The reduction of the loss mechanisms was attempted with the capping of the deposited PbS nanoparticles using other semiconductors such as CdS and ZnS. By covering PbS with a semiconductor having similar crystalline forms as CdS, an enhancement of the optical absorption was achieved. The further coating with ZnS was supposed to passivate the surface by reducing the trap states. Nanosecond laser spectroscopy allowed to demonstrate a significant reduction of the interfacial recombination when capping the PbS nanoparticles with CdS and ZnS. Nevertheless

the overall conversion efficiency could not be increased due to high shunt resistances appearing when the device was tested under full sunlight illumination.

Another synthetic route was then used to form a thin film of PbS at the surface of TiO$_2$, called chemical bath deposition (CBD). By forming a covering film on the TiO$_2$ surface the interfacial charge recombination can be partially avoided as an intimate contact between the TiO$_2$ and the hole-conductor can no more exist. Time resolved spectroscopy showed this phenomenon to occur; the measured recombination kinetics were much slower for CBD deposited samples than for dip-coated samples. Increasing the open-circuit potential of the device was a supplementary proof as this potential is highly affected by the interfacial recombination. Unfortunately the overall efficiency of the CBD device was not higher than the dip-coated one. The collected currents were lower compared to the dip-coated device. This was assigned to a reduction of the effective surface area of the device, due to partial pore filling by the PbS film, decreasing charge regeneration in those pores. The overall conversion efficiencies were identical to those of dip-coated devices but were linear from 0.1 Sun to 1 Sun.

Further interface optimisation was achieved by surface co-modification using organic molecules containing long alkyl chains (C$_{10}$ or C$_{16}$) and an anchoring group like carboxylic or phosphonic entities. The two investigated molecules, hexadecylmalonic acid (HDMA) and decylphosphonic acid (DPA), produced a spectacular increase of the short-circuit current, by a factor of two to four depending on the conditions. This allowed reaching nearly 1 % conversion efficiency at 0.1 Sun (AM 1.5).The effectiveness of these molecules to block the interfacial recombination was also shown by nanosecond laser measurements.

The kinetics were shown to be slowed by the surface co-modification. The influence of HDMA and DPA differed between dip-coated samples and CBD samples. It was first thought that the co-modification influences more the former ones as for these, the interfacial recombination is faster. The time resolved measurement and the photovoltaic characteristics, however, showed the contrary; the photovoltaic performances of the CBD samples were increased more significantly than for dip-coated samples. These observations could be assigned to a surface state passivation effect of the molecules.

Apart from metal sulfide sensitisation, metal selenide sensitisation was investigated. CdSe and PbSe were deposited in-situ on TiO$_2$ by chemical bath deposition.

Unfortunately the photovoltaic response of such devices was much lower than the PbS sensitised ones. Fluorescence spectroscopy allowed pointing out incomplete luminescence quenching of the CdSe sensitised device. It was concluded that an inefficient electron injection is responsible for the bad performances of the device, due to a bad matching of energy levels between the sensitiser and the TiO_2.

IX.2   Outlooks

First of all, the understanding of the effects of the co-modifying molecules on the performance of the device should be improved by ultra-fast laser spectroscopy. The hypothesis of blocking the surface states could be proven with this technique. It should also be possible to prove that the influence of these traps is stronger for CBD samples than for dip-coated samples.

The application of tBP has not had a positive effect on the system operation, but interfacial recombination could also be restricted by the use of a base, and a screening of various candidate bases could be done to find a less aggressive compound for this function.

It should also be very interesting to see if the use of other synthetic routes could enhance the performance of the device. Atomic layer deposition could for example be used to sensitise the system with a variety of semiconductor nanoparticles. Better light absorption could be achieved with other types of nanoparticles. Furthermore this technique allows the preparation of thin trap-poor semiconductor films, which should help to avoid one of the major loss processes.

Appendix

A.1: Curriculum Vitae

Name: Robert Plass

Date of birth: 20th of December 1975 in Geneva

Nationality: Swiss

Work Experiences

2000-2004: Ph.D. Thesis work at the Swiss Federal Institut of Technology in Lausanne (EPFL), Laboratory of Photonics and Interfaces (LPI) of Prof. Grätzel :

- Development and optimisation of solar cells.
- Study of the nanoparticle sensitisation
- Exercises session assistant for thermodynamics lectures
- Teaching lab classes of physical-chemistry

1999-2000: Master Thesis at the EPFL, LPI :

- Synthesis and characterisation of a new molecular dyad.

1997: Training period at Henkel GmbH in Vienna (Austria) :

- Responsible for quality control

Education

2000-2004: Ph.D. at the EPFL, LPI .

1995-2000: Studies in Chemistry at the EPFL.

1994-1995: Studies in Physics at the EPFL.

1990-1994: *Maturité fédérale* (highschool examination) with science specialisation, Collège du Léman, Versoix, Geneva.

Languages

French: Mother tongue

German: Mother tongue

English: Read, spoken, written

Romanian: Beginner

Patent

European Patent **00810681.7 :** R. Plass, U. Bach & M. Grätzel

Publications

1) R. Plass, S. Pelet, J. Krüger, U. Bach and M. Grätzel *J. Phys. Chem. B* **2002**, *106*, 7578-7580. *Quantum Dot Sensitization of Organic-Inorganic Hybrid Solar Cells.*

2) J. Krüger, R. Plass, P. Cameron, et al. *J. Phys. Chem B* **2003**, *107*, 7536-7539. *Charge transport and back reactionin solid-state dye-sensitized solar cells : A study using intensity-modulated photovoltage and photocurrent spectroscopy.*

3) J. Krüger, R. Plass, M. Grätzel et al. *Appl. Phys. Lett.* **2002**, *81*, 367. *Improvement of the photovoltaic performance of solid-state dye-sensitized device by silver complexation of the sensitizer cis-bis(4,4'-dicarboxy-2,2'bipyridine)-bis(isothiocyanato)ruthenium (II).*

Conferences

- 14th International Conference on Photochemical Conversion and Storage of Solar energy (IPS-14), 2002, Sapporo, Japan; Poster presentation *Quantum-dot sensitization of organic-inorganic hybrid solar cells.*

- 10th International Conference on Unconventional Photoactive Systems (UPS-01), 2001, Les Diablerets, Switzerland; Poster presentation *Solid-state Photovoltaic Cell Sensitized by PbS and CdS Nanoparticles.*

- EPA, Joint Meeting of the Italian, French, and Swiss Photochemistry Groups, 2001, Lausanne